Nuclear Dynamics in Electronic Decay Processes followed by Fragmentation

Dissertation
Ying-Chih Chiang
2012

Inaugural-Dissertation

zur Erlangung der Doktorwürde der
Naturwissenschaftlich-Mathematischen
Gesamtfakultät der
Ruprecht-Karls-Universität
Heidelberg

Presented by

Master of Science (Chemist) Ying-Chih Chiang

Born in Tainan, Taiwan

Day of Oral Examination: 19th of October, 2012

Nuclear Dynamics in Electronic Decay Processes followed by Fragmentation

Gutachter: Prof. Dr. Lorenz S. Cederbaum
Prof. Dr. Jochen Schirmer

Abstract

The impact of the nuclear dynamics during an electronic decay process followed by fragmentation in a diatomic system is investigated for three different examples, by using a time-dependent approach.

The first example is the prediction of the interatomic Coulombic decay (ICD) process in NeAr, following the Ne 1s Auger decay. It is a two-step (cascade) decay process where the first step is a fast Auger decay and the second step is the ICD of interest. A full cascade calculation has been performed to provide the (time-resolved) Auger electron and (time-resolved) ICD electron spectra. Our results show that the line width of the Auger electron spectrum contains also the information on the total ICD width at the equilibrium internuclear distance of NeAr. In addition, simulations show that the nuclear motion during the first Auger step has no impact on the following ICD process. This ICD process has been verified by experiment, and if a simple modification of the *ab initio* ICD transition rate is adopted, our simulated ICD spectrum agrees well with the experimental result.

For an electronic decay process followed by fragmentation, the energy spectrum of the emitted electron and the kinetic energy release (KER) spectrum of the ionic fragments are usually considered to be mirror images of each other. This is termed “mirror image principle” and is often applied in experiments. It is usually valid for the ICD electron spectrum and its corresponding KER spectrum. However, the principle is merely an empirical rule and can break down even in a diatomic system. The molecular Auger process in CO is chosen as the second example, as it exhibits such a break down of the mirror image principle. Calculated KER and electron spectra for this process also agree well with experiment.

The resonant Auger process of HCl is chosen as the last example to demonstrate that the interaction between a molecule and an intense laser pulse (as are available today in free electron lasers) can lead to a strong light-induced non-adiabatic effect. It is a general effect that can be found in molecules interacting with an intense laser pulse, which gives rise to strong molecular overall rotation.

Besides the above applications, a new elegant and numerically efficient formulation for evaluating the (time-resolved) KER spectrum in an electronic decay process followed by fragmentation is derived in this work. The KER spectrum now has a simple physical interpretation: it is the accumulated (over time) generalized Franck-Condon factor between the nuclear wave packet on the intermediate decaying state and the discrete continuum eigenfunctions of the dissociative final state. This new representation allows one to analyze the KER and the electron spectra, and it provides the conditions for the mirror image principle to hold.

Kurzfassung

Diese Arbeit untersucht anhand dreier konkreter Beispiele für zweiatomige Systeme den Einfluss der Kerndynamik auf elektronische Zerfallsprozesse mit anschließener Systemaufspaltung. Die Untersuchung erfolgt mit Hilfe einer zeitabhängigen Methode.

Das erste Beispiel ist der interatomare Coulomb-Zerfallsprozess (ICD) in NeAr, welcher nach dem Ne 1s Auger-Zerfall stattfindet. Hierbei handelt es sich um einen zweistufigen Zerfallsprozess (Zerfallskaskade), wobei die erste Stufe ein schneller Auger-Zerfall und die zweite Stufe der ICD-Prozess ist, an dem wir interessiert sind. Es wurden vollständige Berechnungen dieser Zerfallskaskade durchgeführt, um das (zeitaufgelöste) Energiespektrum des Auger-Elektrons und das des ICD-Elektrons zu erhalten. Unsere Resultate zeigen, dass die Linienbreite des Auger-Elektronenspektrums auch Informationen über die ICD-Gesamtbreite für den Gleichgewichts-Kernabstand von NeAr enthält. Außerdem zeigen die Simulationen, dass die Kernbewegung während der ersten Stufe (Auger) keinen Einfluss auf den folgenden ICD-Prozess hat. Dieser ICD-Prozess ist bereits experimentell bestätigt worden, und unser berechnetes ICD-Spektrum stimmt gut mit dem gemessenen Resultat überein, sofern eine einfache Anpassung der *ab initio* berechneten ICD-Zerfallsrate vorgenommen wird.

Für elektronische Zerfallsprozesse mit anschließender Systemaufspaltung wird gewöhnlich davon ausgegangen, dass das Energiespektrum des emittierten Elektrons ein Spiegelbild des Spektrums der "freigesetzten kinetischen Energie" (KER, für *kinetic energy release*) der ionischen Bruchstücke ist. Dieses "Spiegelbild-Prinzip" kommt häufig bei experimentellen Untersuchungen zum Einsatz. Für das ICD-Elektonenspektrum und das zugehörige KER-Spektrum ist dieses Prinzip üblicherweise zutreffend. Es ist jedoch eine empirische Regel, und kann auch in zweiatomigen Systemen verletzt werden. Der molekulare Auger-Prozess in CO stellt daher unser zweites Beispiel dar, denn er weist genau solch eine Verletzung des Spiegelbild-Prinzips auf. Die berechneten KER- und Elektronen-Spektra stimmen wiederum gut mit den experimentellen Ergebnissen überein.

Als letztes Beispiel wird der resonante Auger-Prozess in HCl behandelt. Hier zeigt sich, dass die Wechselwirkung eines Moleküls mit einem starken Laser-Puls (heutzutage verfügbar durch Freie-Elektronen-Laser) zu einem starken licht-induzierten nicht-adiabatischen Effekt führen kann. Hierbei handelt es sich um einen allgemeinen Effekt, der bei der Wechselwirkung zwischen Molekülen und intensiven Laserpulsen auftritt, da dieser zu einer starken Gesamtrotation des Moleküls führt.

Abgesehen von den bisher genannten Anwendungen wird in dieser Arbeit eine neue, elegante und numerisch effiziente Methode hergeleitet, mit der das (zeitabhängige) KER-Spektrum für elektronische Zerfallsprozesse mit anschließender Systemaufspaltung berechnet werden kann. Das KER-Spektrum erhält damit eine einfache physikalische Interpretation: es handelt sich um einen (über die Zeit) angesammelten verallgemeinerten Franck-Condon-Faktor zwischen der Kernwellenfunktion auf dem zerfallenden elektronischen Zwischenzustand und den Kontinuums-Eigenfunktionen des dissoziativen elektronischen Endzustands. Diese neuartige Darstellung erlaubt eine Analyse der KER- und Elektronen-Spektra und klärt die Bedingungen, unter denen das Spiegelbild-Prinzip gültig ist.

Contents

Chapter 1

Introduction

When a molecule or an atom interacts with radiation, its electrons can be excited or ionized. A core or valence hole (vacancy) is then created in such an (ionic) electronically excited system in contrast to the original electronic ground state. Such an excited system often decays via photon emission or, if energetically allowed, electron emission [1]. For instance, if a core hole, created by photoionization, is filled by one valence electron while another valence electron is emitted simultaneously, such a process is termed *Auger decay* [2]. Similarly, if a core hole, created by photoexcitation, undergoes an electronic decay process, this is called a *resonant Auger* process [3].

In contrast to the radiationless relaxation of a core hole, an inner-valence hole in an isolated atom or molecule usually decays via photon emission [4] because the available energy is insufficient for electron emission. However, if the system is embedded in an environment, e.g. with other neighbouring atoms, a radiationless decay channel named *interatomic Coulombic decay* (ICD) [5] becomes possible for an inner-valence hole. Known examples are ICD in van der Waals clusters and dimers [6–14], and ICD in water dimers [15–17]. In such a process, an outer-valence electron fills in the inner-valence hole, and the excess energy is immediately transferred to a neighboring atom, leading to a valence-electron ionization from the neighboring atom. A typical illustrative example is the ICD process in the Ne dimer [8, 10]. After a 2s electron (inner-valence electron) of the target Ne is photoionized, one 2p electron (outer-valence electron) can fill the 2s vacancy and simultaneously one 2p electron from the *neighboring* Ne is emitted, and overall two Ne^+ are produced. These resulting ions then undergo *Coulomb explosion* since the van der Waals dimer is only weakly bound [6, 8, 10].

In such a process, i.e. fragmentation following the emission of an electron, both the emitted electron and the translational kinetic energy of the ionic fragments can be measured. The former gives the electron kinetic energy distribution, e.g. the ICD electron spectrum [8] or the Auger electron spectrum [18], while the latter[1] leads to the so-called *kinetic energy release* (KER) distribution [19]. These two spectra can be measured independently or in coincidence [20], which often provides more information for analyzing the channels.

The spectra measured for molecular electronic decay processes frequently show profound fingerprints of the nuclear motion [3, 13, 14, 18, 19, 21, 22] because lifetimes of the electronic decaying states are comparable with the timescales of molecular motion [23]. Even for a diatomic molecule, the stretching motion along the internuclear axis can strongly influence the electron[2] or KER spectra. For example, one sees the fingerprints of vibrational wave functions in the ICD spectrum of the He dimer [13, 14, 24]. A more extreme example is the direct competition between radiationless decay and fragmentation, taking place when the potential curve of the excited molecule is purely dissociative. In such a process, the measured spectrum contains a molecular background as well as a distinct atomic peak [25]. All these interesting phenomena encourage theoretical studies of the molecular motion participating in an electronic decay process [26, 27]. In particular, a time-dependent approach provides valuable insights into the molecular dynamics [26, 28, 29].

In this work, we study this impact of nuclear dynamics during electronic decay processes. Our first example is the ICD following Ne 1s Auger decay in NeAr (see Ch. 3 and Ch. 4), which belongs to the family of multi-step (or *cascade*) decay processes. Cascade processes have been studied in the beginning under the name of vacancy cascade reorganization [30], and later were observed in Auger cascade processes [31, 32]. A general theory on cascade processes using a time-independent method has been derived in Ref. [33].[3] Here we describe the cascade processes based on a time-dependent approach. The derivation of equations of motion for nuclear wave functions (in cascade processes) is given in Ch. 2. How to evaluate the time-resolved electron spectrum in a cascade process and how to evaluate the time-resolved KER spectrum are discussed in Ch. 5 and Ch. 6, respectively. Finally, the influence of a laser pulse on the molecular motion, and consequently on the spectrum, will be discussed in Ch. 7, where the chosen example is the molecular resonant Auger process [25] in an intense laser field (non-perturbative regime) [34].

---

[1] The kinetic energy of the center of mass is subtracted.

[2] For briefness, the emitted electron spectrum, e.g. Auger or ICD electron spectrum, will be abbreviated as “electron spectrum” and is to be distinguished from the photoelectron spectrum.

[3] In Ref. [33], the author focused on proving that the electron spectrum calculated via the time-independent method is equivalent to the one calculated via the time-dependent method. Equations of motion in Ref. [33] were given without derivations.

Chapter 2

A Time-Dependent Approach to Cascade Decay Processes

In this work, the impact of nuclear dynamics on the electron spectrum, measured from an electronic decay process, is of interest. We would like to study the nuclear motion, taking place in a two-step (cascade) electronic decay process, e.g. ICD processes following the Ne $1s$ Auger decay in NeAr, with a time-dependent approach.

For a cascade decay process, the equations of motion (EOMs) for the nuclear wave functions within different electronic states can be derived from the time-dependent Schrödinger equation ($\hbar = 1$)

$$i\frac{\partial}{\partial t}|\Psi(t)\rangle = \hat{H}|\Psi(t)\rangle \ , \tag{2.1}$$

with a total wave function $|\Psi(t)\rangle$ and a total Hamiltonian $\hat{H}$ [26]. In this chapter, it is explained in detail how to choose the wave function, how to derive the EOMs, and how to evaluate the electron spectrum. The general procedure to obtain EOMs can be easily adapted to different kinds of processes as shown later. For a fully equivalent time-independent theory on cascade decay processes, see Ref. [33].

2.1 Equations of Motion for a Single-Channel Two-Step Decay Process

For simplicity, the first example is chosen as a two-step decay process such that four non-degenerate electronic states are present. The decay process is accompanied by

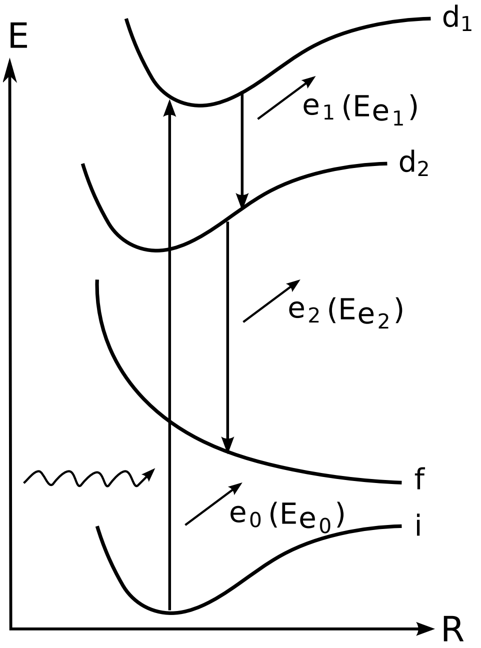

Figure 2.1: Schematic picture of a single channel cascade decay process. The potential energy curves of the electronic ground state (labeled as i), the first intermediate state (labeled as d_1), the second intermediate state (labeled as d_2), and the final state (labeled as f) are depicted. States d_1, d_2, and f are singly, doubly, and triply ionic, respectively. After photoionization, the system decays from the ionic state d_1 to the doubly ionic state d_2 via emitting an electron (denoted as e_1) with the kinetic energy E_{e_1}. The state d_2 is also an intermediate state, which further decays to the repulsive final state f by emitting another electron e_2, whose kinetic energy is denoted by E_{e_2}.

particle emission, e.g. photon or electron emission. In the following sections only the electron emission will be discussed, but the photon emission can be described in a similar manner.

The process is depicted schematically in Fig. 2.1. By absorbing a photon, whose energy is above the (core) ionization threshold of interest, the molecule is ionized to the ionic intermediate state d_1 from the electronic ground state i. The kinetic energy of the emitted photoelectron is denoted by E_{e_0}. The system then decays from the singly ionic intermediate state d_1 to the doubly ionic intermediate state d_2 via emitting an electron e_1 with the kinetic energy E_{e_1}. The state d_2 can further decay to the repulsive final state f via emitting another electron e_2 with energy E_{e_2}. For a general decay process, the potentials of those involved electronic states can be bound, resonant, or purely repulsive. The EOMs hold for all kinds of potentials.

The ansatz for the total wave function for this process is given as a coherent superposition of wave functions on all involved electronic states:

$$
\begin{aligned}
|\Psi(t)\rangle = |\Phi_i\rangle|\psi_i(t)\rangle + \int & \mathrm{d}E_{e_0}|\Phi_{d_1}, E_{e_0}\rangle|\psi_{d_1}(E_{e_0}, t)\rangle + \\
\iint & \mathrm{d}E_{e_0}\, \mathrm{d}E_{e_1}|\Phi_{d_2}, E_{e_0}, E_{e_1}\rangle|\psi_{d_2}(E_{e_0}, E_{e_1}, t)\rangle + \\
\iiint & \mathrm{d}E_{e_0}\, \mathrm{d}E_{e_1}\, \mathrm{d}E_{e_2}|\Phi_f, E_{e_0}, E_{e_1}, E_{e_2}\rangle|\psi_f(E_{e_0}, E_{e_1}, E_{e_2}, t)\rangle \ . \qquad (2.2)
\end{aligned}
$$

In Eq. (2.2), the Born-Oppenheimer approximation has been applied. $|\Phi_x\rangle$ and $|\psi_x(t)\rangle$ are, respectively, the electronic and nuclear wave functions of the state x, which can be the ground state i or the ionic states d_1, d_2, f. The wave functions are more intricate for the ionic states d_1, d_2 and f due to the presence of the outgoing electron(s). In consequence, the wave functions for these states are combined (augmented) with the wave function(s) of the outgoing electron(s). In the literature [35], the wave function of an outgoing electron is often expanded by its energy eigenfunctions, which are continuum functions, i.e. they lie in the continuum part of the spectrum. For instance, the wave function of the photoelectron can be written as

$$
|\Psi_{e_0}\rangle = \int \mathrm{d}E_{e_0}\, b(E_{e_0})|E_{e_0}\rangle \ ,
$$

where $b(E_{e_0})$ is the expansion coefficient. The outer product of $|E_{e_0}\rangle$ and $|\Phi_{d_1}\rangle$ yields the electronic wave function $|\Phi_{d_1}, E_{e_0}\rangle$ of the ionic state d_1 and the outgoing photoelectron. Similarly, multiplying $b(E_{e_0})$ and $|\psi_{d_1}(t)\rangle$ leads to the nuclear wave function $|\psi_{d_1}(E_{e_0}, t)\rangle$, which is the amplitude of finding the system in the ionic state d_1 with an outgoing photoelectron whose energy is E_{e_0}. Due to the nature of continuum functions, the summation over all possible electron energies becomes an integral over E_{e_0}. This procedure can be summarized as the following: *The state d_1 is embedded in a continuum, due to the presence of the outgoing electron e_0. The electronic wave function then is augmented with the wave function of the outgoing electron, e.g. $|\Phi_{d_1}, E_{e_0}\rangle$, and the corresponding nuclear wave function depends on E_{e_0}, e.g. $|\psi_{d_1}(E_{e_0}, t)\rangle$.* Similarly, the electronic wave functions of states d_2 and f are augmented with the wave functions of the emitted electrons, yielding $|\Phi_{d_2}, E_{e_0}, E_{e_1}\rangle$ and $|\Phi_f, E_{e_0}, E_{e_1}, E_{e_2}\rangle$; their nuclear wave functions now depend on the energy of the emitted electrons, namely $|\psi_{d_2}(E_{e_0}, E_{e_1}, t)\rangle$ and $|\psi_f(E_{e_0}, E_{e_1}, E_{e_2}, t)\rangle$. All nuclear wave functions additionally depend on the nuclear degrees of freedom, e.g. the internuclear distance R. See Sec. 7.2 on further details on molecular rotation.

The electronic wave functions used in Eq. (2.2) obey the following ortho-normalization rules:

$$
\begin{aligned}
\langle\Phi_i|\Phi_i\rangle &= 1 \\
\langle\Phi_{d_1}, E_{e_0}|\Phi_{d_1}, E'_{e_0}\rangle &= \delta(E_{e_0} - E'_{e_0}) \\
\langle\Phi_{d_2}, E_{e_0}, E_{e_1}|\Phi_{d_2}, E'_{e_0}, E'_{e_1}\rangle &= \delta(E_{e_0} - E'_{e_0})\,\delta(E_{e_1} - E'_{e_1}) \\
\langle\Phi_f, E_{e_0}, E_{e_1}, E_{e_2}|\Phi_f, E'_{e_0}, E'_{e_1}, E'_{e_2}\rangle &= \delta(E_{e_0} - E'_{e_0})\,\delta(E_{e_1} - E'_{e_1})\,\delta(E_{e_2} - E'_{e_2}) \ . \qquad (2.3)
\end{aligned}
$$

Dirac delta functions $\delta(E_{e_j} - E'_{e_j})$ are employed to denote the orthonormal properties of the continuum functions. The electronic wave functions of different electronic states are always orthogonal, e.g. $\langle \Phi_i | \Phi_{d_1}, E_{e_0} \rangle = 0$. Additionally, the norm of the total wave function must always be conserved, i.e. $\langle \Psi(t) | \Psi(t) \rangle = 1$.

The total Hamiltonian [26] for the system of interest reads

$$\hat{H} = \hat{H}_{\mathrm{el}} + \hat{T}_{\mathrm{nucl}} + \hat{\mathbf{D}} \cdot \mathbf{E}(t) \ . \tag{2.4}$$

The term $\hat{H}_{\mathrm{el}}$ denotes the electronic Hamiltonian, containing the kinetic energy operator of the electrons, the electron-electron interaction, the electron-nuclear interaction, as well as the nuclear-nuclear interaction; hence the electronic Hamiltonian depends parametrically on the nuclear coordinates. The nuclear kinetic energy operator is denoted by $\hat{T}_{\mathrm{nucl}}$. These two terms form the field-free Hamiltonian, describing atoms or molecules, without any interaction with an external field. The last term of Eq. (2.4) describes the interaction between molecules and the external laser electric field $\mathbf{E}(t)$. The electric field is treated classically in the current theory.[1] $\hat{\mathbf{D}}$ denotes the dipole operator. If the initial process is excitation, then the term describes the usual electric dipole transition. If the initial process is photoionization, then $\hat{\mathbf{D}}$ operates on the electronic wave function of the ground state and the electronic wave function of the ionic state augmented with the continuum [36].

A general Hamiltonian describes all charged particles moving in an electromagnetic field [37], and it should contain the electric dipole interaction, magnetic dipole interaction, electric quadrupole interaction, and so on. Eq. (2.4) contains only the electric dipole interaction, i.e. $\hat{\mathbf{D}} \cdot \mathbf{E}(t)$, and it is often sufficient for describing the molecule interacting with a laser pulse. However, the electric quadrupole interaction and the magnetic dipole interaction may also play a role [38], especially when the incident photon wavelength is around the size of the molecule. The generalization of the theory to cope with these interaction terms is straightforward, cf. e.g. Ref. [39].

Inserting the total wave function ansatz Eq. (2.2) and the total Hamiltonian Eq. (2.4) into the time-dependent Schrödinger equation Eq. (2.1), and projecting onto each elec-

---

[1] If the system decays via emitting a photon, the electric field and the photon states should be treated systematically by quantum theory too.

tronic state by using Eq. (2.3), we arrive at four coupled equations:

$$i|\dot{\psi}_i(t)\rangle = \hat{H}_i|\psi_i(t)\rangle + \int dE_{e_0}\hat{F}^\dagger(E_{e_0},t)|\psi_{d_1}(E_{e_0},t)\rangle \tag{2.5}$$

$$\begin{aligned} i|\dot{\psi}_{d_1}(E_{e_0},t)\rangle &= \hat{F}(E_{e_0},t)|\psi_i(t)\rangle + (\hat{H}_{d_1} + E_{e_0})|\psi_{d_1}(E_{e_0},t)\rangle \\ &+ \int \mathrm{d}E_{e_1}\hat{W}^\dagger_{d_1\to d_2}(E_{e_1})|\psi_{d_2}(E_{e_0},E_{e_1},t)\rangle \end{aligned} \tag{2.6}$$

$$\begin{aligned} i|\dot{\psi}_{d_2}(E_{e_0},E_{e_1},t)\rangle &= \hat{W}_{d_1\to d_2}(E_{e_1})|\psi_{d_1}(E_{e_0},t)\rangle + (\hat{H}_{d_2} + E_{e_0} + E_{e_1})|\psi_{d_2}(E_{e_0},E_{e_1},t)\rangle \\ &+ \int dE_{e_2}\hat{W}^\dagger_{d_2\to f}|\psi_f(E_{e_0},E_{e_1},E_{e_2},t)\rangle \end{aligned} \tag{2.7}$$

$$\begin{aligned} i|\dot{\psi}_f(E_{e_0},E_{e_1},E_{e_2},t)\rangle &= \hat{W}_{d_2\to f}(E_{e_2})|\psi_{d_2}(E_{e_0},E_{e_1},t)\rangle \\ &+ (\hat{H}_f + E_{e_0} + E_{e_1} + E_{e_2})|\psi_f(E_{e_0},E_{e_1},E_{e_2},t)\rangle \ , \end{aligned} \tag{2.8}$$

where $\hat{H}_x$ denotes the usual nuclear Hamiltonian, containing the nuclear kinetic energy operator and the potential of state x with $x = i,\ d_1,\ d_2,\ f$; $\hat{W}_{d_1\to d_2}(E_{e_1})$ denotes the transition matrix element from state d_1 to state d_2, i.e.

$$\hat{W}_{d_1\to d_2}(E_{e_1}) = \langle\Phi_{d_2}, E_{e_1}|\hat{H}_{\mathrm{el}}|\Phi_{d_1}\rangle \ .$$

Similarly the transition matrix element from state d_2 to f reads

$$\hat{W}_{d_2\to f}(E_{e_2}) = \langle\Phi_f, E_{e_2}|\hat{H}_{\mathrm{el}}|\Phi_{d_2}\rangle \ .$$

The interaction between an external field and the molecule, denoted by $\hat{F}(E_{e_0},t)$, is given by

$$\hat{F}(E_{e_0},t) = \langle\Phi_{d_1}, E_{e_0}|\hat{\mathbf{D}}|\Phi_i\rangle\cdot\mathbf{E}(t) = \boldsymbol{\mu}\cdot\mathbf{E}(t) \ , \tag{2.9}$$

where $\langle\Phi_{d_1}, E_{e_0}|\hat{\mathbf{D}}|\Phi_i\rangle$ is denoted by $\boldsymbol{\mu}$ for abbreviation[2]. The details of evaluating the inner product of the external field and the dipole transition moment will be given in Sec. 7.2.

Eqs. (2.5-2.8) are coupled. In principle, a set of coupled differential equations can be integrated numerically. In practice, Eq. (2.5) requires an integration over all possible $|\psi_{d_1}(E_{e_0},t)\rangle$. Each $|\psi_{d_1}(E_{e_0},t)\rangle$ can be obtained by solving Eq. (2.6) with different E_{e_0}. Similarly, Eq. (2.6) requires another integration over all possible $|\psi_{d_2}(E_{e_0},E_{e_1},t)\rangle$. In consequence, one has to solve infinitely many coupled equations simultaneously. An alternative procedure is naturally desired such that the numerical integration needed over the electron energies can be carried out analytically. To be more specific, the goal is to perform the integrations (over E_{e_0}, E_{e_1}, E_{e_2}) in Eqs. (2.5-2.7) analytically.

---

[2] In principle, the electric field can also couple states i and d_2 directly. However, these processes have very low probability. Hence we neglect them in the following considerations.

To proceed, we start from the formal solution of $|\psi_f(E_{e_0}, E_{e_1}, E_{e_2}, t)\rangle$, which can be obtained from rearranging Eq. (2.8) as:

$$|\psi_f(E_{e_0}, E_{e_1}, E_{e_2}, t)\rangle = -i \int_{-\infty}^{t} \mathrm{d}t' \; e^{i(\hat{H}_f + E_{e_0} + E_{e_1} + E_{e_2})(t'-t)} \hat{W}_{d_2 \to f}(E_{e_2}) |\psi_{d_2}(E_{e_0}, E_{e_1}, t')\rangle \; , \tag{2.10}$$

and inserting this into Eq. (2.7) leads to

$$\begin{aligned} i|\dot{\psi}_{d_2}(E_{e_0}, E_{e_1}, t)\rangle &= \hat{W}_{d_1 \to d_2}(E_{e_1}) |\psi_{d_1}(E_{e_0}, t)\rangle + (\hat{H}_{d_2} + E_{e_0} + E_{e_1}) |\psi_{d_2}(E_{e_0}, E_{e_1}, t)\rangle \\ &-i \iint \mathrm{d}t' \mathrm{d}E_{e_2} \, \hat{W}^{\dagger}_{d_2 \to f}(E_{e_2}) e^{i(\hat{H}_f + E_{e_0} + E_{e_1} + E_{e_2})(t'-t)} \hat{W}_{d_2 \to f}(E_{e_2}) |\psi_{d_2}(E_{e_0}, E_{e_1}, t')\rangle \; . \end{aligned} \tag{2.11}$$

The last term in Eq. (2.11) contains integrations over E_{e_2} and t and hence is considered as non-local in energy and in time. The terms $e^{i(\hat{H}_f + E_{e_0} + E_{e_1} + E_{e_2})(t'-t)}$ and $|\psi_{d_2}(E_{e_0}, E_{e_1}, t')\rangle$ oscillate rapidly in time and energy with approximately opposite phases. Consequently, the approximate total phase of the two terms varies slowly in time and energy, leading to a non-vanishing value after integrations. Analytically carrying out the integrations over time and energy by using the approximate total phase has been termed as the *local approximation*[26]. Applying this approximation, the last term in Eq. (2.11) becomes

$$\begin{aligned} &- i \iint \mathrm{d}t' \mathrm{d}E_{e_2} \, \hat{W}^{\dagger}_{d_2 \to f}(E_{e_2}) e^{i(\hat{H}_f + E_{e_0} + E_{e_1} + E_{e_2})(t'-t)} \hat{W}_{d_2 \to f}(E_{e_2}) |\psi_{d_2}(E_{e_0}, E_{e_1}, t')\rangle \\ &\approx -i \frac{\Gamma_{d_2}}{2} |\psi_{d_2}(E_{e_0}, E_{e_1}, t)\rangle \; , \end{aligned} \tag{2.12}$$

where $\Gamma_{d_2} = 2\pi |\hat{W}_{d_2 \to f}|^2$. Under the local approximation, $\hat{W}_{d_2 \to f}$ is independent from E_{e_2} and becomes a potential-like operator. Γ_{d_2} is known as the *transition rate* from state d_2 to f or the *decay rate (width)* of state d_2. The derivation of this equation is given in Appendix A. Using Eq. (2.12), Eq. (2.11) now reads,

$$i|\dot{\psi}_{d_2}(E_{e_0}, E_{e_1}, t)\rangle = \hat{W}_{d_1 \to d_2}(E_{e_1}) |\psi_{d_1}(E_{e_0}, t)\rangle + (\hat{\mathcal{H}}_{d_2} + E_{e_0} + E_{e_1}) |\psi_{d_2}(E_{e_0}, E_{e_1}, t)\rangle \; , \tag{2.13}$$

where $\hat{\mathcal{H}}_{d_2} = \hat{H}_{d_2} - i\Gamma_{d_2}/2$. After the local approximation, the nuclear Hamiltonian $\hat{\mathcal{H}}_{d_2}$ is non-Hermitian and contains an imaginary part, which describes the decay from state d_2 to f. Consequently, $|\psi_{d_2}(E_{e_0}, E_{e_1}, t)\rangle$ decays over time. On the other hand, $|\psi_f(E_{e_0}, E_{e_1}, E_{e_2}, t)\rangle$ increases over time, due to the source term $\hat{W}_{d_2 \to f} |\psi_{d_2}(E_{e_0}, E_{e_1}, t)\rangle$, see Eq. (2.8) and Eq. (2.10). In short, the norm of the total wave function is still conserved.

After the local approximation, Eq. (2.11) becomes Eq. (2.13), which is local in time and energy. Similarly, we would like to carry out the integration over E_{e_1} in Eq. (2.6) by performing the local approximation again. Inserting the formal solution of $|\psi_{d_2}(E_{e_0}, E_{e_1}, t)\rangle$ (obtained from Eq. (2.13)), Eq. (2.6) becomes:

$$\begin{aligned} i|\dot{\psi}_{d_1}(E_{e_0}, t)\rangle &= \hat{F}(E_{e_0}, t) |\psi_i(t)\rangle + (\hat{H}_{d_1} + E_{e_0}) |\psi_{d_1}(E_{e_0}, t)\rangle \\ &- i \iint \mathrm{d}t' \mathrm{d}E_{e_1} \, \hat{W}^{\dagger}_{d_1 \to d_2}(E_{e_1}) e^{i(\hat{\mathcal{H}}_{d_2} + E_{e_0} + E_{e_1})(t'-t)} \hat{W}_{d_1 \to d_2}(E_{e_1}) |\psi_{d_1}(E_{e_0}, t')\rangle \; . \end{aligned} \tag{2.14}$$

The last term of Eq. (2.14) is non-local in time and in energy. Applying the local approximation to integrate this term yields

$$\begin{aligned} & -i\iint \mathrm{d}t'\mathrm{d}E_{e_1}\,\hat{W}^{\dagger}_{d_1\to d_2}(E_{e_1})e^{i(\hat{\mathcal{H}}_{d_2}+E_{e_0}+E_{e_1})(t'-t)}\hat{W}_{d_1\to d_2}(E_{e_1})|\psi_{d_1}(E_{e_0},t')\rangle \\ & \approx -i\frac{\Gamma_{d_1}}{2}|\psi_{d_1}(E_{e_0},t)\rangle\ , \qquad (2.15) \end{aligned}$$

where $\Gamma_{d_1} = 2\pi|\hat{W}_{d_1\to d_2}|^2$ denotes the transition rate from state d_1 to d_2. Again, $\hat{W}_{d_1\to d_2}$ does not depend on E_{e_1} after the local approximation. A detailed derivation is also given in Appendix A. The new equation for $|\psi_{d_1}(E_{e_0},t)\rangle$ hence reads,

$$i|\dot{\psi}_{d_1}(E_{e_0},t)\rangle = \hat{F}(t)|\psi_i(t)\rangle + (\hat{\mathcal{H}}_{d_1} + E_{e_0})|\psi_{d_1}(E_{e_0},t)\rangle\ , \qquad (2.16)$$

with $\hat{\mathcal{H}}_{d_1} = \hat{H}_{d_1} - i\Gamma_{d_1}/2$.

Due to the presence of the photoelectron, Eq. (2.5) also contains an integration over E_{e_0}. To remove the integration, the formal solution of $|\psi_{d_1}(E_{e_0},t)\rangle$ (obtained from Eq. (2.16)) is inserted into Eq. (2.5), yielding

$$i|\dot{\psi}_i(t)\rangle = \hat{H}_i|\psi_i(t)\rangle - i\iint \mathrm{d}t'\mathrm{d}E_{e_0}\,\hat{F}^{\dagger}(E_{e_0},t)e^{i(\hat{\mathcal{H}}_{d_1}+E_{e_0})(t'-t)}\hat{F}(E_{e_0},t')|\psi_i(t')\rangle\ . \qquad (2.17)$$

After applying the local approximation to integrate the second term in Eq. (2.17), we arrive at the EOM for $|\psi_i(t)\rangle$, which reads

$$i|\dot{\psi}_i(t)\rangle = (\hat{H}_i - i\frac{\Gamma_{\mathrm{ph}}(\omega,t)}{2})|\psi_i(t)\rangle\ , \qquad (2.18)$$

where the ionization rate reads [40]

$$\Gamma_{\mathrm{ph}}(\omega,t) = 2\pi|\boldsymbol{\mu}\cdot\mathbf{E}(t)|^2 = \frac{\sigma_i(\omega)I(t)}{\omega}\ ,$$

with σ_i being the photoionization cross-section of state i (to d_1) under the photon energy ω, and $I(t)$ being the laser pulse intensity. A detailed derivation of the expression for Γ_{ph} is given in Appendix B.

Defining $\hat{\mathcal{H}}_i = \hat{H}_i - i\Gamma_{\mathrm{ph}}(t)/2$, we can summarize the EOMs for the single channel two-step decay process, initiated by photoionization, in matrix form as:

$$i\begin{pmatrix} \dot{\psi}_i \\ \dot{\psi}_{d_1} \\ \dot{\psi}_{d_2} \\ \dot{\psi}_f \end{pmatrix} = \begin{pmatrix} \hat{\mathcal{H}}_i & 0 & 0 & 0 \\ \hat{F}(t) & \hat{\mathcal{H}}_{d_1}+E_{e_0} & 0 & 0 \\ 0 & \hat{W}_{d_1\to d_2} & \hat{\mathcal{H}}_{d_2}+E_{e_0}+E_{e_1} & 0 \\ 0 & 0 & \hat{W}_{d_2\to f} & \hat{H}_f+E_{e_0}+E_{e_1}+E_{e_2} \end{pmatrix} \begin{pmatrix} \psi_i \\ \psi_{d_1} \\ \psi_{d_2} \\ \psi_f \end{pmatrix}. \qquad (2.19)$$

2.2 Equations of Motion for a Non-Separable Multi-Channel Two-Step Decay Process

In general, there could be multiple states involved in a decay process. These multiple states can be degenerate or non-degenerate. If the states are non-degenerate, the emitted electrons are separable by their energies and the decay channels are also separable. If the states are degenerate or almost degenerate, the emitted electrons become non-separable in energy, and so do the decay channels. In this section, we derive the EOMs for a non-separable multi-channel cascade decay process, while the separable multi-channel cascade decay process will be discussed in Sec. 2.3.

A schematic picture of such a multi-channel process is shown in Fig. 2.2, where there are two singly ionic states labeled as d_{1_α} with $\alpha = 1, 2$, two doubly ionic states labeled as d_{2_β} with $\beta = 1, 2$, and two triply ionic states labeled as f_γ with $\gamma = 1, 2$. For the current example, the two singly ionic states are chosen to be (almost) degenerate. The same is true for the two doubly ionic states and the two final states. Due to the fact that the states are degenerate, the electrons emitted from the partial channel[3] $d_{1_1} \to d_{2_\beta}$ are not separable from the electrons emitted from the partial channel $d_{1_2} \to d_{2_\beta}$ in energy, see Fig. 2.2. In consequence, the electrons emitted in the first decay process are all denoted as e_1, having a kinetic energy E_{e_1}, and the wave functions of the outgoing electrons are expanded by the same energy eigenfunctions. Similarly, the electrons emitted during the second decay process are denoted as e_2, whose kinetic energy is E_{e_2}. Additionally, the kinetic energy of the photoelectrons will be denoted by E_{e_0}.

The total wave function contains wave functions of all the states involved in the decay processes [26]. Using the Born-Oppenheimer approximation, it reads

$$\begin{aligned}|\Psi(t)\rangle = {} & |\Phi_i\rangle|\psi_i(t)\rangle + \sum_{\alpha=1}^{2} \int \mathrm{d}E_{e_0} |\Phi_{d_{1_\alpha}}, E_{e_0}\rangle|\psi_{d_{1_\alpha}}(E_{e_0}, t)\rangle \\ & + \sum_{\beta=1}^{2} \iint \mathrm{d}E_{e_0}\, \mathrm{d}E_{e_1} |\Phi_{d_{2_\beta}}, E_{e_0}, E_{e_1}\rangle|\psi_{d_{2_\beta}}(E_{e_0}, E_{e_1}, t)\rangle \\ & + \sum_{\gamma=1}^{2} \iiint \mathrm{d}E_{e_0}\, \mathrm{d}E_{e_1}\, \mathrm{d}E_{e_2} |\Phi_{f_\gamma}, E_{e_0}, E_{e_1}, E_{e_2}\rangle|\psi_{f_\gamma}(E_{e_0}, E_{e_1}, E_{e_2}, t)\rangle \,. \end{aligned} \tag{2.20}$$

As was explained in Sec. 2.1, $|\Phi_x\rangle$ and $|\psi_x(t)\rangle$ are the electronic and nuclear wave functions of the state x, respectively. The ionic states d_{1_α}, d_{2_β}, and f_γ are embedded in the continuum, and hence their electronic wave functions are augmented with the continuum wave function(s) of the outgoing electron(s). Accordingly, their nuclear wave functions are multiplied with the amplitude(s) of the continuum function(s). As before, the nuclear wave functions also depend on the nuclear degrees of freedom.

---

[3] A state-specific channel is termed as *partial* channel.

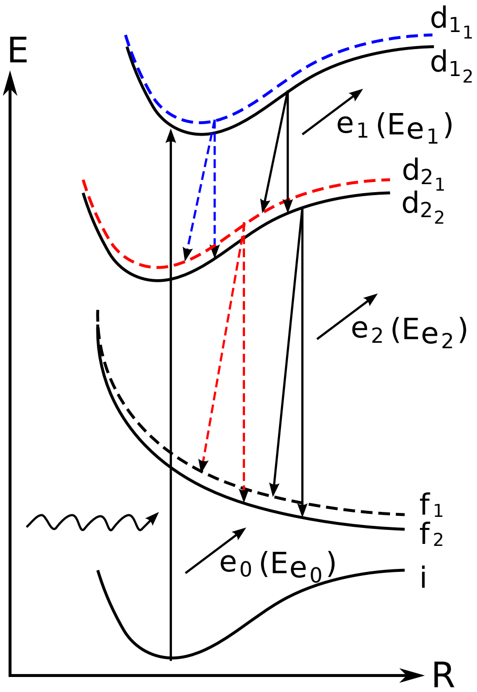

Figure 2.2: Schematic picture of a multi-channel cascade decay process. The potential energy curves are depicted for: (i) the electronic ground state (labeled as i), (ii) the degenerate singly ionic states (labeled as d_{1_α} with $\alpha = 1, 2$), (iii) the degenerate doubly ionic states (labeled as d_{2_β} with $\beta = 1, 2$), and (iv) the degenerate final states (labeled as f_γ with $\gamma = 1, 2$). The process is initiated by photoionization, followed successively by two electronic decay processes. There are four partial channels in each decay step, depicted by two dashed and two solid arrows. The emitted electrons e_1 from different partial channels are non-separable in energy because the involved states are degenerate. The same is true for electrons e_2.

Similar to Eq. (2.3), the electronic wave functions in Eq. (2.20) follow the orthonormalization rules:

$$\begin{aligned}
\langle \Phi_i | \Phi_i \rangle &= 1 \\
\langle \Phi_{d_{1_\alpha}}, E_{e_0} | \Phi_{d_{1_{\alpha'}}}, E'_{e_0} \rangle &= \delta_{\alpha,\alpha'}\, \delta(E_{e_0} - E'_{e_0}) \\
\langle \Phi_{d_{2_\beta}}, E_{e_0}, E_{e_1} | \Phi_{d_{2_{\beta'}}}, E'_{e_0}, E'_{e_1} \rangle &= \delta_{\beta,\beta'}\, \delta(E_{e_0} - E'_{e_0})\, \delta(E_{e_1} - E'_{e_1}) \qquad (2.21) \\
\langle \Phi_{f_\gamma}, E_{e_0}, E_{e_1}, E_{e_2} | \Phi_{f_{\gamma'}}, E'_{e_0}, E'_{e_1}, E'_{e_2} \rangle &= \delta_{\gamma,\gamma'}\, \delta(E_{e_0} - E'_{e_0})\, \delta(E_{e_1} - E'_{e_1})\, \delta(E_{e_2} - E'_{e_2})\ .
\end{aligned}$$

Both the Kronecker delta, e.g. $\delta_{\alpha,\alpha'}$, and Dirac delta function, e.g. $\delta(E_{e_0} - E'_{e_0})$, are employed to denote the orthonormal properties of the discrete states and continuum functions, respectively. In addition, electronic wave functions with different numbers of outgoing electrons are always orthogonal, e.g. $\langle \Phi_i | \Phi_{d_{1_\alpha}}, E_{e_0} \rangle = 0$.

Using the same total Hamiltonian as Eq. (2.4) and a similar procedure as in Sec. 2.1, we again obtain coupled equations for the nuclear wave functions. Projecting the total Schrödinger equation onto the electronic ground state i, the equation obtained for

$|\psi_i(t)\rangle$ reads:

$$i|\dot{\psi}_i(t)\rangle = \hat{H}_i|\psi_i(t)\rangle + \sum_{\alpha=1}^{2}\int dE_{e_0}\hat{F}_\alpha^\dagger(E_{e_0},t)|\psi_{d_{1_\alpha}}(E_{e_0},t)\rangle \ . \tag{2.22}$$

Different from Eq. (2.5), there is now a summation over α in the second term in Eq. (2.22), due to the presence of two singly ionic states. Projecting the total Schrödinger equation onto each singly ionic state, the equation for $|\psi_{d_\alpha}(E_{e_0},t)\rangle$, with $\alpha = 1, 2$, reads:

$$\begin{aligned} i|\dot{\psi}_{d_{1_\alpha}}(E_{e_0},t)\rangle &= \hat{F}_\alpha(E_{e_0},t)|\psi_i(t)\rangle + (\hat{H}_{d_{1_\alpha}} + E_{e_0})|\psi_{d_{1_\alpha}}(E_{e_0},t)\rangle \\ &+ \sum_{\beta=1}^{2}\int \mathrm{d}E_{e_1}\hat{W}^\dagger_{d_{1_\alpha}\to d_{2_\beta}}(E_{e_1})|\psi_{d_{2_\beta}}(E_{e_0},E_{e_1},t)\rangle \ . \end{aligned} \tag{2.23}$$

Note that there is a summation over β in the last term of the equation because there are two doubly ionic states in this example. Similarly, the projection of the total Schrödinger equation onto each doubly ionic state yields the equation for $|\psi_{d2_\beta}(E_{e_0},E_{e_1},t)\rangle$ with $\beta = 1, 2$, which reads

$$\begin{aligned} i|\dot{\psi}_{d_{2_\beta}}(E_{e_0},E_{e_1},t)\rangle &= \sum_{\alpha=1}^{2}\hat{W}_{d_{1_\alpha}\to d_{2_\beta}}(E_{e_1})|\psi_{d_{1_\alpha}}(E_{e_0},t)\rangle \\ &+ (\hat{H}_{d_{2_\beta}} + E_{e_0} + E_{e_1})|\psi_{d_{2_\beta}}(E_{e_0},E_{e_1},t)\rangle \\ &+ \sum_{\gamma=1}^{2}\int dE_{e_2}\hat{W}^\dagger_{d_{2_\beta}\to f_\gamma}|\psi_{f_\gamma}(E_{e_0},E_{e_1},E_{e_2},t)\rangle \ . \end{aligned} \tag{2.24}$$

Comparing Eq. (2.24) to Eq. (2.7), one finds two differences: First, there is a summation over α in the first term of the right hand side (RHS) of the equation, since both states d_{1_1} and d_{1_2} can decay to state $d_{2\beta}$, see Fig. 2.2. Second, there is a summation over γ in the last term of the RHS of the equation, since both final states can couple to state d_{2_β}. Finally, projecting the total Schrödinger equation onto each final state ($\gamma = 1, 2$), the equation for $|\psi_{f_\gamma}(E_{e_0},E_{e_1},E_{e_2},t)\rangle$ reads

$$\begin{aligned} i|\dot{\psi}_{f_\gamma}(E_{e_0},E_{e_1},E_{e_2},t)\rangle &= \sum_{\beta=1}^{2}\hat{W}_{d_{2_\beta}\to f_\gamma}(E_{e2})|\psi_{d_{2_\beta}}(E_{e_0},E_{e_1},t)\rangle \\ &+ (\hat{H}_{f_\gamma} + E_{e_0} + E_{e_1} + E_{e_2})|\psi_{f_\gamma}(E_{e_0},E_{e_1},E_{e_2},t)\rangle \ . \end{aligned} \tag{2.25}$$

Since both states d_{2_1} and d_{2_2} can decay to state f_γ (see Fig. 2.2) there is a summation over β in the first term of the RHS of Eq. (2.25).

As before, $\hat{H}_x$ denotes the nuclear Hamiltonian of state x. Due to the presence of multiple states, the transition matrix elements now read

$$\hat{W}_{d_{1_\alpha}\to d_{2_\beta}}(E_{e_1}) = \langle\Phi_{d_{2_\beta}}, E_{e_1}|\hat{H}_{\mathrm{el}}|\Phi_{d_{1_\alpha}}\rangle \ \text{ and } \ \hat{W}_{d_{2_\beta}\to f_\gamma}(E_{e_2}) = \langle\Phi_{f_\gamma}, E_{e_2}|\hat{H}_{\mathrm{el}}|\Phi_{d_{2_\beta}}\rangle \ ,$$

while the interaction between the molecule and the external field is given by[4]

$$\hat{F}_\alpha(E_{e_0}, t) = \boldsymbol{\mu}_\alpha \cdot \mathbf{E}(t) \ .$$

Eqs. (2.24-2.25) are equations for the degenerate states, and the emitted electrons are energetically non-separable. If the emitted electrons from different partial channels are separable in energy, the wave functions of the outgoing electrons can be expanded into different energy eigenfunctions. As a consequence, the summation over the different source term in Eqs. (2.24-2.25) will reduce to only one source term, due to the energy conservation and the ortho-normalization properties of the wave functions. See Sec. 2.3 for details on such a separable multi-channel cascade decay process.

As in Sec. 2.1, the local approximation [26] is applied to carry out the energy integration in Eqs. (2.22-2.24). To proceed, the formal solution for $|\psi_{f_\gamma}(E_{e0}, E_{e_1}, E_{e_2}, t)\rangle$, which can be obtained from Eq. (2.25), is inserted into Eq. (2.24). This yields

$$\begin{aligned} i|\dot{\psi}_{d_{2_\beta}}(E_{e_0}, E_{e_1}, t)\rangle &= \sum_{\alpha=1}^{2} \hat{W}_{d_{1_\alpha}\to d_{2_\beta}}(E_{e_1})|\psi_{d_{1_\alpha}}(E_{e_0}, t)\rangle + (\hat{H}_{d_{2_\beta}} + E_{e_0} + E_{e_1})|\psi_{d_{2_\beta}}(E_{e_0}, E_{e_1}, t)\rangle \\ - i\sum_{\gamma=1}^{2}\sum_{\beta'=1}^{2} &\iint \mathrm{d}t'\mathrm{d}E_{e_2}\, \hat{W}^\dagger_{d_{2_\beta}\to f_\gamma}(E_{e_2}) e^{i(\hat{H}_{f_\gamma}+E_{e_0}+E_{e_1}+E_{e_2})(t'-t)} \hat{W}_{d_{2_{\beta'}}\to f_\gamma}(E_{e_2})|\psi_{d_{2_{\beta'}}}(E_{e_0}, E_{e_1}, t')\rangle. \end{aligned} \tag{2.26}$$

The last term of the RHS of Eq. (2.26) again contains integrations over E_{e_2} and t. It can be integrated by using the local approximation [26] (see also Appendix A), leading to

$$\begin{aligned} &- i\sum_{\gamma=1}^{2}\sum_{\beta'=1}^{2} \iint \mathrm{d}t'\mathrm{d}E_{e_2}\, \hat{W}^\dagger_{d_{2_\beta}\to f}(E_{e_2}) e^{i(\hat{H}_{f_\gamma}+E_{e_0}+E_{e_1}+E_{e_2})(t'-t)} \hat{W}_{d_{2_{\beta'}}\to f_\gamma}(E_{e_2})|\psi_{d_{2_{\beta'}}}(E_{e_0}, E_{e_1}, t')\rangle \\ &\approx -i\sum_{\gamma=1}^{2}\sum_{\beta'=1}^{2} \pi \hat{W}^\dagger_{d_{2_\beta}\to f_\gamma} \hat{W}_{d_{2_{\beta'}}\to f_\gamma}|\psi_{d_{2_{\beta'}}}(E_{e_0}, E_{e_1}, t)\rangle \ . \end{aligned} \tag{2.27}$$

After the local approximation, operators $\hat{W}_{d_{2_\beta}}$ and $\hat{W}_{d_{2_{\beta'}}}$ do not depend on E_{e_2} anymore. The summation over β' in Eq. (2.27) can be divided into two parts: $\beta' = \beta$ and $\beta' \neq \beta$. For the part $\beta' = \beta$, it reads

$$\begin{aligned} &-i\sum_{\gamma} \pi \hat{W}^\dagger_{d_{2_\beta}\to f_\gamma} \hat{W}_{d_{2_\beta}\to f_\gamma}|\psi_{d_{2_\beta}}(E_{e_0}, E_{e_1}, t)\rangle \\ &= \frac{-i}{2}\sum_{\gamma} \Gamma^{(\gamma)}_\beta |\psi_{d_{2_\beta}}(E_{e_0}, E_{e_1}, t)\rangle = \frac{-i}{2}\Gamma_\beta |\psi_{d_{2_\beta}}(E_{e_0}, E_{e_1}, t)\rangle \ , \end{aligned}$$

---

[4] $\boldsymbol{\mu}_\alpha = \langle \Phi_{d_{1_\alpha}}, E_{e_0}|\hat{\mathbf{D}}|\Phi_i\rangle$.

where $\Gamma_\beta^{(\gamma)}$ denotes the partial decay rate from state d_{2_β} to state f_γ, and Γ_β denotes the total decay rate of state d_{2_β}. For $\beta' \neq \beta$, Eq. (2.27) yields

$$\begin{aligned}
&-i\sum_{\gamma}\sum_{\beta'\neq\beta}\pi\hat{W}^\dagger_{d_{2_\beta}\to f_\gamma}\hat{W}_{d_{2_{\beta'}}\to f_\gamma}|\psi_{d_{2_{\beta'}}}(E_{e_0},E_{e_1},t)\rangle \\
&=\frac{-i}{2}\sum_{\gamma}\sum_{\beta'\neq\beta}\Lambda^{(\gamma)}_{\beta,\beta'}|\psi_{d_{2_{\beta'}}}(E_{e_0},E_{e_1},t)\rangle=\frac{-i}{2}\sum_{\beta'\neq\beta}\Lambda_{\beta,\beta'}|\psi_{d_{2_{\beta'}}}(E_{e_0},E_{e_1},t)\rangle\ ,
\end{aligned}$$

where $\Lambda^{(\gamma)}_{\beta,\beta'}$ (implicitly defined by the equation above) denotes the partial *interchannel interference via continuum* from state $d_{2_{\beta'}}$ to state d_{2_β} via state f_γ. This term can be pictured as a two-step process: First, state $d_{2_{\beta'}}$ decays to state f_γ via emitting an electron e_2 with energy E_{e_2}. The electron then immediately recombines with the final state again, coupling back to state d_{2_β}. This process is energetically allowed due to the degeneracy of the states. If states d_{2_1} and d_{2_2} were not degenerate, the "transition back to another state" would be forbidden due to the law of energy conservation. Therefore, the interchannel coupling via continuum is only non-zero if the intermediate states are nearly degenerate, i.e. the emitted electrons are non-separable by their energies. Summation of $\Lambda^{(\gamma)}_{\beta,\beta'}$ over all γ yields the total interchannel interference via continuum from state $d_{2_{\beta'}}$ to state d_{2_β}; it is denoted by $\Lambda_{\beta,\beta'}$. After the local approximation, Eq. (2.26) becomes

$$\begin{aligned}
i|\dot{\psi}_{d_{2_\beta}}(E_{e_0},E_{e_1},t)\rangle &= \sum_{\alpha}\hat{W}_{d_{1_\alpha}\to d_{2_\beta}}(E_{e_1})|\psi_{d_{1_\alpha}}(E_{e_0},t)\rangle - i\sum_{\beta'\neq\beta}^{2}\frac{\Lambda_{\beta,\beta'}}{2}|\psi_{d_{2_{\beta'}}}(E_{e_0},E_{e_1},t)\rangle \\
&\quad + (\hat{\mathcal{H}}_{d_{2_\beta}}+E_{e_0}+E_{e_1})|\psi_{d_{2_\beta}}(E_{e_0},E_{e_1},t)\rangle\ , \qquad (2.28)
\end{aligned}$$

with $\hat{\mathcal{H}}_{d_{2_\beta}} = \hat{H}_{d_{2_\beta}} - i\Gamma_\beta/2$.

Similarly, to carry out the integration over E_{e_1} in Eq. (2.23), the formal solution for $|\psi_{d_{2_\beta}}(E_{e_0},E_{e_1},t)\rangle$, obtained from rearranging Eq. (2.28), is inserted into Eq. (2.23), which then reads

$$\begin{aligned}
&i|\dot{\psi}_{d_{1_\alpha}}(E_{e_0},t)\rangle = \hat{F}_\alpha(t)|\psi_i(t)\rangle + (\hat{H}_{d_{1_\alpha}}+E_{e_0})|\psi_{d_{1_\alpha}}(E_{e_0},t)\rangle \\
&-i\sum_{\beta=1}^{2}\sum_{\alpha'=1}^{2}\iint \mathrm{d}t'\mathrm{d}E_{e_1}\,\hat{W}^\dagger_{d_{1_\alpha}\to d_{2_\beta}}(E_{e_1})e^{i(\hat{\mathcal{H}}_{d_{2_\beta}}+E_{e_0}+E_{e_1})(t'-t)}\hat{W}_{d_{1_{\alpha'}}\to d_{2_\beta}}(E_{e_1})|\psi_{d_{1_{\alpha'}}}(E_{e_0},t')\rangle \\
&-\sum_{\beta=1}^{2}\sum_{\beta'\neq\beta}^{2}\iint \mathrm{d}t'\mathrm{d}E_{e_1}\,\hat{W}^\dagger_{d_{1_\alpha}\to d_{2_\beta}}(E_{e_1})e^{i(\hat{\mathcal{H}}_{d_{2_\beta}}+E_{e_0}+E_{e_1})(t'-t)}\frac{\Lambda_{\beta,\beta'}}{2}|\psi_{d_{2_{\beta'}}}(E_{e_0},E_{e_1},t')\rangle.
\end{aligned}$$
$$(2.29)$$

The last two terms in the RHS of Eq. (2.29) both contain the integrations over t and

E_{e_1}. Applying the local approximation to the second last term yields

$$\begin{aligned} & -i\sum_{\beta}\sum_{\alpha'}\iint \mathrm{d}t'\mathrm{d}E_{e_1}\,\hat{W}^{\dagger}_{d_{1_\alpha}\to d_{2_\beta}}(E_{e_1})e^{i(\hat{\mathcal{H}}_{d_{2_\beta}}+E_{e_0}+E_{e_1})(t'-t)}\hat{W}_{d_{1_{\alpha'}}\to d_{2_\beta}}(E_{e_1})|\psi_{d_{1_{\alpha'}}}(E_{e_0},t')\rangle \\ & \approx -i\sum_{\beta}\sum_{\alpha'}\pi\hat{W}^{\dagger}_{d_{1_\alpha}\to d_{2_\beta}}\hat{W}_{d_{1_{\alpha'}}\to d_{2_\beta}}|\psi_{d_{1_{\alpha'}}}(E_{e_0},t)\rangle\ , \end{aligned} \tag{2.30}$$

which, as in Eq. (2.27), is divided into two parts ($\alpha'=\alpha$ and $\alpha'\neq\alpha$), leading to

$$\begin{aligned} & -i\sum_{\beta}\sum_{\alpha'}\pi\hat{W}^{\dagger}_{d_{1_\alpha}\to d_{2_\beta}}\hat{W}_{d_{1_{\alpha'}}\to d_{2_\beta}}|\psi_{d_{1_{\alpha'}}}(E_{e_0},t)\rangle \\ &= -i\sum_{\beta}\frac{\Gamma^{(\beta)}_{\alpha}}{2}|\psi_{d_{1_\alpha}}(E_{e_0},t)\rangle - i\sum_{\beta}\sum_{\alpha'\neq\alpha}\frac{\Lambda^{(\beta)}_{\alpha,\alpha'}}{2}|\psi_{d_{1_{\alpha'}}}(E_{e_0},t)\rangle \\ &= -i\frac{\Gamma_{\alpha}}{2}|\psi_{d_{1_\alpha}}(E_{e_0},t)\rangle - i\sum_{\alpha'\neq\alpha}\frac{\Lambda_{\alpha,\alpha'}}{2}|\psi_{d_{1_{\alpha'}}}(E_{e_0},t)\rangle\ . \end{aligned}$$

As before, $\Gamma^{(\beta)}_{\alpha}$ denotes the partial decay rate from state d_{1_α} to d_{2_β}, while Γ_α denotes the total decay rate of state d_{1_α}. Furthermore, $\Lambda^{(\beta)}_{\alpha,\alpha'}$ denotes the partial interchannel interference via continuum from state $d_{1_{\alpha'}}$ through state d_{2_β} to state d_{1_α}. The total interchannel interference from state $d_{1_{\alpha'}}$ to d_{1_α} is denoted by $\Lambda_{\alpha,\alpha'}$.

On the other hand, applying the local approximation to the last term in the RHS of Eq. (2.29) yields

$$-\sum_{\beta=1}^{2}\sum_{\beta'\neq\beta}^{2}\iint \mathrm{d}t'\mathrm{d}E_{e_1}\,\hat{W}^{\dagger}_{d_{1_\alpha}\to d_{2_\beta}}(E_{e_1})e^{i(\hat{\mathcal{H}}_{d_{2_\beta}}+E_{e_0}+E_{e_1})(t'-t)}\frac{\Lambda_{\beta,\beta'}}{2}|\psi_{d_{2_{\beta'}}}(E_{e_0},E_{e_1},t')\rangle \approx 0\ .$$

Note that $|\psi_{d_{2_{\beta'}}}(E_{e_0},E_{e_1},t')\rangle$ also depends on E_{e_1}, producing a rapidly oscillating phase for each $|\psi_{d_{2_{\beta'}}}(E_{e_0},E_{e_1},t')\rangle$. Integrating over E_{e_1} then leads to destructive interferences and gives zero. See Appendix C for details.

After applying the local approximation, the EOM for $|\psi_{d_{1_\alpha}}(E_{e_0},t)\rangle$ then reads,

$$i|\dot{\psi}_{d_{1_\alpha}}(E_{e_0},t)\rangle = \hat{F}_{\alpha}(t)|\psi_i(t)\rangle + (\hat{\mathcal{H}}_{d_{1_\alpha}}+E_{e_0})|\psi_{d_{1_\alpha}}(E_{e_0},t)\rangle - i\sum_{\alpha'\neq\alpha}^{2}\frac{\Lambda_{\alpha,\alpha'}}{2}|\psi_{d_{1_{\alpha'}}}(E_{e_0},t)\rangle\ , \tag{2.31}$$

where $\hat{\mathcal{H}}_{d_{1_\alpha}} = \hat{H}_{d_{1_\alpha}} - i\Gamma_\alpha/2$.

Similar to the procedure in Sec. 2.1, using Eq. (2.31) and the local approximation, Eq. (2.22) becomes

$$i|\dot{\psi}_i(t)\rangle = (\hat{H}_i - i\frac{\Gamma_{\mathrm{ph}}(\omega,t)}{2})|\psi_i(t)\rangle\ , \tag{2.32}$$

where the total ionization rate $\Gamma_{\text{ph}}(\omega,t)$ is given by a sum over all partial ionization rates, namely,

$$\Gamma_{\text{ph}}(\omega,t) = \sum_{\alpha} \frac{\sigma_\alpha(\omega)I(t)}{\omega} = \frac{\sigma_i(\omega)I(t)}{\omega} \ ,$$

where $\sigma_\alpha(\omega)$ is the ionization cross-section from state i to state d_{1_α} at the photon frequency ω, and $I(t)$ denotes the laser intensity. The total ionization cross-section of state i, i.e. $\sigma_i(\omega)$, naturally is given by the summation over the cross-sections to all states d_{1_α}.

To sum up, the EOMs for the non-separable multi-channel two-step decay process, initiated by photoionization, can be generalized from the previous derivations. The degeneracy of states d_{1_α}, states d_{2_β}, and states f_γ is denoted by N_{d_1}, N_{d_2}, and N_f, respectively. For a case as shown in Fig. 2.2, N_{d_1}, N_{d_2}, and N_f are all equal to 2. The EOM of the electronic ground state i reads,

$$i|\dot{\psi}_i(t)\rangle = (\hat{H}_i - i\frac{\Gamma_{\text{ph}}(\omega,t)}{2})|\psi_i(t)\rangle \ . \tag{2.33}$$

For the degenerate states d_{1_α} ($\alpha = 1,\cdots,N_{d_1}$), the EOM of each state d_{1_α} has the same form:

$$i|\dot{\psi}_{d_{1_\alpha}}(E_{e_0},t)\rangle = \hat{F}_\alpha(t)|\psi_i(t)\rangle + (\hat{\mathcal{H}}_{d_{1_\alpha}} + E_{e_0})|\psi_{d_{1_\alpha}}(E_{e_0},t)\rangle - i\sum_{\alpha'\neq\alpha}^{N_{d_1}} \frac{\Lambda_{\alpha,\alpha'}}{2}|\psi_{d_{1_{\alpha'}}}(E_{e_0},t)\rangle \ . \tag{2.34}$$

The doubly ionic states d_{2_β} are also degenerate ($\beta = 1,\cdots,N_{d_2}$), and the EOM for each state is given by:

$$\begin{aligned} i|\dot{\psi}_{d_{2_\beta}}(E_{e_0},E_{e_1},t)\rangle = &\sum_{\alpha=1}^{N_{d_1}} \hat{W}_{d_{1_\alpha}\to d_{2_\beta}}|\psi_{d_{1_\alpha}}(E_{e_0},t)\rangle - i\sum_{\beta'\neq\beta}^{N_{d_2}} \frac{\Lambda_{\beta,\beta'}}{2}|\psi_{d_{2_{\beta'}}}(E_{e_0},E_{e_1},t)\rangle \\ &+ (\hat{\mathcal{H}}_{d_{2_\beta}} + E_{e_0} + E_{e_1})|\psi_{d_{2_\beta}}(E_{e_0},E_{e_1},t)\rangle \ . \end{aligned} \tag{2.35}$$

Finally, the EOM for each state f_γ ($\gamma = 1,\cdots,N_f$) reads,

$$\begin{aligned} i|\dot{\psi}_{f_\gamma}(E_{e_0},E_{e_1},E_{e_2},t)\rangle = &\sum_{\beta=1}^{N_{d_2}} \hat{W}_{d_{2_\beta}\to f_\gamma}|\psi_{d_{2_\beta}}(E_{e_0},E_{e_1},t)\rangle \\ &+ (\hat{H}_{f_\gamma} + E_{e_0} + E_{e_1} + E_{e_2})|\psi_{f_\gamma}(E_{e_0},E_{e_1},E_{e_2},t)\rangle \ . \end{aligned} \tag{2.36}$$

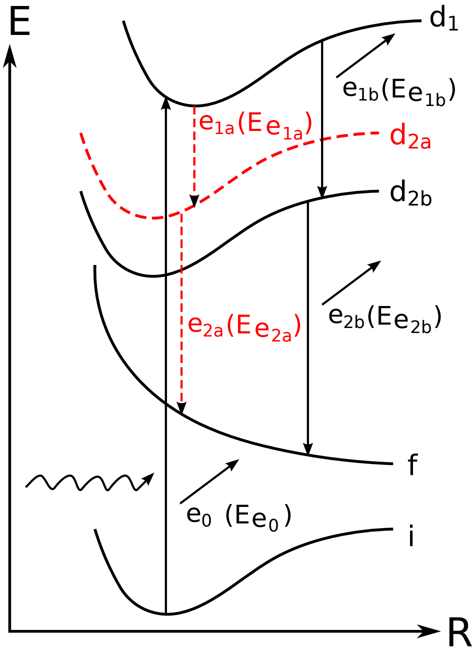

Figure 2.3: Schematic picture of a two-channel two-step decay process. The potential energy curves of the electronic ground state (labeled as i), the singly ionic state (labeled as d_1), the doubly ionic states (labeled as d_{2_a} and d_{2_b}), and the final state (labeled as f) are depicted. After photoionization, state d_1 can decay via two separable partial channels, i.e. via state d_{2_a} to state f or via state d_{2_b} to state f.

2.3 Equations for a Separable Multi-Channel Two-Step Decay Process

In this section, a separable multi-channel decay process is discussed. A simple two-channel two-step decay process is chosen as an example, see Fig. 2.3. The electronic states i, d_1, f are chosen to be non-degenerate. The two doubly ionic states are labeled by d_{2a} and d_{2b} and are well-separated in energy.

After phototionization, the system is ionized to the electronically excited ionic state d_1, which then decays to either state d_{2a} or state d_{2b}. Since states d_{2a} and d_{2b} are well separated in energy, i.e. the emitted electrons are separable in energy, the electron emitted from the partial channel $d_1 \to d_{2a}$ is denoted by e_{1a} with a kinetic energy $E_{e_{1a}}$, and the electron emitted from the other partial channel is denoted by e_{1b} with a kinetic energy $E_{e_{1b}}$, see Fig. 2.3. Following the separable partial channels in the first decay process, the two partial channels in the second decay process are also separable. The electron emitted from the partial channel $d_{2a} \to f$ is denoted by e_{2a} with a kinetic energy $E_{e_{2a}}$. Similarly, the electron emitted from the partial channel $d_{2b} \to f$ is denoted by e_{2b}, having a kinetic energy $E_{e_{2b}}$. Again, we stress that $E_{e_{1a}}$ and $E_{e_{1b}}$ are well-separated in energy, and so are $E_{e_{2a}}$ and $E_{e_{2b}}$.

The total wave function ansatz for the process depicted in Fig. 2.3 reads

$$\begin{aligned}|\Psi(t)\rangle = |\Phi_i\rangle|\psi_i(t)\rangle &+ \int \mathrm{d}E_{e0}|\Phi_{d_1}, E_{e0}\rangle|\psi_{d_1}(E_{e0}, t)\rangle \\ &+ \iint \mathrm{d}E_{e0}\ \mathrm{d}E_{e_{1a}}|\Phi_{d_{2a}}, E_{e0}, E_{e_{1a}}\rangle|\psi_{d_{2a}}(E_{e0}, E_{e_{1a}}, t)\rangle \\ &+ \iint \mathrm{d}E_{e0}\ \mathrm{d}E_{e_{1b}}|\Phi_{d_{2b}}, E_{e0}, E_{e_{1b}}\rangle|\psi_{d_{2b}}(E_{e0}, E_{e_{1b}}, t)\rangle \\ &+ \iiint \mathrm{d}E_{e0}\ \mathrm{d}E_{e_1}\ \mathrm{d}E_{e_2}|\Phi_f, E_{e0}, E_{e_1}, E_{e_2}\rangle|\psi_f(E_{e0}, E_{e_1}, E_{e_2}, t)\rangle\ . \end{aligned} \tag{2.37}$$

As before, $|\Phi_x\rangle$ and $|\psi_x(t)\rangle$ denote the electronic and nuclear wave functions of state x, respectively. The ionic state d_1 is embedded in the continuum, and consequently, its wave function is augmented with the wave function of the photoelectron. Similarly, the doubly ionic states d_{2a} and d_{2b} are embedded in continuum, and their wave functions are augmented with the respective wave functions of the photoelectron and the emitted electron. Since the emitted electrons from the two different partial channels are separable, the wave functions of e_{1a} and e_{1b} can be expanded by continuum energy eigenfunctions with different energy. The final state is also embedded in the continuum and its wave function is augmented with the wave functions of the outgoing electrons. However, the label of the continuum energy eigenfunctions are kept as E_{e_1} and E_{e_2} instead of $E_{e_{1a}}$ and $E_{e_{2a}}$, due to the fact that both states d_{2a} and d_{2b} can populate the final state. Later in the discussion the values of E_{e_1} and E_{e_2} will be determined.

The electronic wave functions used in Eq. (2.37) obey the same ortho-normalization rules as shown in Sec. 2.3. Also, the electronic wave functions provide the following transition matrix elements

$$\begin{aligned}\langle\Phi_{d_{2a}}, E_{e0}, E_{e_{1a}}|\hat{H}_{\mathrm{el}}|\Phi_{d_1}, E_{e0}\rangle &= \langle\Phi_{d_{2a}}, E_{e_{1a}}|\hat{H}_{\mathrm{el}}|\Phi_{d_1}\rangle = \hat{W}_{d_1\to d_{2a}}(E_{e_{1a}})\ , \\ \langle\Phi_{d_{2b}}, E_{e0}, E_{e_{1b}}|\hat{H}_{\mathrm{el}}|\Phi_{d_1}, E_{e0}\rangle &= \langle\Phi_{d_{2b}}, E_{e_{1b}}|\hat{H}_{\mathrm{el}}|\Phi_{d_1}\rangle = \hat{W}_{d_1\to d_{2b}}(E_{e_{1b}})\ . \end{aligned} \tag{2.38}$$

Since the two partial channels to state f are separable, the corresponding transition matrix elements to state f are naturally distinguishable. For example, the transition matrix element from state d_{2a} to state f reads

$$\begin{aligned}&\langle\Phi_f, E_{e0}, E_{e_1}, E_{e_2}|\hat{H}_{\mathrm{el}}|\Phi_{d_{2a}}, E_{e0}, E_{e_{1a}}\rangle \\ &= \langle\Phi_f, E_{e_2}|\hat{H}_{\mathrm{el}}|\Phi_{d_{2a}}\rangle\,\delta(E_{e_1} - E_{e_{1a}}) \\ &= \hat{W}_{d_{2a}\to f}(E_{e_2})\,\delta(E_{e_1} - E_{e_{1a}})\ .\end{aligned}$$

The term $\hat{W}_{d_{2a}\to f}(E_{e_2})$ is only non-zero when E_{e_2} is inside the possible range of value for $E_{e_{2a}}$, i.e. $E_{e_2} = E_{e_{2a}}$, due to the law of energy conservation. Note that ranges for $E_{e_{2a}}$ and $E_{e_{2b}}$ are not overlap; see also Fig. 2.3. Similarly, the transition element of state d_{2b} to state f reads,

$$\begin{aligned}&\langle\Phi_f, E_{e_0}, E_{e_1}, E_{e_2}|\hat{H}_{\mathrm{el}}|\Phi_{d_{2b}}, E_{e_0}, E_{e_{1b}}\rangle\\&= \langle\Phi_f, E_{e_2}|\hat{H}_{\mathrm{el}}|\Phi_{d_{2b}}\rangle\,\delta(E_{e_1} - E_{e_{1b}})\\&= \hat{W}_{d_{2b}\to f}(E_{e_2})\,\delta(E_{e_1} - E_{e_{1b}})\ ,\end{aligned}$$

and $\hat{W}_{d_{2b}\to f}(E_{e_2})$ is only non-zero when E_{e_2} equals $E_{e_{2b}}$.

Using the same total Hamiltonian as shown in Eq. (2.4), the time-dependent Schrödinger equation of the total system is projected onto each electronic state. For the initial state, the equation reads

$$i|\dot{\psi}_i(t)\rangle = \hat{H}_i|\psi_i(t)\rangle + \int dE_{e_0}\hat{F}^\dagger(E_{e_0}, t)|\psi_{d_1}(E_{e_0}, t)\rangle\ . \tag{2.39}$$

This equation is identical to Eq. (2.5). Projecting onto the state d_1, we get

$$\begin{aligned}&i|\dot{\psi}_{d_1}(E_{e_0}, t)\rangle = \hat{F}(E_{e_0}, t)|\psi_i(t)\rangle + (\hat{H}_{d_1} + E_{e_0})|\psi_{d_1}(E_{e_0}, t)\rangle +\\&\int \mathrm{d}E_{e_{1a}}\hat{W}^\dagger_{d_1\to d_{2a}}(E_{e_{1a}})|\psi_{d_{2a}}(E_{e_0}, E_{e_{1a}}, t)\rangle + \int \mathrm{d}E_{e_{1b}}\hat{W}^\dagger_{d_1\to d_{2b}}(E_{e_{1b}})|\psi_{d_{2b}}(E_{e_0}, E_{e_{1b}}, t)\rangle,\end{aligned} \tag{2.40}$$

which is very similar to Eq. (2.6), except that now there are two doubly ionic states coupled to state d_1 in Eq. (2.40). The equations for state d_{2a} and d_{2b} are also obtained from projecting the total Schrödinger equation onto these states. The equations read

$$\begin{aligned}i|\dot{\psi}_{d_{2a}}(E_{e_0}, E_{e_{1a}}, t)\rangle &= \hat{W}_{d_1\to d_{2a}}(E_{e_{1a}})|\psi_{d_1}(E_{e_0}, t)\rangle + (\hat{H}_{d_{2a}} + E_{e_0} + E_{e_{1a}})|\psi_{d_{2a}}(E_{e_0}, E_{e_{1a}}, t)\rangle\\&+ \int dE_{e_{2a}}\hat{W}^\dagger_{d_{2a}\to f}(E_{e_{2a}})|\psi_f(E_{e_0}, E_{e_{1a}}, E_{e_{2a}}, t)\rangle\ ,\end{aligned} \tag{2.41}$$

and

$$\begin{aligned}i|\dot{\psi}_{d_{2b}}(E_{e_0}, E_{e_{1b}}, t)\rangle &= \hat{W}_{d_1\to d_{2b}}(E_{e_{1b}})|\psi_{d_1}(E_{e_0}, t)\rangle + (\hat{H}_{d_{2b}} + E_{e_0} + E_{e_{1b}})|\psi_{d_{2b}}(E_{e_0}, E_{e_{1b}}, t)\rangle\\&+ \int dE_{e_{2b}}\hat{W}^\dagger_{d_{2b}\to f}(E_{e_{2b}})|\psi_f(E_{e_0}, E_{e_{1b}}, E_{e_{2b}}, t)\rangle\ .\end{aligned} \tag{2.42}$$

It has been used in Eq. (2.41) that the transition matrix element $\hat{W}_{d_{2a}\to f}$ is non-zero only when E_{e_2} equals $E_{e_{2a}}$. The same holds for $E_{e_{2b}}$ in Eq. (2.42). Interestingly, the formulations of Eq. (2.41) and of Eq. (2.42) are identical, apart from the label a and b.

What will happen when the total Schrödinger equation is projected onto the final electronic state? Due to the separation of the channels, the final electronic state is either $|\Phi_f, E_{e_0}, E_{e_{1a}}, E_{e_{2a}}\rangle$ or $|\Phi_f, E_{e_0}, E_{e_{1b}}, E_{e_{2b}}\rangle$, depending on the channel. Hence, the projection yields two equations, namely

$$\begin{aligned}i|\dot{\psi}_f(E_{e_0}, E_{e_{1a}}, E_{e_{2a}}, t)\rangle &= \hat{W}_{d_{2a}\to f}(E_{e_{2a}})|\psi_{d_{2a}}(E_{e_0}, E_{e_{1a}}, t)\rangle\\&+ (\hat{H}_f + E_{e_0} + E_{e_{1a}} + E_{e_{2a}})|\psi_f(E_{e_0}, E_{e_{1a}}, E_{e_{2a}}, t)\rangle\ ,\end{aligned} \tag{2.43}$$

and

$$\begin{aligned} i|\dot{\psi}_f(E_{e_0}, E_{e_{1b}}, E_{e_{2b}}, t)\rangle &= \hat{W}_{d_{2b}\to f}(E_{e_{2b}})|\psi_{d_{2b}}(E_{e_0}, E_{e_{1b}}, t)\rangle \\ &+ (\hat{H}_f + E_{e_0} + E_{e_{1b}} + E_{e_{2b}})|\psi_f(E_{e_0}, E_{e_{1b}}, E_{e_{2b}}, t)\rangle \; . \qquad (2.44) \end{aligned}$$

Again, the formulations of Eq. (2.43) and Eq. (2.44) are the same, except for the label a and b. In consequence, the equations for states d_{2a}, d_{2b}, and f can be separated into two groups, according to the energy of the emitted electron, which depends on the partial channel.

Following the same procedure as in Sec. 2.1, the local approximation has been applied to the coupled equations, yielding the EOMs for the system. For the partial channel passing through state d_{2a} (red dashed line in Fig. 2.3), the EOMs of states d_{2a} and f read

$$\begin{aligned} i|\dot{\psi}_{d_{2a}}(E_{e_0}, E_{e_{1a}}, t)\rangle &= \hat{W}_{d_1\to d_{2a}}|\psi_{d_1}(E_{e_0}, t)\rangle \\ &+ (\hat{\mathcal{H}}_{d_{2a}} + E_{e_0} + E_{e_{1a}})|\psi_{d_{2a}}(E_{e_0}, E_{e_{1a}}, t)\rangle \; , \qquad (2.45) \\ i|\dot{\psi}_f(E_{e_0}, E_{e_{1a}}, E_{e_{2a}}, t)\rangle &= \hat{W}_{d_{2a}\to f}|\psi_{d_{2a}}(E_{e_0}, E_{e_{1a}}, t)\rangle \\ &+ (\hat{H}_f + E_{e_0} + E_{e_{1a}} + E_{e_{2a}})|\psi_f(E_{e_0}, E_{e_{1a}}, E_{e_{2a}}, t)\rangle \; , \qquad (2.46) \end{aligned}$$

respectively. If the partial channel goes through state d_{2b} (black solid line in Fig. 2.3), the EOMs of the relevant states then are given by

$$\begin{aligned} i|\dot{\psi}_{d_{2b}}(E_{e_0}, E_{e_{1b}}, t)\rangle &= \hat{W}_{d_1\to d_{2b}}|\psi_{d_1}(E_{e_0}, t)\rangle \\ &+ (\hat{\mathcal{H}}_{d_{2b}} + E_{e_0} + E_{e_{1b}})|\psi_{d_{2b}}(E_{e_0}, E_{e_{1b}}, t)\rangle \; , \qquad (2.47) \\ i|\dot{\psi}_f(E_{e_0}, E_{e_{1b}}, E_{e_{2b}}, t)\rangle &= \hat{W}_{d_{2b}\to f}|\psi_{d_{2b}}(E_{e_0}, E_{e_{1b}}, t)\rangle \\ &+ (\hat{H}_f + E_{e_0} + E_{e_{1b}} + E_{e_{2b}})|\psi_f(E_{e_0}, E_{e_{1b}}, E_{e_{2b}}, t)\rangle \; . \qquad (2.48) \end{aligned}$$

Obviously, Eqs. (2.45-2.46) and Eqs. (2.47-2.48) are formally equivalent, but they describe the nuclear motions taking place within two different partial channels. The EOMs for states i and d_1 are also obtained after the local approximation, and they read

$$\begin{aligned} i|\dot{\psi}_i(t)\rangle &= \hat{\mathcal{H}}_i|\psi_i(t)\rangle \; , \qquad (2.49) \\ i|\dot{\psi}_{d_1}(E_{e_0}, t)\rangle &= \hat{F}(E_{e_0}, t)|\psi_i(t)\rangle + (\hat{\mathcal{H}}_{d_1} + E_{e_0})|\psi_{d_1}(E_{e_0}, t)\rangle \; . \qquad (2.50) \end{aligned}$$

Again, the non-hermitian nuclear Hamiltonian of state x is denoted by $\hat{\mathcal{H}}_x$, which reads

$$\hat{\mathcal{H}}_x = \hat{H}_x - \frac{i}{2}\Gamma_x \; ,$$

where Γ_x denotes the *total* decay (or photoionization for state i) rate of state x. In the current case, the decay rates are [5]

$$\begin{aligned}\Gamma_{ph}(\omega,t) &= \frac{\sigma_i(\omega)I(t)}{\omega}\ ; &\qquad \Gamma_{d_1} &= 2\pi|\hat{W}_{d_1\to d_{2a}}|^2 + 2\pi|\hat{W}_{d_1\to d_{2b}}|^2\\ \Gamma_{d_{2a}} &= 2\pi|\hat{W}_{d_{2a}\to f}|^2\ ; &\qquad \Gamma_{d_{2b}} &= 2\pi|\hat{W}_{d_{2b}\to f}|^2\ .\end{aligned} \tag{2.51}$$

In matrix representation, for a specific channel one solves

$$i\begin{pmatrix}\dot{\psi}_i\\ \dot{\psi}_{d_1}\\ \dot{\psi}_{d_2}\\ \dot{\psi}_f\end{pmatrix}=\begin{pmatrix}\hat{\mathcal{H}}_i & 0 & 0 & 0\\ \hat{F}(t) & \hat{\mathcal{H}}_{d_1}+E_{e_0} & 0 & 0\\ 0 & \hat{W}_{d_1\to d_2} & \hat{\mathcal{H}}_{d_2}+E_{e_0}+E_{e_1} & 0\\ 0 & 0 & \hat{W}_{d_2\to f} & \hat{H}_f+E_{e_0}+E_{e_1}+E_{e_2}\end{pmatrix}\begin{pmatrix}\psi_i\\ \psi_{d_1}\\ \psi_{d_2}\\ \psi_f\end{pmatrix}, \tag{2.52}$$

where $\hat{\mathcal{H}}_{d_2}$, E_{e_1}, E_{e_2}, $\hat{W}_{d_1\to d_2}$, and $\hat{W}_{d_2\to f}$ depend on the channel.

In contrast, if the states d_{2a} and d_{2b} are degenerate, the EOMs[6] read

$$i\begin{pmatrix}\dot{\psi}_i\\ \dot{\psi}_{d_1}\\ \dot{\psi}_{d_{2a}}\\ \dot{\psi}_{d_{2b}}\\ \dot{\psi}_f\end{pmatrix}=\begin{pmatrix}\hat{\mathcal{H}}_i & 0 & 0 & 0 & 0\\ \hat{F}(t) & \hat{\mathcal{H}}_{d_1}+E_{e_0} & 0 & 0 & 0\\ 0 & \hat{W}_{d_1\to d_{2a}} & \hat{\mathcal{H}}_{d_{2a}}+E_{e_0}+E_{e_1} & -i\,\Lambda_{a,b}/2 & 0\\ 0 & \hat{W}_{d_1\to d_{2b}} & -i\,\Lambda_{b,a}/2 & \hat{\mathcal{H}}_{d_{2b}}+E_{e_0}+E_{e_1} & 0\\ 0 & 0 & \hat{W}_{d_{2a}\to f} & \hat{W}_{d_{2b}\to f} & \hat{H}_f+E_{e_0}+E_{e_1}+E_{e_2}\end{pmatrix}\begin{pmatrix}\psi_i\\ \psi_{d_1}\\ \psi_{d_{2a}}\\ \psi_{d_{2b}}\\ \psi_f\end{pmatrix}. \tag{2.53}$$

Compared with Eq. (2.52), Eq. (2.53) shows two additional interesting phenomena. First, the final state f is coherently populated by the wave packets coming from state d_{2a} and state d_{2b}. This coherent population on the final state f introduces an interference effect, which requires the precise knowledge of transition elements $\hat{W}_{d_1\to d_{2a}}$ and $\hat{W}_{d_1\to d_{2b}}$ for numerical simulations. Second, the emitted electrons are indistinguishable in energy. Hence the interchannel interference via continuum is possible, cf. the terms $\Lambda_{a,b}$ and $\Lambda_{b,a}$ in Eq. (2.53). These phenomena are interesting, but rarely discussed in the literature because of the difficulty to evaluate the transition matrix element [41]. To be specific, it is the phase of the transition matrix element which cannot be evaluated [41]. The impact of introducing the wrong phase to the dynamics is obvious. Consider an example where $\psi_{d_{2a}}$ and $\psi_{d_{2b}}$ are both Gaussian functions. If both transition elements are real and positive, the two Gaussian functions undergo constructive interference after their transition to state f. On the other hand, if both transition elements are real but with opposite signs, destructive interference is expected. Besides, the interchannel interference terms also depend on the phase of the transition element $\Lambda_{a,b} = 2\pi\hat{W}^{\dagger}_{d_1\to d_{2a}}\hat{W}_{d_1\to d_{2b}}$. In consequence, without the phase of the transition matrix elements, a correct simulation of the dynamics, including the interchannel interference

---

[5] $\sigma_i(\omega)$ denotes the ionization cross-section of state i under the photon energy ω, and $I(t)$ denotes the laser pulse intensity.

[6] See Sec. 2.2.

and coherent populating of f, is impossible. However, we can still estimate the impact of the interchannel interference on the dynamics by comparing a simulation without the interchannel interference to simulations with the interchannel interference based on some guessed phases. For example, we have investigated the ICD process in the CO$\cdots$Mg complex (with the interchannel interference using real positive numbers) together with Sören Kopelke, and the results have been published in his PhD thesis [41]. In this case, it was found that the interchannel interference exists only in a small range of CO bond length where the electronic states are degenerate, and hence the effect is negligible.

To conclude, for *separable* cascade channels, the EOMs can be written in the general form:

$$i\begin{pmatrix}\dot{\psi}_i\\ \dot{\psi}_{d_{1_\alpha}}\\ \dot{\psi}_{d_{2_\beta}}\\ \dot{\psi}_{f_\gamma}\end{pmatrix}=\begin{pmatrix}\hat{\mathcal{H}}_i & 0 & 0 & 0\\ \hat{F}_\alpha(t) & \hat{\mathcal{H}}_{d_{1_\alpha}}+E_{e_0} & 0 & 0\\ 0 & \hat{W}_{d_{1_\alpha}\to d_{2_\beta}} & \hat{\mathcal{H}}_{d_{2_\beta}}+E_{e_0}+E_{e_1} & 0\\ 0 & 0 & \hat{W}_{d_{2_\beta}\to f_\gamma} & \hat{H}_{f_\gamma}+E_{e_0}+E_{e_1}+E_{e_2}\end{pmatrix}\begin{pmatrix}\psi_i\\ \psi_{d_{1_\alpha}}\\ \psi_{d_{2_\beta}}\\ \psi_{f_\gamma}\end{pmatrix}, \tag{2.54}$$

where the Hamiltonians, energies of outgoing electrons, and transition matrix elements are given by the channel of interest. There is no interchannel interference via continuum in the EOMs. In this work, we follow Refs. [12, 42], where all the ICD channels are considered as separable, because the correct description for the interchannel interference (via continuum) is not available.

As a remark, we mention that the EOMs for the two-step decay process (with separable channels) initiated by photoexcitation, i.e. without e_0, are given in Appendix D.

2.4 Analysis

For a cascade electronic decay process one can measure the outgoing electrons separately or in coincidence. Measuring all electrons (e_0, e_1, e_2) in coincidence yields the multi-electron coincidence spectrum, which is by definition the probability of going into a channel that produces three outgoing electrons with certain energies. In consequence, one can define an operator $\hat{O}^{(\gamma)}$, yielding the desired probability when evaluated with the total wave function $|\Psi(t)\rangle$. This operator reads

$$\hat{O}^{(\gamma)} = |\Phi_{f_\gamma}, E_{e_0}, E_{e_1}, E_{e_2}\rangle\langle\Phi_{f_\gamma}, E_{e_0}, E_{e_1}, E_{e_2}| \,. \tag{2.55}$$

Consequently, the time-resolved multi-electron coincidence spectrum for a partial channel γ reads[7]

$$\sigma^{(\gamma)}(E_{e_0}, E_{e_1}, E_{e_2}, t) = \langle \Psi(t) | \hat{O}^{(\gamma)} | \Psi(t) \rangle = \langle \psi_{f_\gamma}(E_{e_0}, E_{e_1}, E_{e_2}, t) | \psi_{f_\gamma}(E_{e_0}, E_{e_1}, E_{e_2}, t) \rangle \ . \tag{2.56}$$

Eq. (2.56) is consistent with the common interpretation of the final state wave function $|\psi_{f_\gamma}(E_{e_0}, E_{e_1}, E_{e_2}, t)\rangle$, which is the amplitude of the system going into a certain final electronic state f_γ with the energies of outgoing electrons E_{e_0}, E_{e_1}, and E_{e_2}. Hence the final state population yields the time-resolved coincidence spectrum for a partial channel. The non-time-resolved (final) coincidence spectrum of the same partial channel γ is the result in the large-time limit, i.e.

$$\sigma^{(\gamma)}(E_{e_0}, E_{e_1}, E_{e_2}) = \lim_{t \to \infty} \langle \psi_{f_\gamma}(E_{e_0}, E_{e_1}, E_{e_2}, t) | \psi_{f_\gamma}(E_{e_0}, E_{e_1}, E_{e_2}, t) \rangle \ . \tag{2.57}$$

Here we introduce a systematic procedure to obtain a (time-resolved) partial spectrum through defining an operator which maps the total wave function to a probability of interest. This idea has been known in the literature [38, 43] for different cases, e.g. reaction probabilities. For a single electronic decay process, i.e. no cascade decay is present, our method yields exactly the same (time-resolved) electron spectrum as reported in Refs. [26, 44].

By integrating over E_{e_0} and E_{e_2}, the non-time-resolved spectrum of e_1 from the same partial channel reads

$$\sigma^{(\gamma)}_{e_1}(E_{e_1}) = \iint \mathrm{d}E_{e_0} \mathrm{d}E_{e_2} \sigma^{(\gamma)}(E_{e_0}, E_{e_1}, E_{e_2}) \ . \tag{2.58}$$

Similarly, the non-time-resolved spectrum of e_2 from the current partial channel reads

$$\sigma^{(\gamma)}_{e_2}(E_{e_2}) = \iint \mathrm{d}E_{e_0} \mathrm{d}E_{e_1} \sigma^{(\gamma)}(E_{e_0}, E_{e_1}, E_{e_2}) \ . \tag{2.59}$$

The above two equations for evaluating the spectra of e_1 and e_2 are identical to those reported in Ref. [33], where the (time-independent) scattering theory was employed. One of our main results is the formula for the time-resolved electron spectrum of e_1, which will be introduced together with the time-resolved electron spectrum of e_2 later in Ch. 4 and Ch. 5.

Due to the presence of many final states, i.e. many partial channels, Eqs. (2.56-2.59) describe the partial spectra of a partial channel from state d_{1_α} to state d_{2_β} and then to state f_γ. A total spectrum of state d_{2_β} to all possible f_γ hence requires a summation

---

[7] Use the ortho-normal conditions of the electronic states, cf. Eq. (2.21).

over all final states, i.e. the sum over γ:

$$\sigma^{(\beta)}(E_{e_0}, E_{e_1}, E_{e_2}) = \sum_{\gamma} \sigma^{(\gamma)}(E_{e_0}, E_{e_1}, E_{e_2}) \tag{2.60}$$

$$\sigma^{(\beta)}_{e_1}(E_{e_1}) = \sum_{\gamma} \sigma^{(\gamma)}_{e_1}(E_{e_1}) \tag{2.61}$$

$$\sigma^{(\beta)}_{e_2}(E_{e_2}) = \sum_{\gamma} \sigma^{(\gamma)}_{e_2}(E_{e_2}) \, . \tag{2.62}$$

If the total spectrum of state α is desired, an additional summation over β is required for Eqs. (2.60-2.62). For instance, $\sigma^{(\beta)}_{e_1}(E_{e_1})$ denotes the electron spectrum of e_1 from channel d_{1_α} to d_{2_β}. The total spectrum of e_1 from state d_{1_α} to all possible d_{2_β} hence requires an additional summation over β. For the separable channels, the rule to obtain a total spectrum of a specific state is a trivial summation over all possible channels[8]. Since we will discuss only the situation of separable channels, in later chapters we will use the formulation of the partial spectrum of a partial channel.

---

[8] Sometimes this is simplified as “summation over all final states.”

Chapter 3

ICD following the K-LL Auger process of Ne in NeAr (I)

The ICD process following the Auger decay of Ne^{+} $(1s^{-1})$ in the Ne dimer has been predicted theoretically in Refs. [45, 46] and confirmed experimentally in Ref. [11]. The process starts from photoionizing the $1s$ electron from one of the Ne atoms, where a very fast Auger decay (lifetime 2.4 fs) takes place. The Auger final state $\mathrm{Ne}^{2+}(2s^{-1}2p^{-1}\ {}^{1}P)\mathrm{Ne}$ then further undergoes a direct ICD process to the purely repulsive final state $\mathrm{Ne}^{2+}(2p^{-2}\ {}^{1}D) + \mathrm{Ne}^{+}(2p^{-1})$ via emitting an ICD electron. Demekhin *et al.* have carried out a theoretical study for this case [12], utilizing the fact that the Auger decay (lifetime 2.4 fs) is much faster than the relative nuclear motion between the two Ne atoms (period 350 fs). In other words, they took into account only the nuclear motion during the ICD process but did not consider the influence of the nuclear motion during the Auger process on the ICD electron spectrum, and their results agreed perfectly with the experimental observations [11].

In this chapter, we will apply the complex short iterative Lanczos integration scheme [33, 43] to solve the time-dependent Schrödinger equation for the NeAr dimer (for more details see Appendix E). By choosing a different neighboring atom (environment), i.e. Ar, we study the influence of changing the environment on the ICD channels. Since the ionization threshold of Ar $3p$ (15.82 eV) is lower than that of Ne $2p$ (21.60 eV), there will be more ICD channels available after the Ne^{+} $(1s^{-1})$ Auger decay process. A detailed description of the system is given in the following section.

channel	intermediate state	final state
1	$\mathrm{Ne}^{2+}(2s^{-1}2p^{-1}\ ^1P)\mathrm{Ar}$	$\mathrm{Ne}^{2+}(2p^{-2}\ ^1D)\text{-}\mathrm{Ar}^{+}(3p^{-1})$
2		$\mathrm{Ne}^{2+}(2p^{-2}\ ^1S)\text{-}\mathrm{Ar}^{+}(3p^{-1})$
3	$\mathrm{Ne}^{2+}(2s^{-1}2p^{-1}\ ^3P)\mathrm{Ar}$	$\mathrm{Ne}^{2+}(2p^{-2}\ ^3P)\text{-}\mathrm{Ar}^{+}(3p^{-1})$

Table 3.1: List of ICD channels in NeAr following the K-LL Auge decay in Ne. Detailed analysis of each channel is given in the text.

3.1 The NeAr system

Potential Curves

Our process of interest is the ICD following the Auger decay in Ne of NeAr. Potential energy curves, taken from Ref. [42], are depicted in Fig. 3.1. The potential energy curve of the electronic ground state[1] is depicted in panel (c) together with the initial wave packet, which is chosen to be the lowest vibrational eigenfunction of the NeAr ground state. After a Ne $1s$ electron is photoionized, the produced singly ionic state $\mathrm{Ne}^{+}(1\mathrm{s}^{-1})\mathrm{Ar}$ decays through an Auger process. Due to the presence of Ar, the doubly ionic Auger final states $\mathrm{Ne}^{2+}(2s^{-1}2p^{-1}\ ^1P)\mathrm{Ar}$ and $\mathrm{Ne}^{2+}(2s^{-1}2p^{-1}\ ^3P)\mathrm{Ar}$ both can relax further via an ICD process, resulting in a repulsive ionic pair of $\mathrm{Ne}^{2+}(2p^{-2})\text{-}\mathrm{Ar}^{+}(3p^{-1})$, which then undergoes Coulomb explosion. The potential energy curve of $\mathrm{Ne}^{+}(1s^{-1})\mathrm{Ar}$ and the potential energy curves the doubly and triply ionic states are depicted in Fig. 3.1 (a) and Fig. 3.1 (b), respectively.

As indicated in Fig. 3.1 by arrows, there are three ICD channels, which are numbered and listed in Table 3.1 with term symbols of states. Channel 1 and 2 are from the singlet state $\mathrm{Ne}^{2+}(2s^{-1}2p^{-1}\ ^1P)\mathrm{Ar}$, which is populated by the Auger process with a branching ratio of 17.5 % [47]. Channel 3 is from the triplet state $\mathrm{Ne}^{2+}(2s^{-1}2p^{-1}\ ^3P)\mathrm{Ar}$, whose Auger branching ratio is 6.5 % [47]. Within each channel, there are many partial channels because the states are degenerate. Take the ICD channel 1, i.e. $\mathrm{Ne}^{2+}(2s^{-1}2p^{-1}\ ^1P)\mathrm{Ar} \rightarrow \mathrm{Ne}^{2+}(2p^{-2}\ ^1D)\text{-}\mathrm{Ar}^{+}(3p^{-1})$, for instance. The intermediate state has three micro-states, namely a doubly degenerate[2] $^1\Pi$ and a $^1\Sigma^+$, while the final state has 15 micro-states[3], which are $^2\Delta_1$, $^2\Delta_2$, $^2\Pi_1$, $^2\Pi_2$, $^2\Pi_3$, $^2\Phi$, $^2\Sigma^-$, $^2\Sigma_1^+$, and $^2\Sigma_2^+$, see Fig. 3.1 for the potential curves. The situation is much simpler for channel 2, where there are only three ICD final micro-states, namely a doubly degenerate $^2\Pi$ and $^2\Sigma^+$. As for channel 3, there are 18 final micro-states: $^2\Delta$, $^2\Pi_1$, $^2\Pi_2$, $^2\Sigma^+$, $^2\Sigma_1^-$, $^2\Sigma_2^-$, $^4\Delta$, $^4\Pi_1$, $^4\Pi_2$, $^4\Sigma^+$, $^4\Sigma_1^-$, and $^4\Sigma_2^-$.

For each micro-state, we have performed the nuclear dynamics simulation to evaluate

---

[1] Its zero point energy (4.13 meV) is subtracted.

[2] Except for Σ, molecular term symbols are doubly degenerate.

[3] The spin degeneracy is not considered.

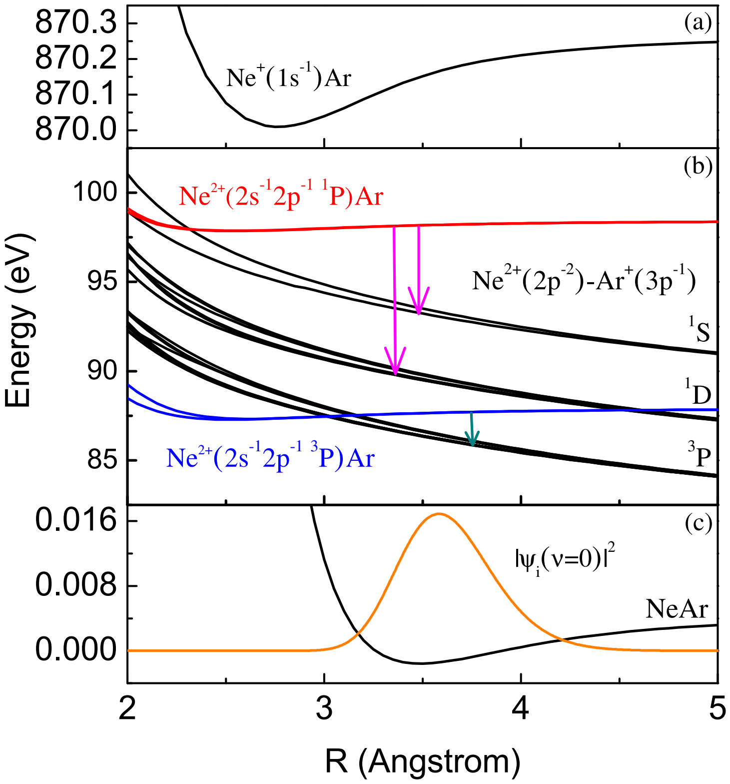

Figure 3.1: Potential energy curves for the ICD process following the Ne $1s^{-1}$ Auger decay in NeAr. Panel (c): shown are the potential curve of the NeAr electronic ground state and its lowest vibrational eigenfunction $|\chi_i(\nu=0)|^2$. Because of the very weak van der Waals force, the dimer has an equilibrium nuclear distance R of 3.5 Å. The potential curve of the first intermediate state, i.e. $\mathrm{Ne}^+(1s^{-1})\mathrm{Ar}$, is depicted in panel (a). The first intermediate state decays via electron emission (Auger process), producing $\mathrm{Ne}^{2+}\mathrm{Ar}$. Some of the doubly ionic states then can further decay by ICD, resulting in $\mathrm{Ne}^{2+}(2p^{-2})$-$\mathrm{Ar}^+(3p^{-1})$. Potential curves of the second intermediate states, i.e. $\mathrm{Ne}^{2+}(2s^{-1}2p^{-1})\mathrm{Ar}$, and the final states $\mathrm{Ne}^{2+}(2p^{-2})$-$\mathrm{Ar}^+(3p^{-1})$ are depicted in panel (b). Three possible ICD channels, see Table 3.1, are indicated by arrows.

the partial electron spectra. The ICD spectrum of a channel is then given by the sum over all partial spectra of available partial channels (see also Sec. 2.4).

ICD Transition Rates

The total transition rates of states $\mathrm{Ne}^{2+}(2s^{-1}2p^{-1}\,{}^1P)\mathrm{Ar}$ and $\mathrm{Ne}^{2+}(2s^{-1}2p^{-1}\,{}^3P)\mathrm{Ar}$, shown in Fig. 3.2, are taken from Ref. [48]. Because the ICD process involves the energy transfer between two atoms, the ICD transition rates naturally depend on the internuclear distance R ($\propto 1/R^6$ asymptotically [49]). For instance, the transition rates of the two micro-states ${}^1\Sigma^+$ and ${}^1\Pi$ of $\mathrm{Ne}^{2+}(2s^{-1}2p^{-1}\ {}^1P)\mathrm{Ar}$, depicted in Fig. 3.2(a), both increase while R decreases.

The ICD channel in the triplet $\mathrm{Ne}^{2+}(2s^{-1}2p^{-1}\ {}^3P)\mathrm{Ar}$ states, in contrast to those in the singlet states, closes at around $R = 3$ Å, as shown in Fig. 3.1(b). Accordingly, the total transition rates of these triplet states drop to zero at around $R = 3$ Å, see Fig. 3.2(b). Surprisingly, the total decay rates of these triplet states, shown in Fig. 3.2(b), rise again rapidly for $R < 2.5$ Å. The transition rates at this small internuclear distance are actually the transition rates form decay channels other than ICD. For example, the channel

$$\mathrm{Ne}^{2+}(2s^{-1}2p^{-1}\ {}^3P)\mathrm{Ar} \rightarrow \mathrm{Ne}^{+}(2p^{-1}) - \mathrm{Ar}^{2+}(3p^{-2}) + e^{-}_{\mathrm{ETMD}}\ .$$

is still open at the small internuclear distance. In this process, one outer-valence electron of the neighboring atom (Ar $3p$) fills in the inner-valence hole on the target atom ($\mathrm{Ne}^{2+}\ 2s^{-1}2p^{-1}$), and simultaneously one additional electron is ionized from the neighboring atom (Ar). Such a process has been termed *electron transfer mediated decay* (ETMD)[50, 51]. Since the ETMD requires the transfer of an electron, its role only becomes relevant when the orbital overlaps are sufficiently large, i.e. at short internuclear distance. In comparison to ICD, ETMD is much slower and negligible when the ICD channels are open. The only ETMD process which has been directly measured is $\mathrm{Ar}^{3+}\mathrm{Ar} \rightarrow \mathrm{Ar}^{2+}$-$\mathrm{Ar}^{2+}$ [51] where no ICD is available. Therefore, we will concentrate on the dynamics of ICD processes. For the current system, only the total decay rates are available [48], and each micro-state is assumed to have the same partial width.

The lifetimes of the singlet and triplet intermediate states can be estimated from their total widths at the equilibrium distance (3.5 Å). For example, the ${}^1\Pi$ state has a lifetime of around 36 fs, while the ${}^3\Pi$ lifetime is roughly 80 fs. On the other hand, the wave packet propagation shows that it takes roughly 250 fs for the wave packet to travel back and forth between the two turning points. See Fig. 3.2(c) for illustration. Hence one can expect that the nuclear dynamics will have a larger influence on the electron spectrum for the triplet channels than for the singlet channels.

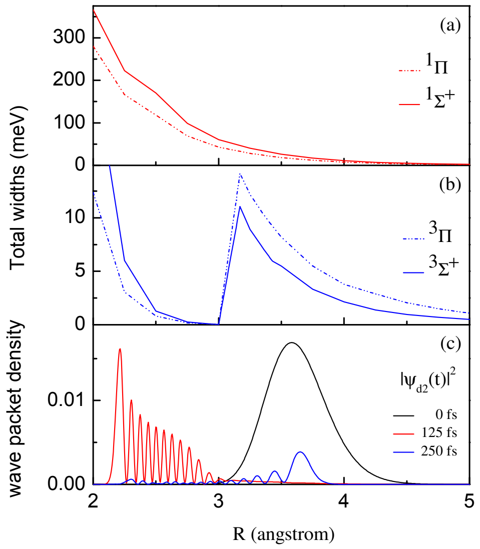

Figure 3.2: Total widths of the intermediate states and the wave packet density. Shown in panel (a) and (b) are the total widths, i.e. total decay rates, of the singlet and triplet states of $\mathrm{Ne}^{2+}(2s^{-1}2p^{-1})\mathrm{Ar}$, respectively. The data are taken from Ref. [48]. In panel (b), the ICD channels close completely at $R = 3$ Å and hence the widths decrease to zero. For $R < 2.5$ Å, the total widths increases again due to ETMD. Shown in panel (c) is the wave packet density of $|\psi_{d_2}\rangle$ for the triplet state after one half and one full period. The period of the wave packet motion is around 250 fs, and the norm of the wave packet after one period is roughly one-third of its original magnitude.

3.2 Theory

In this section we will describe how to obtain the working equations for numerical simulations of the nuclear dynamics in ICD processes under several widely used approximations. For the reader who is not interested in the details, a summary of the final working equations is provided at the end.

EOMs for ICD Following an Auger Process

The general theory of a two-step decay process has been introduced in Chapter 2 and can be adapted to the ICD following an Auger process. As already mentioned in the previous section, the first Auger decay process is simple: from an ionic state d_1 to different doubly ionic states d_{2_β}. Two of the doubly ionic states then continue to decay by ICD process to the triplet ionic final states, and all three ICD channels are distinguishable by their energies. For each channel, there are many partial channels due to the presence of micro-states d_{2_β} and f_γ. The partial channels are assumed to be also separable [12], even though the intermediate micro-states are almost degenerate. Following the procedure introduced in Sec. 2.3, the total wave function ansatz for the

ICD following an Auger decay process (see also Fig. 3.1) reads

$$\begin{aligned}|\Psi(t)\rangle = |\Phi_i\rangle|\psi_i(t)\rangle &+ \int \mathrm{d}E_{e_0}|\Phi_{d_1}, E_{e_0}\rangle|\psi_{d_1}(E_{e_0}, t)\rangle \\ &+ \sum_{\beta} \iint \mathrm{d}E_{e_0}\ \mathrm{d}E_{e_1}|\Phi_{d_{2_\beta}}, E_{e_0}, E_{e_1}\rangle|\psi_{d_{2_\beta}}(E_{e_0}, E_{e_1}, t)\rangle \\ &+ \sum_{\gamma} \iiint \mathrm{d}E_{e_0}\ \mathrm{d}E_{e_1}\ \mathrm{d}E_{e_1}|\Phi_{f_\gamma}, E_{e_0}, E_{e_1}, E_{e_2}\rangle|\psi_{f_\gamma}(E_{e_0}, E_{e_1}, E_{e_2}, t)\rangle. \end{aligned} \tag{3.1}$$

Following the same procedure as shown in Sec. 2.3, the EOMs read

$$i|\dot{\psi}_i(t)\rangle = \hat{\mathcal{H}}_i|\psi_i(t)\rangle \ , \tag{3.2}$$

$$i|\dot{\psi}_{d_1}(E_{e_0}, t)\rangle = \hat{F}(t)|\psi_i(t)\rangle + (\hat{\mathcal{H}}_{d_1} + E_{e_0})|\psi_{d_1}(E_{e_0}, t)\rangle \ , \tag{3.3}$$

$$\begin{aligned} i|\dot{\psi}_{d_{2_\beta}}(E_{e_0}, E_{e_1}, t)\rangle &= \hat{W}_{d_1\to d_{2_\beta}}|\psi_{d_1}(E_{e_0}, t)\rangle \\ &\quad + (\hat{\mathcal{H}}_{d_{2_\beta}} + E_{e_0} + E_{e_1})|\psi_{d_{2_\beta}}(E_{e_0}, E_{e_1}, t)\rangle \ , \end{aligned} \tag{3.4}$$

$$\begin{aligned} i|\dot{\psi}_{f_\gamma}(E_{e_0}, E_{e_1}, E_{e_2}, t)\rangle &= \hat{W}_{d_{2_\beta}\to f_\gamma}|\psi_{d_{2_\beta}}(E_{e_0}, E_{e_1}, t)\rangle \\ &\quad + (\hat{H}_{f_\gamma} + E_{e_0} + E_{e_1} + E_{e_2})|\psi_{f_\gamma}(E_{e_0}, E_{e_1}, E_{e_2}, t)\rangle \ . \end{aligned} \tag{3.5}$$

The nuclear Hamiltonians of state i, d_1, d_{2_β} read

$$\hat{\mathcal{H}}_i = \hat{H}_i - \frac{i}{2}\frac{\sigma_i(\omega)I(t)}{\omega} \quad ; \quad \hat{\mathcal{H}}_{d_1} = \hat{H}_{d_1} - \frac{i}{2}\Gamma_{d_1} \quad ; \quad \hat{\mathcal{H}}_{d_{2_\beta}} = \hat{H}_{d_{2_\beta}} - \frac{i}{2}\Gamma_{d_{2_\beta}} \ , \tag{3.6}$$

where $\sigma_i(\omega)$ is the ionization cross-section of the state i to state d_1 under the incident photon energy ω, $I(t)$ is the cyclic-averaged laser pulse intensity; Γ_{d_1} and $\Gamma_{d_{2_\beta}}$ are the total decay widths of state d_1 and state d_{2_β}, respectively. These total decay widths are related to individual transition matrix elements:

$$\Gamma_{d_1} = \sum_{\beta'} 2\pi|\hat{W}_{d_1\to d_{2_{\beta'}}}|^2 \quad ; \quad \Gamma_{d_{2_\beta}} = \sum_{\gamma'} 2\pi|\hat{W}_{d_{2_\beta}\to f_{\gamma'}}|^2 \ ,$$

under the local approximation. Additionally, the initial wave function $|\psi_i(0)\rangle$ is chosen to be the lowest vibrational eigenfunction of state i. The ICD electron spectrum for each individual partial channel is given by Eq. (2.59), while the total ICD electron spectrum for a channel is the summation over the results of all partial channels, cf. Eq. (2.62).

Approximations and Corresponding Initial Conditions

The time-dependent Schrödinger equation for the nuclear dynamics is an initial value problem. Once the initial wave packet is determined, the rest follows by integration over time[4], according to the EOMs. Although the initial wave packet is chosen to be the lowest vibrational eigenfunction of state i, in practice it is usually directly placed on the intermediate state [9, 10, 26] or even the second intermediate state [12] under some approximations. We shall explain how to determine the initial condition according to the used approximations in practice.

First, the experiments are usually performed in the gas phase at a very low temperature. Hence it is usually assumed that only the lowest vibrational level is populated. If the temperature is higher, for each calculation one uses a different vibrational eigenfunction as the initial wave packet, and the simulated results are averaged according to the Boltzmann distribution.

Second, if the used light source is not too strong, which is the case e.g. for synchrotron radiation, the laser pulse intensity is within the perturbative regime. Namely, only a few percents of molecules are ionized (or excited) during the laser pulse duration. Therefore, the depletion of the initial state i can be neglected, and its EOM reads

$$i|\dot{\psi}_i(t)\rangle = \hat{H}_i|\psi_i(t)\rangle \ . \tag{3.7}$$

This is called the *weak field approximation* [26] because the field is so weak that the electronic ground state i is essentially unperturbed[5]. Under this approximation, $|\psi_i(t)\rangle$ is trivial and can be ignored from the simulation.

Third, according to Eq. (3.3), the intermediate state gets populated by $\hat{F}(t)|\psi_i(t)\rangle$. The term $\hat{F}(t)$ is often written in the following form [9, 12, 33]:

$$\hat{F}(t) = \hat{V}_{i\to d_1} g(t) \ ,$$

where $g(t)$ and $\hat{V}_{i\to d_1}$ denote the envelope of the electric field and the amplitude of the ionization process, respectively. If the laser pulse is much longer than the lifetime of state d_1, and for the ionization process the incident photon energy is around the ionization threshold of state d_1, the state d_1 is continuously populated by $\hat{V}_{i\to d_1} g(t)|\psi_i(t)\rangle$. This has been termed *narrow-band excitation / ionization* [26]. If the pulse is short, e.g. $\sim \delta(t)$, and for the ionization process the incident photon energy is well-above the ionization threshold, the transition is equivalent to directly placing the wave packet $\hat{V}_{i\to d_1}|\chi_i(\nu = 0)\rangle$ on state d_1 at $t = 0$. Namely, Eq. 3.3 becomes

$$i|\dot{\psi}_{d_1}(E_{e_0}, t)\rangle = (\hat{\mathcal{H}}_{d_1} + E_{e_0})|\psi_{d_1}(E_{e_0}, t)\rangle \ ,$$

with the initial wave packet

$$|\psi_{d_1}(E_{e_0}, 0)\rangle = \hat{V}_{i\to d_1}|\chi_i(\nu = 0)\rangle \tag{3.8}$$

---

[4] It is often called “propagation.”

[5] In consequence, the transition to state d_1 and the following process can be treated by the perturbation theory.

This approximation has been termed *broad-band excitation / ionization* [26]. If $\hat{V}_{i\to d_1}$ is independent of R, this gives the well-known Condon approximation, resulting in a vertical transition. The most common choice of $\hat{V}_{i\to d_1}$ under the Condon approximation is $\hat{V}_{i\to d_1} = 1$ [9, 12, 26, 33]. However, when doing so, one changes the absolute intensity of the spectrum. In the following, we will discuss how the absolute intensity of the spectrum, starting from assuming that $\hat{V}_{i\to d_1}$ is in fact a function of E_{e_0}. In practice, $\hat{V}_{i\to d_1}$ will be chosen as 1 for calculation, yielding a spectrum with the relative intensity. To obtain the spectrum with the absolute intensity, see the following discussion.

For our simulation, we follow the weak field approximation and the broad-band ionization, so that $|\psi_{d_1}(E_{e_0}, 0)\rangle = \hat{V}_{i\to d_1}|\chi_i(\nu = 0)\rangle$. In addition, we follow the fast Auger decay approximation [12], which assumes that the system decays to the second intermediate state d_{2_β} before the wave packet could move on state d_1. Namely, the initial condition now reads

$$|\psi_{d_{2_\beta}}(E_{e_0}, E_{e_1}, 0)\rangle = \hat{V}_{d_1\to d_{2_\beta}}(E_{e_1})\hat{V}_{i\to d_1}(E_{e_0})|\chi_i(\nu = 0)\rangle \ , \tag{3.9}$$

where $\hat{V}_{d_1\to d_{2_\beta}}$ is usually considered as R-independent for an Auger process. Under the broad-band and fast Auger decay approximations, the effective EOMs become

$$\begin{aligned} i|\dot{\psi}_{d_{2_\beta}}(E_{e_0}, E_{e_1}, t)\rangle &= (\hat{\mathcal{H}}_{d_{2_\beta}} + E_{e_0} + E_{e_1})|\psi_{d_{2_\beta}}(E_{e_0}, E_{e_1}, t)\rangle \ , & (3.10)\\ i|\dot{\psi}_{f_\gamma}(E_{e_0}, E_{e_1}, E_{e_2}, t)\rangle &= \hat{W}_{d_{2_\beta}\to f_\gamma}|\psi_{d_{2_\beta}}(E_{e_0}, E_{e_1}, t)\rangle \\ &\quad + (\hat{H}_{f_\gamma} + E_{e_0} + E_{e_1} + E_{e_2})|\psi_{f_\gamma}(E_{e_0}, E_{e_1}, E_{e_2}, t)\rangle \ . & (3.11) \end{aligned}$$

Observing Eq. (3.10) and Eq. (3.11), one finds that $E_{e_0} + E_{e_1}$ only contributes a trivial phase to the wave packets. This trivial phase can be removed by dressing up the states with a counter phase. Namely,

$$\begin{aligned} |\tilde{\psi}_{d_{2_\beta}}(E_{e_0}, E_{e_1}, t)\rangle &= e^{i(E_{e_0}+E_{e_1})t}|\psi_{d_{2_\beta}}(E_{e_0}, E_{e_1}, t)\rangle & (3.12)\\ |\tilde{\psi}_{f_\gamma}(E_{e_0}, E_{e_1}, E_{e_2}, t)\rangle &= e^{i(E_{e_0}+E_{e_1})t}|\psi_{f_\gamma}(E_{e_0}, E_{e_1}, E_{e_2}, t)\rangle \ . \end{aligned}$$

where $|\tilde{\psi}_{d_2}(E_{e_0}, E_{e_1}, t)\rangle$ and $|\tilde{\psi}_f(E_{e_0}, E_{e_1}, E_{e_2}, t)\rangle$ are the *dressed* wave functions[6], while $|\psi_{d_2}(E_{e_0}, E_{e_1}, t)\rangle$ and $|\psi_f(E_{e_0}, E_{e_1}, E_{e_2}, t)\rangle$ are the *bare* wave functions. Replacing the bare wave functions in Eqs. (3.10-3.11) by the dressed ones, the EOMs read

$$\begin{aligned} i|\dot{\tilde{\psi}}_{d_{2_\beta}}(E_{e_0}, E_{e_1}, t)\rangle &= \hat{\mathcal{H}}_{d_{2_\beta}}|\tilde{\psi}_{d_{2_\beta}}(E_{e_0}, E_{e_1}, t)\rangle & (3.13)\\ i|\dot{\tilde{\psi}}_{f_\gamma}(E_{e_0}, E_{e_1}, E_{e_2}, t)\rangle &= \hat{W}_{d_{2_\beta}\to f_\gamma}|\tilde{\psi}_{d_{2_\beta}}(E_{e_0}, E_{e_1}, t)\rangle \\ &\quad + (\hat{H}_{f_\gamma} + E_{e_2})|\tilde{\psi}_{f_\gamma}(E_{e_0}, E_{e_1}, E_{e_2}, t)\rangle \ . & (3.14) \end{aligned}$$

Although Eq. (3.13) and Eq. (3.14) do not depend on E_{e_0} nor on E_{e_1}, the initial wave packet does depend on these two energies, see Eq. (3.9). Consequently the formal

---

[6] This technique is called the *dressed state method*.

solution for $|\tilde{\psi}_{f_\gamma}(E_{e0}, E_{e_1}, E_{e_2}, t)\rangle$ also depends on these two energies, i.e.

$$\begin{aligned}
&|\tilde{\psi}_{f_\gamma}(E_{e0}, E_{e_1}, E_{e_2}, t)\rangle \\
&= -i \int_0^t \mathrm{d}t' e^{i(\hat{H}_{f_\gamma}+E_{e_2})(t'-t)} \hat{W}_{d_{2_\beta}\to f_\gamma} e^{-i\hat{H}_{d_{2_\beta}}t'} |\tilde{\psi}_{d_{2_\beta}}(E_{e0}, E_{e_1}, E_{e_2}, 0)\rangle \\
&\approx -i\hat{V}_{d_1\to d_{2_\beta}}(E_{e_1})\hat{V}_{i\to d_1}(E_{e0}) \int_0^t \mathrm{d}t' e^{i(\hat{H}_{f_\gamma}+E_{e_2})(t'-t)} \hat{W}_{d_{2_\beta}\to f_\gamma} e^{-i\hat{H}_{d_{2_\beta}}t'} |\chi_i(\nu=0)\rangle \;. \qquad (3.15)
\end{aligned}$$

The Condon approximation, that is $\hat{V}_{i\to d_1}(E_{e0})$ and $\hat{V}_{d_1\to d_{2_\beta}}(E_{e_1})$ are taken as R-independent, has been applied in Eq. (3.15), which then shows that the propagation can be done with an initial wave packet $|\chi_i(\nu = 0)\rangle$, and the coefficients $\hat{V}_{d_1\to d_{2_\beta}}(E_{e_1})\hat{V}_{i\to d_1}(E_{e0})$ are multiplied to the wave packets afterwards. Hence in practice the initial wave packet for propagation is often chosen to be $|\chi_i(\nu = 0)\rangle$ [9, 10, 12, 26, 42]. To distinguish the propagation done with the initial wave packet $|\chi_i(\nu = 0)\rangle$ from the others, we now define $|\psi_{d_{2_\beta}}(t)\rangle$ and $|\psi_{f_\gamma}(E_{e_2}, t)\rangle$, which do not depend on E_{e_0} nor on E_{e_1}. The EOMs for them read

$$i|\dot{\psi}_{d_{2_\beta}}(t)\rangle = \hat{\mathcal{H}}_{d_{2_\beta}}|\psi_{d_{2_\beta}}(t)\rangle \qquad (3.16)$$

$$i|\dot{\psi}_{f_\gamma}(E_{e_2}, t)\rangle = \hat{W}_{d_{2_\beta}\to f_\gamma}|\psi_{d_{2_\beta}}(t)\rangle + (\hat{H}_{f_\gamma} + E_{e_2})|\psi_{f_\gamma}(E_{e_2}, t)\rangle \;. \qquad (3.17)$$

Eqs. (3.16-3.17) are formally equivalent to Eqs. (3.13-3.14). The only difference is that the dressed wave packets in Eqs. (3.16-3.17) do not depend on E_{e_0} nor on E_{e_1} due to the choice of the initial wave packet.

Spectrum Intensity and Norm Conservation

According to Eq. (2.59), the partial ICD electron spectrum of a partial channel f_γ reads

$$\begin{aligned}
&\sigma_{e_2}^{(\gamma)}(E_{e_2}) \\
&= \lim_{t\to\infty} \iint \mathrm{d}E_{e0}\mathrm{d}E_{e_1} \langle\psi_{f_\gamma}(E_{e0}, E_{e_1}, E_{e_2}, t)|\psi_{f_\gamma}(E_{e0}, E_{e_1}, E_{e_2}, t)\rangle \\
&= \lim_{t\to\infty} \iint \mathrm{d}E_{e0}\mathrm{d}E_{e_1} \langle\tilde{\psi}_{f_\gamma}(E_{e0}, E_{e_1}, E_{e_2}, t)|\tilde{\psi}_{f_\gamma}(E_{e0}, E_{e_1}, E_{e_2}, t)\rangle \\
&= \lim_{t\to\infty} \int \mathrm{d}E_{e0}|\hat{V}_{i\to d_1}(E_{e0})|^2 \int \mathrm{d}E_{e_1}|\hat{V}_{d_1\to d_{2_\beta}}(E_{e_1})|^2 \langle\psi_{f_\gamma}(E_{e_2}, t)|\psi_{f_\gamma}(E_{e_2}, t)\rangle \;. \qquad (3.18)
\end{aligned}$$

Since $\hat{V}_{i\to d_1}$ and $\hat{V}_{d_{2_\beta}\to f_\gamma}$ do not depend on E_{e_2}, the *shape* of the spectrum $\sigma_{e_2}^{(\gamma)}$ is only determined by the population of the dressed final state. Namely, the ICD electron spectrum with a relative intensity for the given channel f_γ is given by [12]

$$\sigma_{e_2}^{(\gamma)}(E_{e_2}) = \lim_{t\to\infty} \langle\psi_{f_\gamma}(E_{e_2}, t)|\psi_{f_\gamma}(E_{e_2}, t)\rangle \;. \qquad (3.19)$$

If the absolute intensity is relevant, the integrations in Eq. (3.18) have to be evaluated. Here we demonstrate how to evaluate these integrations for a broad-band ionization process. For simplicity, the envelope $g(t)$ is chosen as a delta-like pulse such that $g^2(t) = \delta(t)$, and the theory for an arbitrary $g(t)$ can be easily deduced by following the same procedure. The key of obtaining the absolute intensity is the norm conservation of the total wave function. Namely,

$$\langle \Psi(t) | \Psi(t) \rangle = 1 \ .$$

With Eq. (3.1), the norm conservation yields

$$\begin{aligned} 1 - \langle \psi_i(t) | \psi_i(t) \rangle = & \int \mathrm{d}E_{e_0} \langle \psi_{d_1}(E_{e_0}, t) | \psi_{d_1}(E_{e_0}, t) \rangle \\ & + \sum_{\beta} \iint \mathrm{d}E_{e_0} \, \mathrm{d}E_{e_1} \langle \psi_{d_{2_\beta}}(E_{e_0}, E_{e_1}, t) | \psi_{d_{2_\beta}}(E_{e_0}, E_{e_1}, t) \rangle \\ & + \sum_{\gamma} \iiint \mathrm{d}E_{e_0} \, \mathrm{d}E_{e_1} \, \mathrm{d}E_{e_2} \langle \psi_{f_\gamma}(E_{e_0}, E_{e_1}, E_{e_2}, t) | \psi_{f_\gamma}(E_{e_0}, E_{e_1}, E_{e_2}, t) \rangle \ . \end{aligned} \tag{3.20}$$

Eq. (3.20) holds for all t, and of course, it holds for $t = 0$ when the initial condition is determined. If no assumption is made, the original initial wave packet is chosen as $|\psi_i(0)\rangle = |\chi_i(\nu = 0)\rangle$ and wave packets of other states are zero. For this case, Eq. (3.20) at $t = 0$ becomes

$$1 - \langle \chi_i(\nu = 0) | \chi_i(\nu = 0) \rangle = 0 \ , \tag{3.21}$$

which simply states the normalization of the vibrational eigenfunction. If the broad-band ionization is assumed, the initial condition directly after the pulse (this moment of time is denoted by $t = 0^+$) is then given by the wave packet populated on state d_1 after the pulse but before the decay processes take place. For this situation, Eq. (3.20) becomes

$$1 - \langle \psi_i(0^+) | \psi_i(0^+) \rangle = \int \mathrm{d}E_{e_0} \langle \psi_{d_1}(E_{e_0}, 0^+) | \psi_{d_1}(E_{e_0}, 0^+) \rangle \ . \tag{3.22}$$

The right hand side (RHS) of Eq. (3.22) can be carried out by using Eq. (3.8) and the Condon approximation, yielding

$$\int \mathrm{d}E_{e_0} \langle \psi_{d_1}(E_{e_0}, 0^+) | \psi_{d_1}(E_{e_0}, 0^+) \rangle = \int \mathrm{d}E_{e_0} |\hat{V}_{i \to d_1}(E_{e_0})|^2 \ .$$

On the other hand, the left-hand-side (LHS) of Eq. (3.22) states the loss of the population of state i due to the photoionization. With Eq. (3.2) and Eq. (3.6), the LHS can be evaluated by[7]

$$1 - \langle \psi_i(0^+) | \psi_i(0^+) \rangle = -\int_{0^-}^{0^+} \mathrm{d}t \frac{\mathrm{d}}{\mathrm{d}t} \langle \psi_i(t) | \psi_i(t) \rangle = \int_{0^-}^{0^+} \mathrm{d}t \langle \psi_i(t) | \frac{\sigma_i(\omega) \varepsilon_0^2 \delta(t)}{8\pi\alpha\omega} | \psi_i(t) \rangle = \frac{\sigma_i(\omega)}{\omega} \frac{\varepsilon_0^2}{8\pi\alpha},$$

---

[7]
$$I(t) = \frac{\varepsilon_0^2 g^2(t)}{8\pi\alpha} \approx \frac{\varepsilon_0^2 \delta(t)}{8\pi\alpha} \ ,$$
where ε_0 is the electric field amplitude, and α is the fine structure constant. See Ref. [52].

where the first fraction is related to the photoionization cross-section, and the second fraction is the intensity of the laser pulse. In consequence, the absolute intensity for populating state d_1 with all possible photoelectron energies reads

$$\int \mathrm{d}E_{e_0} |\hat{V}_{i\to d_1}(E_{e_0})|^2 = \frac{\sigma_i(\omega)}{\omega} \frac{\varepsilon_0^2}{8\pi\alpha} \ . \tag{3.23}$$

At last, if the fast-Auger decay assumption is additionally made, then the initial condition is given by the wave packet directly populated onto state d_{2_β} after both the pulse and the ultra-fast Auger decay ($t = 0^+$), but before the ICD takes place. Eq. (3.20) now becomes

$$1 - \langle \psi_i(0^+)|\psi_i(0^+)\rangle = \sum_\beta \iint \mathrm{d}E_{e_0}\mathrm{d}E_{e_1} \langle \psi_{d_{2_\beta}}(E_{e_0}, E_{e_1}, 0^+)|\psi_{d_{2_\beta}}(E_{e_0}, E_{e_1}, 0^+)\rangle \ . \tag{3.24}$$

The LHS of Eq. (3.24) is already known from the previous reasoning. The RHS of the equation is also not difficult to carry out by using Eq. (3.9) and the Condon approximation, resulting in

$$\begin{aligned}
&\sum_\beta \iint \mathrm{d}E_{e_0}\mathrm{d}E_{e_1} \langle \psi_{d_{2_\beta}}(E_{e_0}, E_{e_1}, 0^+)|\psi_{d_{2_\beta}}(E_{e_0}, E_{e_1}, 0^+)\rangle \\
=&\int \mathrm{d}E_{e_0}|\hat{V}_{i\to d_1}(E_{e_0})|^2 \sum_\beta \int \mathrm{d}E_{e_1}|\hat{V}_{d_1\to d_{2_\beta}}(E_{e_1})|^2 = \frac{\sigma_i(\omega)}{\omega}\frac{\varepsilon_0^2}{8\pi\alpha} \sum_\beta \int \mathrm{d}E_{e_1}|\hat{V}_{d_1\to d_{2_\beta}}(E_{e_1})|^2 .
\end{aligned}$$

Using the above representation for RHS, Eq. (3.24) yields

$$\sum_\beta \int \mathrm{d}E_{e_1}|\hat{V}_{d_1\to d_{2_\beta}}(E_{e_1})|^2 = 1 \ . \tag{3.25}$$

In Eq. (3.25), the integration $\int \mathrm{d}E_{e_1}|\hat{V}_{d_1\to d_{2_\beta}}(E_{e_1})|^2$ denotes the probability of the wave packet going into states d_{2_β} from state d_1. Since the wave packet of state d_1 should completely decay into states d_{2_β}, this value should be 1. Following Eq. (3.25), the probability for going into a specific state d_{2_β}, namely the *branching ratio*[8], is given by:

$$\int \mathrm{d}E_{e_1}|\hat{V}_{d_1\to d_{2_\beta}}(E_{e_1})|^2 = \frac{2\pi|\hat{W}_{d_1\to d_{2_\beta}}|^2}{\sum_{\beta'} 2\pi|\hat{W}_{d_1\to d_{2_{\beta'}}}|^2} = \frac{\Gamma_\beta}{\sum_{\beta'}\Gamma_{\beta'}} = \frac{\Gamma_\beta}{\Gamma_{d_1}} \ , \tag{3.26}$$

where $\Gamma_\beta/\Gamma_{d_1}$ is the branching ratio of the decay from state d_1 to state d_{2_β}.

Now, we come back to Eq. (3.18). The absolute intensity of the ICD electron spectrum for a single partial channel, i.e. the partial spectrum, reads

$$\begin{aligned}
&\sigma_{e_2}^{(\gamma)}(E_{e_2}) \\
&= \lim_{t\to\infty} \int \mathrm{d}E_{e_0}|\hat{V}_{i\to d_1}(E_{e_0})|^2 \int \mathrm{d}E_{e_1}|\hat{V}_{d_1\to d_{2_\beta}}(E_{e_1})|^2 \langle \psi_{f_\gamma}(E_{e_2}, t)|\psi_{f_\gamma}(E_{e_2}, t)\rangle \\
&= \frac{\sigma_i(\omega)}{\omega}\frac{\varepsilon_0^2}{8\pi\alpha} \times \frac{\Gamma_\beta}{\Gamma_{d_1}} \times \lim_{t\to\infty} \langle \psi_{f_\gamma}(E_{e_2}, t)|\psi_{f_\gamma}(E_{e_2}, t)\rangle \ .
\end{aligned} \tag{3.27}$$

---

[8] The ratio of the partial decay width to the overall decay width

Due to recent developments in pump-probe techniques using femtosecond and subfemtosecond pulses [53, 54], measuring the time-resolved electron spectrum is within reach [55]. Hence we mentioned that the time-resolved electron spectrum for a single partial channel, i.e. the time-resolved partial spectrum, with absolute intensity reads

$$\sigma_{e_2}^{(\gamma)}(E_{e_2}, t) = \frac{\sigma_i(\omega)}{\omega} \frac{\varepsilon_0^2}{8\pi\alpha} \times \frac{\Gamma_\beta}{\Gamma_{d_1}} \times \langle \psi_{f_\gamma}(E_{e_2}, t) | \psi_{f_\gamma}(E_{e_2}, t) \rangle \; . \tag{3.28}$$

Eqs. (3.27-3.28) show that the Auger branching ratio is relevant when the (time-resolved) ICD spectra from different Auger channels are compared.

Summary

To sum up, we have employed the broad-band ionization, the weak field approximation and the fast-Auger decay approximation. These two approximations allow us to simplify a two-step (Auger decay followed by ICD) process into a single-step (ICD) process. The working equations for this read [12]

$$i|\dot{\psi}_{d2_\beta}(t)\rangle = \hat{\mathcal{H}}_{d2_\beta} |\psi_{d2_\beta}(t)\rangle \tag{3.29}$$

$$i|\dot{\psi}_{f_\gamma}(E_{e_2}, t)\rangle = \hat{W}_{d2_\beta \to f_\gamma} |\psi_{d2_\beta}(t)\rangle + (\hat{H}_{f_\gamma} + E_{e_2}) |\psi_{f_\gamma}(E_{e_2}, t)\rangle \; , \tag{3.30}$$

with the initial wave packet $|\psi_{d2_\beta}(0)\rangle = |\chi_i(\nu = 0)\rangle$.

If the absolute intensity is not relevant, the time-resolved partial spectrum (with a relative intensity) can be evaluated according to [12]

$$\sigma_{e_2}^{(\gamma)}(E_{e_2}, t) = \langle \psi_{f_\gamma}(E_{e_2}, t) | \psi_{f_\gamma}(E_{e_2}, t) \rangle \; , \tag{3.31}$$

while the non-time-resolved partial spectrum (with a relative intensity) reads [12]

$$\sigma_{e_2}^{(\gamma)}(E_{e_2}) = \lim_{t \to \infty} \langle \psi_{f_\gamma}(E_{e_2}, t) | \psi_{f_\gamma}(E_{e_2}, t) \rangle \; . \tag{3.32}$$

In order to compare with experiment, we sum over all the partial spectra of possible final states for a channel. In addition, the ICD spectra from two different Auger channels, e.g. ICD channel 1 and ICD channel 3, will be compared. Therefore, the calculated spectrum must additionally be multiplied with the Auger branching ratios, as shown in Eqs. (3.27-3.28).

3.3 Numerical ICD Electron Spectra

In this section we present the numerical results for the ICD electron spectrum, obtained by carrying out the wave packet propagation according to Eqs. (3.29-3.30). The ICD electron spectrum then is evaluated via Eqs. (3.31-3.32) and afterwards is multiplied with the Auger branching ratio.

Let us begin with channel 1 (see Table 3.1). The time-resolved ICD electron spectrum of one particular partial channel

$$\mathrm{Ne}^{2+}(2s^{-1}2p^{-1}\,{}^1P)\mathrm{Ar}\ [{}^1\Pi] \rightarrow \mathrm{Ne}^{2+}(2p^{-2}\,{}^1D) - \mathrm{Ar}^{+}\ [{}^2\Delta_1] + e^{-}_{\mathrm{ICD}}\ ,$$

is depicted in Fig. 3.3(a). Within the first 40 fs, the ICD electron energy distribution is basically Gaussian, centered at an energy of 8.7 eV. After 40 fs, a small tail develops toward a lower electron kinetic energy, stemming from that the wave packet $|\psi_{d_{2_\beta}}(t)\rangle$ moves to a smaller internuclear distance R, from where the emitted ICD electron has a lower kinetic energy. The time-resolved electron spectrum is converged after 200 fs (black curve), yielding the non time-resolved partial electron spectrum. For comparison, an estimated electron spectrum can be obtained without considering the nuclear motion by employing the so-called "mirror-reflection" principle[9] [23, 56], the result of which is depicted by the orange-dotted curve in Fig. 3.3 (a). The difference between the black and orange-dotted curves is small, showing that the nuclear dynamics is not very important in this channel, as we already expected.

Shown in panel (a) is only the time-resolved spectrum of a single partial channel. There are 9 partial channels (6 of the micro-states are doubly degenerate) for the process

$$\mathrm{Ne}^{2+}(2s^{-1}2p^{-1}\,{}^1P)\mathrm{Ar}\ [{}^1\Pi] \rightarrow \mathrm{Ne}^{2+}(2p^{-2}\,{}^1D) - \mathrm{Ar}^{+} + e^{-}_{\mathrm{ICD}}\ .$$

All the partial ICD electron spectra of this process are depicted in Fig. 3.3(b). Naturally, the spectra for the doubly degenerate states are twice as intense as the non-degenerate ones, cf. ${}^2\Delta_1$ and ${}^2\Sigma^-$ shown in Fig. 3.3(b) because an equal partial decay rate for each micro-state is assumed. In addition, the spectra are centered at slightly different ICD electron energies due to the fact that the potential curves of $\mathrm{Ne}^{2+}(2p^{-2}\,{}^1D)$-$\mathrm{Ar}^{+}$ separate into two groups, see Fig. 3.1.

The spectra shown in both Fig. 3.3(a) and (b) are already multiplied by the Auger branching ratio (17.5%) to the singlet $\mathrm{Ne}^{2+}(2s^{-1}2p^{-1}\,{}^1P)\mathrm{Ar}$ state. However, it is a naïve multiplication and does not take into account that this branching ratio has to be redistributed to micro-states of $\mathrm{Ne}^{2+}(2s^{-1}2p^{-1}\,{}^1P)\mathrm{Ar}$, namely ${}^1\Pi$ (doubly degenerate) and ${}^1\Sigma$. In consequence, the ${}^1\Pi$ state actually has a branching ratio of 17.5% × 2/3 by the statistics of micro-states. Hence, summing up all the partial spectra shown in panel (b) and multiplying the result by 2/3 gives the ICD electron spectrum from the micro-state ${}^1\Pi$, which is depicted by the blue-dashed line in Fig. 3.3(c). Similarly, the red-dotted line depicts the corresponding spectrum from the ${}^1\Sigma$ state. The total

---

[9] The mirror-reflection principle assumes that there is no nuclear dynamics during electron emission, so that the electron spectrum is given by mapping the probability distribution $|\chi_i(R)|^2$ onto the potential gap $V_{d_2}(R) - V_f(R)$ through R. If the decay rate Γ is R-dependent, then one maps $\Gamma_{d_2}(R)|\chi_i(R)|^2$ onto the potential gaps.

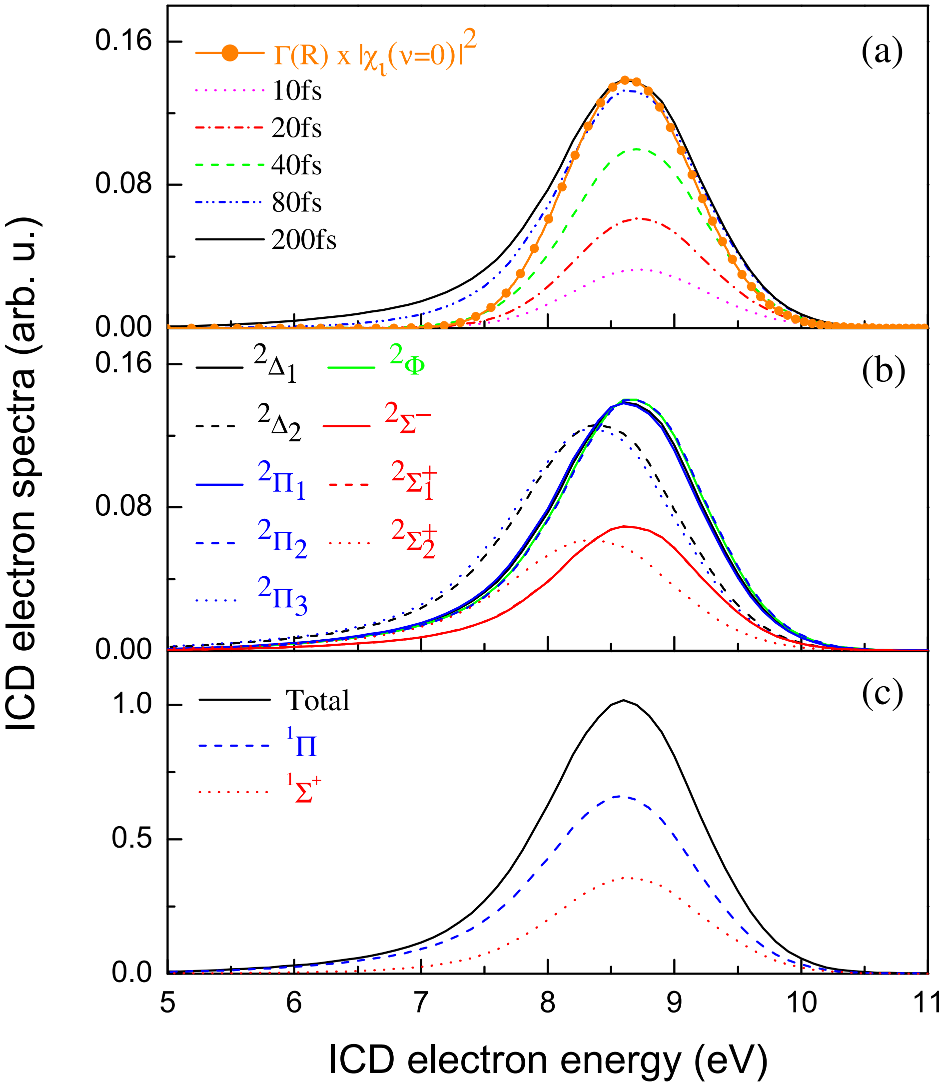

Figure 3.3: ICD electron spectra of channel 1 (see Table 3.1). Panel (a) shows the time-resolved ICD electron spectrum of one partial channel (see the text). The spectrum develops over time, and the slightly asymmetric tail is the evidence that $|\psi_{d_{2_\beta}}(t)\rangle$ moves toward smaller R during the decay process. The curve obtained via $\Gamma_{d_2}(R)|\chi_i(R)|^2$ is the estimation of the spectrum based on the mirror-reflection principle (see text). Shown in panel (b) are the spectra of all ICD partial channels from $\mathrm{Ne}^{2+}(2s^{-1}2p^{-1}\ {}^1P)\mathrm{Ar}[{}^1\Pi]$. Note that a degenerate final state, e.g. ${}^2\Delta_1$, is as twice intense as a non-degenerate final state, e.g. ${}^2\Sigma^-$. The total ICD spectrum, shown by the black curve in panel (c), is obtained via summing over all partial spectra and averaging with the statistic weights of the intermediate states, i.e. ${}^1\Pi$ and ${}^1\Sigma$, whose contributions are also depicted by the blue-dashed and red-dotted curves, respectively.

ICD spectrum (black-solid curve) is then the sum of the two spectra from the $^1\Pi$ and $^1\Sigma$ micro-states. Again, the nuclear dynamics does not have much influence on the spectrum, as we already expected.

There is not much to say about the ICD spectrum of channel 2. Its shape is very similar to the result shown in Fig. 3.3, but this spectrum is centered at 4.9 eV. Its intensity is also weaker in comparison to the other two channels. Therefore, let us concentrate on the more interesting channel 3. The reader can find the spectrum of channel 2 published in Ref. [42].

Unlike the spectrum of channel 1, it is expected that the nuclear dynamics have a strong influence on the ICD electron spectrum of channel 3 due to the longer lifetime of its intermediate states. Again we begin with one single partial channel, namely

$$\mathrm{Ne}^{2+}(2s^{-1}2p^{-1}\ {}^3P)\mathrm{Ar}\ [{}^3\Pi] \rightarrow \mathrm{Ne}^{2+}(2p^{-2}\ {}^3P) - \mathrm{Ar}^{+}\ [{}^2\Delta] + e^{-}_{\mathrm{ICD}}\ ,$$

whose time-resolved spectrum is shown Fig. 3.4(a). The time-resolved spectrum evaluated via Eq. (3.31) already shows an asymmetric feature at 140 fs, which is around half a period of the wave packet motion, cf. Fig. 3.2(c). When the whole decay is finished, the ICD electron spectrum (black-solid curve) deviates strongly from the one estimated via the mirror-reflection principle [23, 56] (orange-dotted curve). Except from having a strongly asymmetric shape, the numerical spectrum also centers at smaller electron kinetic energies because the wave packet now has more time to explore the region of smaller R before it decays completely. In consequence, the probability of the wave packet decaying from a smaller R, producing a lower kinetic energy electron, is higher in the case of the triplet $\mathrm{Ne}^{2+}(2s^{-1}2p^{-1})\mathrm{Ar}$ state. Based on the simulation, we do see a stronger nuclear dynamics in the ICD channel 3.

Concerning the spectral intensity, the spectrum shown in Fig. 3.4(a) has been multiplied with the Auger branching ratio (6.5%) of the triplet state $\mathrm{Ne}^{2+}(2s^{-1}2p^{-1}\ {}^3P)\mathrm{Ar}$. Similar to the case of channel 1, this naïve multiplication omits the state degeneracy of $\mathrm{Ne}^{2+}(2s^{-1}2p^{-1}\ {}^3P)\mathrm{Ar}$. The corresponding statistical average has been performed in order to obtain the total ICD spectrum; results are depicted in Fig. 3.4(b).

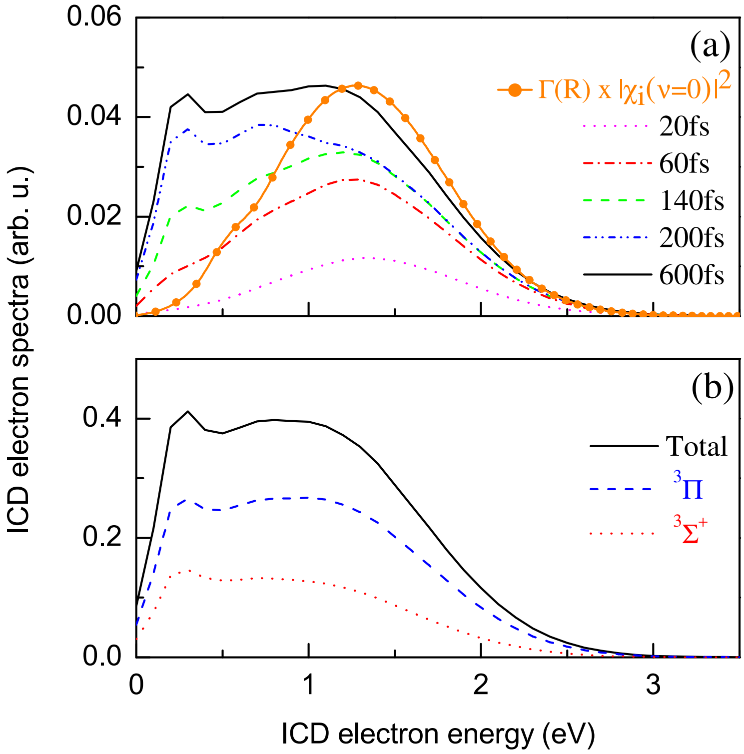

Figure 3.4: ICD electron spectra of channel 3. Panel (a): the time-resolved ICD electron spectra of one partial channel (see text). The spectrum shows a strong deviation from the prediction obtained via the mirror-reflection principle, which does not consider the nuclear dynamics (orange-dotted line). Panel (b): the total ICD spectrum and its contributions from $^3\Pi$ and $^3\Sigma$ micro-states. This result verifies the prediction that the nuclear dynamics play a strong role in the triplet ICD channel.

Chapter 4

ICD following the K-LL Auger process of Ne in NeAr (II)

Our numerical electron spectra, shown in Sec. 3.3, have been published in 2009 [42] in order to promote experiments on hetero-atomic systems. Later in 2010, Ouchi *et al.* have performed experiments for the NeAr system [57]. Naturally, our discussions will continue starting from the comparison between our numerical electron spectra and experiment.

4.1 Comparison with Experiments

In the experiment, electron-ion multicoincidence spectroscopy was employed to identify the ICD channels. In other words, both the ICD electron and the ionic fragments were measured, but only the KER spectra[1] of the produced ions Ne^{2+} and Ar^{+} were reported because the electron spectra have rather low resolution [57].

How can we compare the two different physical quantities, namely the energy distribution of the emitted ICD electrons and the energy distribution of the ionic fragments? There is an empirical rule, namely the *mirror-image principle*[2], which allows us to compare the ICD electron spectrum and the ICD KER spectrum [10, 12]. This empirical rule states that the electron spectrum and the KER spectrum are mirror images of each other due to the conservation of the total energy, i.e. $E_{e_2} + E_{\mathrm{KER}}$. Therefore,

---

[1] KER is the gain of the total translational energy of all fragmented ions from a dissociation process.

[2] One should not confuse this with the mirror-reflection principle from Sec. 3.3. The mirror-reflection principle is a way of estimating a spectrum, using only the initial wave function and the potential energy curves.

a total ICD electron spectrum is then reversed along the energy axis to yield its corresponding "numerical" KER spectrum[3]. This mapping depends on the total energy of a channel. For example, the total energy is 16.65 eV and 9.25 eV for channel 1 and channel 3, respectively. The numerical KER spectra are then additionally convoluted with a Gaussian function, whose full-width at half maximum (FWHM) is 0.7 eV, to account for the experimental resolution.

The numerical and experimental KER spectra are depicted in Fig. 4.1 by the dashed line and the solid-dotted curve, respectively. Shown in Fig. 4.1(b) are the spectra of channel 3. Our calculation agrees very well with experiment, proving that the nuclear dynamics do affect the spectrum of channel 3. However, the numerical KER spectrum of channel 1, shown in Fig. 4.1(a), does not match the experimental observation. In comparison with our simulation, the experiment shows more ions with higher E_{KER}. These ions can only be produced when the ICD process takes place while the wave packet $|\psi_{d_{2_\beta}}(t)\rangle$ is located at a smaller R. For example, ions with $E_{\mathrm{KER}} > 10$ eV can only be produced from $R < 2.9$ Å, cf. Fig. 3.1. In other words, the experiment indicates that the nuclear wave packet $|\psi_{d_{2_\beta}}(t)\rangle$ decays more often from a smaller R than what we expected for ICD channel 1. How could this happen? There are two possibilities. One is that the wave packet already moved toward a smaller internuclear distance during the Auger decay process, which has been neglected so far. The other is that the ICD transition rate is lower than the current theoretical one, leading to a longer lifetime of the state $\mathrm{Ne}^{2+}(2s^{-1}2p^{-1}\,{}^1P)\mathrm{Ar}$. We shall investigate both possibilities in this chapter. One might wonder if this disagreement between experiment and theory stems from the mirror image principle, which is employed for evaluating the KER spectrum from the numerical electron spectrum. In Ch. 6, we will show the validity of the mirror image principle for this case.

4.2 Theory

The general EOMs for the ICD following an Auger decay process have been illustrated in Sec. 3.2, namely Eqs. (3.2-3.5). The initial wave function is chosen as the lowest vibrational eigenfunction of state i, i.e. $|\psi_i(0)\rangle = |\chi_i(\nu = 0)\rangle$. Following the broad-band ionization, this initial wave packet is then directly transfered onto the first intermediate state d_1.[4] Besides, the ground state wave packet motion is trivial as the laser pulse is too weak to influence it; hence it is not of interest here.

---

[3] Please note that this "numerical" KER spectrum is merely a prediction of the actual numerical KER spectrum. The evaluation of the actual numerical KER spectrum will be the subject of Ch. 6.

[4] The photoionization process is usually considered as a broad-band ionization process since the photoelectron can take an arbitrary amount of energy, resulting in an initial condition equivalent to using a broad-band pulse.

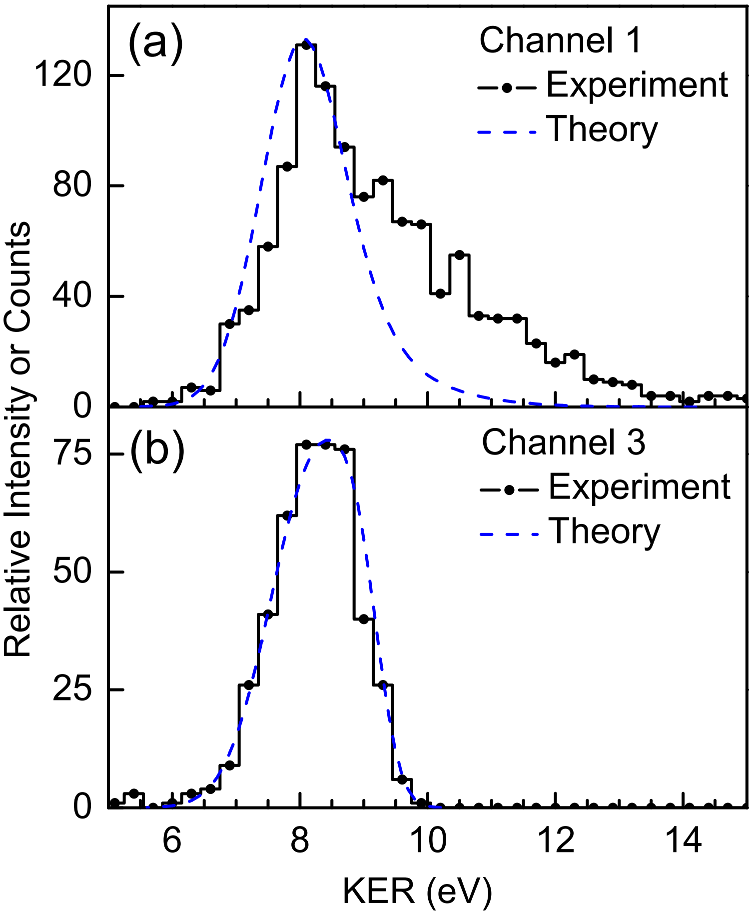

Figure 4.1: The experimental and theoretical KER spectra of ICD channel 1 and channel 3 (see Table 3.1) . The numerical KER spectra are obtained from our numerical ICD electron spectra via an empirical mirror-image rule (see text) and additionally are convoluted with a Gaussian function, FWHM 0.7 eV, to account for the experimental resolution. Panel (a): KER spectra of ICD channel 1. The numerical and experimental KER spectra are depicted by the dashed curve and the solid-dotted curve, respectively. The experiment observes more ions with large kinetic energy release than our theory predictions, showing a strong nuclear dynamics effect. Panel (b): KER spectra of ICD channel 3. In contrast to channel 1, the experimental and numerical KER spectra of channel 3 agree very well.

Because the photoelectron energy E_{e_0} appears in all three EOMs as a constant potential operating on all wave packets, it contributes only a trivial phase $e^{-iE_{e_0}t}$ to their time-dependence. Thus E_{e_0} can be removed by the dressed state method (see Sec. 3.2), yielding the working equations for the two-step decay. Following the same procedure as introduced in Sec. 3.2, we obtain the working equations, which read

$$\begin{aligned} i|\dot{\psi}_{d_1}(t)\rangle &= \hat{\mathcal{H}}_{d_1}|\psi_{d_1}(t)\rangle && (4.1)\\ i|\dot{\psi}_{d_{2_\beta}}(E_{e_1},t)\rangle &= \hat{W}_{d_1\to d_{2_\beta}}|\psi_{d_1}(t)\rangle + (\hat{\mathcal{H}}_{d_{2_\beta}} + E_{e_1})|\psi_{d_{2_\beta}}(E_{e_1},t)\rangle && (4.2)\\ i|\dot{\psi}_{f_\gamma}(E_{e_1},E_{e_2},t)\rangle &= \hat{W}_{d_{2_\beta}\to f_\gamma}|\psi_{d_{2_\beta}}(E_{e_1},t)\rangle + (\hat{H}_{f_\gamma} + E_{e_1} + E_{e_2})|\psi_{f_\gamma}(E_{e_1},E_{e_2},t)\rangle, && (4.3)\end{aligned}$$

where $|\psi_{d_1}(t)\rangle$, $|\psi_{d_{2_\beta}}(E_{e_1},t)\rangle$, and $|\psi_{f_\gamma}(E_{e_1},E_{e_2},t)\rangle$ are the dressed nuclear wave functions. The initial wave packet is chosen to be

$$|\psi_{d_1}(0)\rangle = |\chi_i(\nu = 0)\rangle \ . \tag{4.4}$$

The nuclear Hamiltonians expressed with the decay widths read

$$\begin{aligned}\hat{\mathcal{H}}_{d_1} &= \hat{H}_{d_1} - \frac{i}{2}\Gamma_{d_1} = \hat{H}_{d_1} - \sum_{\beta'} i\pi|\hat{W}_{d_1\to d_{2_{\beta'}}}|^2\\ \hat{\mathcal{H}}_{d_{2_\beta}} &= \hat{H}_{d_{2_\beta}} - \frac{i}{2}\Gamma_{d_{2_\beta}} = \hat{H}_{d_{2_\beta}} - \sum_{\gamma'} i\pi|\hat{W}_{d_{2_\beta}\to f_{\gamma'}}|^2 \ .\end{aligned} \tag{4.5}$$

The partial time-resolved coincidence spectrum (with a relative intensity) of e_1 (Auger electron) and e_2 (ICD electron) for a specific channel γ is given by the final state's population [12]

$$\sigma^{(\gamma)}(E_{e_1},E_{e_2},t) = \langle\psi_{f_\gamma}(E_{e_1},E_{e_2},t)|\psi_{f_\gamma}(E_{e_1},E_{e_2},t)\rangle \ . \tag{4.6}$$

Gathering all events irrespective of time yields the non-time-resolved partial coincidence spectrum of e_1 and e_2 :

$$\sigma^{(\gamma)}(E_{e_1},E_{e_2}) = \lim_{t\to\infty}\sigma^{(\gamma)}(E_{e_1},E_{e_2},t) \ . \tag{4.7}$$

Integrating over all possible Auger electron energies (E_{e_1}) yields the time-resolved partial ICD electron spectrum, which reads

$$\sigma^{(\gamma)}_{e_2}(E_{e_2},t) = \int \mathrm{d}E_{e_1}\,\langle\psi_{f_\gamma}(E_{e_1},E_{e_2},t)|\psi_{f_\gamma}(E_{e_1},E_{e_2},t)\rangle \ . \tag{4.8}$$

As before, the non-time-resolved partial ICD electron spectrum reads

$$\sigma^{(\gamma)}_{e_2}(E_{e_2}) = \lim_{t\to\infty}\sigma^{(\gamma)}_{e_2}(E_{e_2},t) \ . \tag{4.9}$$

The total ICD spectrum is then given by the summation over all these partial spectra. In contrast to Sec. 3.2, no additional multiplication with the Auger branching ratio is required here because this is automatically included in a full cascade simulation.

One goal of performing the full cascade simulation is that it allows us to evaluate the time-resolved Auger spectrum. Interestingly, direct integration over a partial time-resolved coincidence spectrum, similar to what is done in Eq. (4.8) for the ICD electron spectrum, does not lead to the correct time-resolved partial Auger electron spectrum. In fact, the correct time-resolved Auger electron spectrum of state d_{2_β} reads

$$\sigma_{e_1}^{(\beta)}(E_{e_1},t) = \langle\psi_{d_{2_\beta}}(E_{e_1},t)|\psi_{d_{2_\beta}}(E_{e_1},t)\rangle + \int_0^t \mathrm{d}t' \, \langle\psi_{d_{2_\beta}}(E_{e_1},t')|\Gamma_{d_{2_\beta}}|\psi_{d_{2_\beta}}(E_{e_1},t')\rangle \; . \tag{4.10}$$

The derivation will be discussed in detail in Ch. 5. We only mention that the non-time-resolved partial Auger electron spectrum reads

$$\sigma_{e_1}^{(\beta)}(E_{e_1}) = \lim_{t\to\infty} \sigma_{e_1}^{(\beta)}(E_{e_1},t) \; , \tag{4.11}$$

which is formally equivalent to Eq. (2.61) and is numerically efficient. The total Auger spectrum is given by the summation over all partial Auger spectra.

4.3 Numerical Auger and ICD Electron Spectra

As we mentioned in Sec. 4.1, the nuclear dynamics during the Auger process might not be negligible. To investigate this possibility, the working equations Eqs. (4.1-4.3) are employed to simulate the full cascade process of the ICD following an Auger decay. The potential curves and ICD rates are taken the same as those were illustrated in Sec. 3.3.

Let us begin with the time-resolved Auger electron spectrum for the process

$$\mathrm{Ne}^+(1s^{-1})\mathrm{Ar} \to \mathrm{Ne}^{2+}(2s^{-1}2p^{-1}\,{}^1P)\mathrm{Ar} + e^- \; .$$

The time-resolved Auger electron spectra for this process, depicted in Fig. 4.2(a), is obtained by summing over all time-resolved partial spectra, which are evaluated according to Eq. (4.10). In the beginning, the energy distribution of the Auger electron energy E_{e_1} is broader than at later times. The spectrum evolves in a way that the "uncertainty" of the energy distribution becomes smaller[5]. The reason of such a development will be discussed in detail in Sec. 6.4. The time-resolved Auger spectrum is converged after 30 fs; this is consistent with the expected lifetime of $\mathrm{Ne}^+(1s^{-1})$, i.e. 2.4 fs.

---

[5] One should not confuse this with the time-energy uncertainty principle, which states that a state with a finite lifetime could not have a well-defined energy.

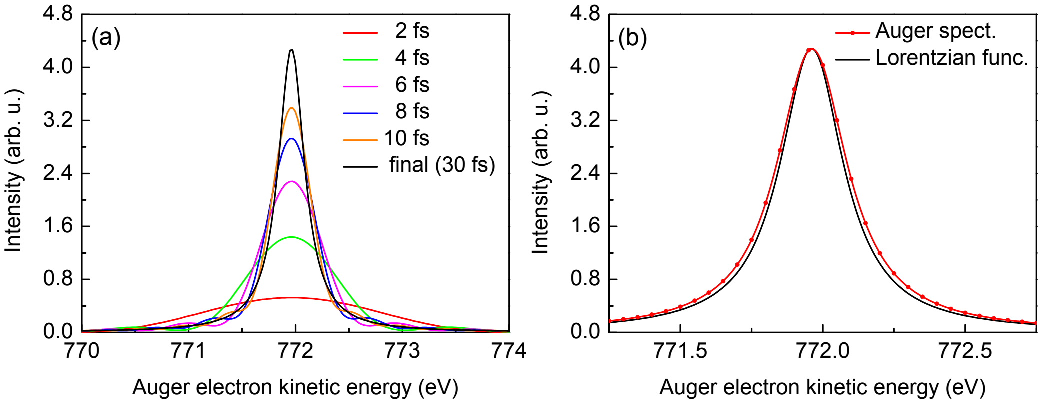

Figure 4.2: The Auger electron spectrum for the process $\mathrm{Ne}^{+}(1s^{-1})\mathrm{Ar} \rightarrow \mathrm{Ne}^{2+}(2s^{-1}2p^{-1}\ ^1P)\mathrm{Ar} + e^{-}$. Panel (a): The time-resolved Auger electron spectrum. The Auger electron energy distribution is very broad in the beginning, e.g. at 2 fs, and as time increases, this “energy uncertainty” gradually disappears, leading to a narrower spectrum. The final spectrum is depicted by the black curve. Panel (b): The final numerical Auger electron spectrum and a Lorentzian function with a FWHM 270 meV. From the numerical Auger spectrum, we obtain a FWHM of 293 meV, which is larger than the natural width of $\mathrm{Ne}^{+}(1s^{-1})$, which is 270 meV [47]. The excess part of the width is equivalent to the total width of the following ICD process at the equilibrium internuclear distance.

Due to the extremely short lifetime of state d_1 in comparison to the nuclear vibrational period, the Auger spectrum is essentially the same as the Auger spectrum without considering the nuclear motion, i.e. the Auger spectrum of an individual Ne atom. It is known that the line shape for a single decay process in an atom is given by a Lorentzian function with the decay width as its FWHM [58]. Indeed, the final Auger spectrum shown in Fig. 4.2(a) appears like a Lorentzian function with a FWHM of 270 meV [47]. However, the comparison of the total Auger spectrum and a Lorentzian function of this FWHM shows that the total Auger spectrum is actually slightly broader compared to the Lorentzian function, see Fig. 4.2(b). This broadening effect due to the presence of the second decay process has been known in atomic cascade processes [31], and it will be explained in Ch. 5. The FWHM of the Auger spectrum shown in Fig. 4.2(b) is around 293 meV, which is 23 meV more than the prediction based on the lifetime. Interestingly, the total ICD width of the state $\mathrm{Ne}^{2+}(2s^{-1}2p^{-1}\ ^1P)\mathrm{Ar}$ is around 21 meV at the equilibrium internuclear distance (3.5 Å). The FWHM of the Auger process is then approximately equivalent to the summation of its own natural width and the total width of the following ICD processes.

We now turn to the total ICD electron spectrum, which can be obtained by summing over all partial ICD electron spectra, evaluated via Eq. (4.9). The result is depicted by the red-dotted curve in Fig. 4.3. To compare, the total ICD electron spectrum, evaluated with the fast Auger decay approximation (already shown in Fig. 3.3) is also depicted in Fig. 4.3 by the black curve. The difference between the two results is

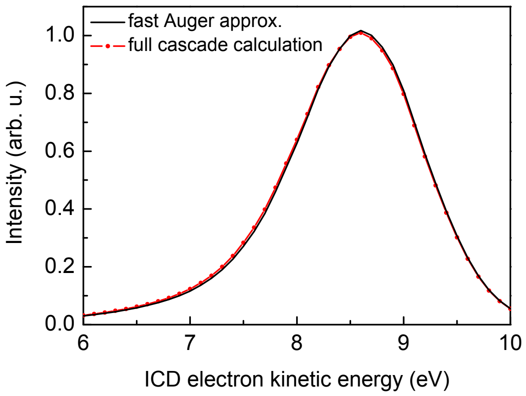

Figure 4.3: The numerical ICD electron spectrum, calculated via a full cascade calculation (red-dotted curve) and via the fast Auger decay approximation (black curve). The difference between the two curves is almost negligible, proving that the fast Auger decay approximation is indeed valid. The strong nuclear dynamics fingerprint in the spectrum can not be explained by the nuclear dynamics during the Auger process.

basically negligible. Hence there can be no doubt that the fast Auger decay assumption is valid. In consequence, the nuclear dynamics during the Auger decay is not responsible for the strong nuclear dynamics fingerprint, which was observed in the experiment.

4.4 ICD Rates and Nuclear Dynamics

The other possibility to account for the experimental observation is a smaller ICD transition rate, which would allow the wave packet to travel to a smaller internuclear distance and decay from there. This suggestion is based on the fact that the transition rate is often notoriously difficult to compute because continuum wave functions must be included in the computation [41]. The current ICD transition rate is calculated via the Fano-Stieltjes-Lanczos method [48, 59], which is already known to be one of the best methods for treating the discrete continuum, see Ref. [59]. However, this method does not provide an accurate partial decay width for each partial channel γ [48] but only provides a total decay width of an intermediate state d_{2_β} to all final states[6]. Additionally, the current *ab initio* calculation is also limited by the number of configurations that the computer program allows [41]. Therefore, it is a *reasonable assumption* that the ICD transition rate was overestimated previously and the experimental observation indicates a lower ICD rate. One can also question the quality of the potential curve. An investigation showed that the wave packet travels slightly faster when the potential curve of $\mathrm{Ne}^{2+}(2s^{-1}2p^{-1}\ {}^1P)\mathrm{Ar}$ becomes 1.5 times steeper. Yet this

---

[6] Our simulation is done under the assumption that all partial decay widths are equal. The same assumption has been applied to the ICD following the K-LL Auger process in the Ne dimer, and the agreement between experiments and theory was excellent [42].

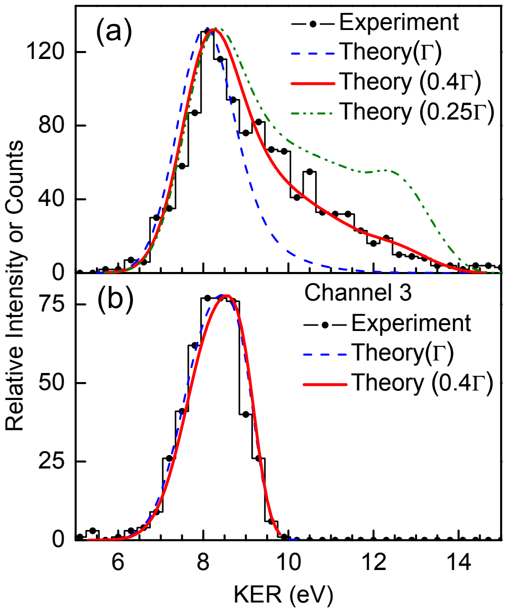

Figure 4.4: The KER distributions for ICD channel 1, shown in panel (a), and for ICD channel 3, shown in panel (b). The theoretical KER distributions are evaluated for three different ICD rates: the *ab initio* width (Γ), 0.4 times the *ab initio* width (0.4Γ), and one quarter of the *ab initio* width (0.25Γ). In panel (a), the theoretical KER distributions vary with different ICD rates. The lower the rate is, the more fragments have higher KER energy. The best fit to the experimental results is achieved for 0.4Γ. In panel (b), the ICD transition rate does not play a role in the shape of the spectrum. Even the calculation with a smaller ICD width provides good agreement with the experimental observation. All theoretical results are convolved with a Gaussian function (FWHM 0.7 eV) to account for the experimental resolution, and their intensities are scaled to the maximum of the experimental result.

rather strong change of the potential is not enough to explain the observed ICD electron spectrum. Therefore, here we concentrate on altering only a single parameter, i.e. the ICD transition rate.

What is the suggested ICD width? To proceed, the ICD electron spectrum was evaluated by using a modified transition rate, which was taken to be the *ab initio* rate multiplied by a constant (< 1). Several different values of the constant were tried. Then, the mirror imaging procedure was again applied to transform this numerical ICD electron spectrum into its corresponding "numerical" KER spectrum. In addition, the numerical spectra were convolved with a Gaussian function with FWHM 0.7 eV to account for the experimental resolution.

Shown in Fig. 4.4 are our theoretical results with three different ICD widths, together with the KER distributions observed by experiments. The *ab initio* width (Γ) is taken from the calculation reported in Ref. [48] and the modified ones are this *ab initio* width multiplied by 0.4 (0.4Γ) and 0.25 (0.25Γ). The KER distributions for ICD channel 1 are depicted in Fig. 4.4 (a). With a lower ICD transtion rate, the wave packet has enough time to move to a smaller internuclear distance R before it decays completely. In consequence, the system, $\mathrm{Ne}^{2+}(2s^{-1}2p^{-1}\ {}^1P)\mathrm{Ar}$, emits more ICD electrons with lower energy and more ion pairs with higher E_{KER}. The best agreement with the experiment is found at 0.4 times the *ab initio* rate.

In contrast, the numerical KER distributions for ICD channel 3, shown in Fig. 4.4 (b), do not vary when a lower ICD rate is employed in the simulation. Because this ICD channel is only open for $R > 3$ Å, the change of the spectrum is very tiny when varying the decay width. This tiny change is even smaller than the current experimental resolution and can not be observed.

Is there any way to check whether our suggested ICD rate is the accurate? In Ref. [57] it was admitted that other methods than Fano-Stieltjes-Lanczos are required to evaluate the transition rate in more detail. Here we suggest a different approach. We already mentioned that the FWHM of the Auger electron spectrum is composed of two sources: The natural width of the Ne $1s$ Auger decay, and the total width of the ICD process at the equilibrium position R. Measuring the Auger electron spectrum of the cascade process (with a resolution of 10 meV) and subtracting the natural width of the Ne $1s$ Auger decay would then yield reliable total ICD rates, which can be compared with the currently suggested ICD rates at the equilibrium R. Such a suggested experiment could concentrate on only measuring the Auger electron, hence it is expected to be easier than the usual coincidence measurement.

4.5 Summary

The full cascade simulation allows us to evaluate the time-resolved electron spectrum for the Auger process, which takes place before the ICD process in NeAr. The broadening of the Auger spectrum is found to be caused by the finite lifetime of the state $\mathrm{Ne}^{+}(1s^{-1})\mathrm{Ar}$ as well as by the finite lifetime of the state $\mathrm{Ne}^{2+}(1s^{-1}1p^{-1}\ {}^1P)\mathrm{Ar}$. This leads to a new technique for measuring the ICD rates at the equilibrium internuclear distance. Besides, our full cascade calculation demonstrates that the fast Auger decay approximation is an excellent approximation for the ICD following the Auger decay of $\mathrm{Ne}^{+}(1s^{-1})$ in NeAr. In consequence, the experimental observation of a strong nuclear dynamics footprint in the spectra of ICD channel 1 can be reasonably assumed to be an effect of a lower ICD rate. The comparison between many simulated spectra and the experimental one yields the best suggested ICD rate, which is 0.4 times the rate obtained by *ab initio* computations. This suggested rate can be confirmed (or disproved) by measuring the Auger electron spectrum of the first decay process (with a resolution of around 10 meV).

Interestingly, the ICD following Auger decay process in NeAr is one of the few studied ICD processes (in a noble gas dimer) which do not close at a small internuclear distance. Another one is the ICD in the He dimer [13, 14, 24]. In the He dimer case, it was already proved that the ICD rate is low, and the KER spectrum has the vibrational structure [13, 14]. The transition rate for the ICD in the He dimer has also been evaluated by the most accurate Fano-Stieltjes-Lanczos computation to date [13].

For our present case, we have already seen that the experiment suggests a lower ICD rate than predicted from *ab initio* computations. First, the current Fano-Stieltjes-Lanczos method does not provide partial ICD widths of each channel [57]. Second, the current code for the Fano-Stieltjes-Lanczos method does not include more than 2-hole-2-particle configurations [41], which might be required in the current case. However, the current study focuses on the molecular dynamics, so a more accurate *ab initio* computation for the decay rate is left for a future study.

Chapter 5

An Atomic Level Model for Cascade Processes

The previous simulation for the cascade process of interest, i.e. the ICD process following Auger decay of $\mathrm{Ne}^{+}(1s^{-1})$ in NeAr, has shown that the ICD transition rate could be obtained by measuring the Auger electron spectrum. Additionally, the time-resolved Auger electron spectrum was simulated according to Eq. (4.10), which will be derived in this chapter. For simplicity, a singe channel cascade process in atomic levels is chosen as an example. The theory developed here can be easily adapted to describe a diatomic system, as shown in Eqs. (4.8-4.10).

5.1 Theory

In order to keep the physics as simple as possible, we begin with a two-step Auger cascade processes, induced by a broad-band excitation[1]. The atomic levels are depicted schematically in Fig. 5.1. The system initially in its electronic ground state i is excited to the first intermediate state d_1, from which an Auger electron (e_1) with the kinetic energy E_{e_1} is emitted, and subsequently the system decays to the second intermediate state d_2. From this state d_2, the system decays to the final state f by emitting another Auger electron (e_2) with a kinetic energy E_{e_2}. The energy of each state α is denoted by E_α, where $\alpha = i, d_1, d_2, f$, and the two emitted Auger electrons are distinguishable by their kinetic energies E_{e_1} and E_{e_2} [60].

---

[1] A broad-band excitation refers to the excitation process carried out by a pulse with a large photon band-width. It can be performed practically by a pulse whose duration is shorter than the life time of the intermediate state.

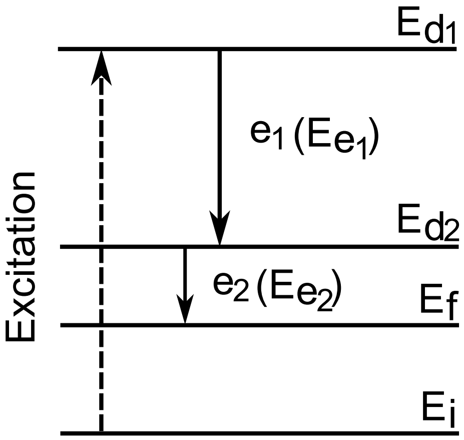

Figure 5.1: Schematic atomic energy levels of a two-step Auger cascade process. The four energy levels involved are shown, namely: the ground state i with energy E_i, the first and second intermediate states d_1 and d_2 with energies E_{d_1} and E_{d_2}, respectively, and the doubly ionic final state f with energy E_f. The process is initiated by a broad-band excitation, depicted by dashed-line. The excited state d_1 has a finite lifetime and can decay via emission of one electron e_1 with a kinetic energy E_{e_1}. Similarly, the state d_2 also relaxes through emission of one electron e_2 with a kinetic energy E_{e_2}. All levels are assumed to be non-degenerate.

The wave function ansatz here is slightly different from Eq. 2.2, since there is no relative nuclear motion in atomic levels and there is no photoelectron in an excitation process. The total wave function ansatz then reads

$$\begin{aligned}|\Psi(t)\rangle &= a_i(t)|\Phi_i\rangle + a_{d_1}(t)|\Phi_{d_1}\rangle + \int dE_{e_1}\ a_{d_2}(E_{e_1},t)|\Phi_{d_2},E_{e_1}\rangle \\ &+ \iint dE_{e_1}\ dE_{e_2}\ a_f(E_{e_1},E_{e_2},t)\rangle|\Phi_f,E_{e_1},E_{e_2}\rangle\ , \qquad (5.1)\end{aligned}$$

where $a_\alpha(t)$ and $|\Phi_\alpha\rangle$ denote the time-dependent coefficient, i.e. the amplitude, and the electronic wave function of state α, respectively. For the state d_2 and state f, their electronic wave functions and their coefficients are additionally augmented to the wave function(s) and the coefficient(s) of the emitted electron(s).

Following the same procedure presented in Sec. 2.1, the EOMs of a cascade decay in the atomic levels, under a weak field and broad-band excitation, reads

$$\begin{aligned} i\dot{a}_{d_1}(t) &= \left[E_{d_1} - \frac{i}{2}\Gamma_{d_1}\right] a_{d_1}(t)\ , & (5.2)\\ i\dot{a}_{d_2}(E_{e_1},t) &= W_{d_1\to d_2}a_{d_1}(t) + \left[E_{d_2} + E_{e_1} - \frac{i}{2}\Gamma_{d_2}\right] a_{d_2}(E_{e_1},t)\ , & (5.3)\\ i\dot{a}_f(E_{e_1},E_{e_2},t) &= W_{d_2\to f}a_{d_2}(E_{e_1},t) + \left[E_f + E_{e_1} + E_{e_2}\right] a_f(E_{e_1},E_{e_2},t)\ . & (5.4)\end{aligned}$$

Additionally, the initial conditions are $a_{d_1}(0) = 1$ and $a_{d_2}(0) = a_f(0) = 0$. By $W_{d_2\to f}$ we denote the transition element from state d_2 to state f, which is related to the total decay width Γ_{d_2} ,by the local approximation, giving $\Gamma_{d_2} = 2\pi|W_{d_2\to f}|^2$. Similarly, the total decay width of the state d_1 reads $\Gamma_{d_1} = 2\pi|W_{d_1\to d_2}|^2$. These equations are very similar to Eq. (2.19) except for the fact that the current process begins with a broad-band excitation, i.e. no phototelectron energy E_{e_0}, and with a weak field approximation, i.e. the equation of motion for the ground state i is trivial and not relevant. Besides, the current time-dependent amplitude of each electronic state is a coefficient instead of the nuclear wave function.

The goal of this chapter is to investigate the time-resolved electron spectra of the first decay process. To proceed, we begin with the multi-electron coincidence spectrum, see also Sec. 2.4. The physical meaning of the final state coefficient $a_f(E_{e_1}, E_{e_2}, t)$ is the time-dependent amplitude of finding the system at the electronic final state f with e_1 having an energy E_{e_1} and e_2 an energy E_{e_2}. Straightforwardly, the probability of finding e_1 and e_2 with energies E_{e_1} and E_{e_2}, i.e. the time-resolved electron-electron coincidence spectrum, is given by

$$\sigma(E_{e_1}, E_{e_2}, t) = |a_f(E_{e_1}, E_{e_2}, t)|^2 \ . \tag{5.5}$$

The collection of all events, decaying to state f via electron emission, irrespective of time, gives the usual non-time-resolved electron-electron coincidence spectrum. It reads

$$\sigma(E_{e_1}, E_{e_2}) = \lim_{t\to\infty} |a_f(E_{e_1}, E_{e_2}, t)|^2. \tag{5.6}$$

Similar to the procedure described in Sec. 3.2, the integration of the coincidence spectrum over E_{e_1} yields the electron spectrum of e_2, and vice versa. The non-time-resolved electron spectra are obtainable from

$$\sigma_{e_1}(E_{e_1}) \ = \ \int_0^\infty \mathrm{d}E_{e_2} \lim_{t\to\infty} |a_f(E_{e_1}, E_{e_2}, t)|^2 \ , \tag{5.7}$$

$$\sigma_{e_2}(E_{e_2}) \ = \ \int_0^\infty \mathrm{d}E_{e_1} \lim_{t\to\infty} |a_f(E_{e_1}, E_{e_2}, t)|^2 \ . \tag{5.8}$$

In practice, the integration over electron energies is only performed in the energy range where the electrons appear. Moreover, the current coincidence measurement is not the only way to obtain the two electron spectra, i.e. they can be measured independently if e_1 and e_2 are well separated in energy. For instance, tracing the kinetic energy distribution of e_2 in time leads to the time-resolved spectrum of e_2, which reads

$$\sigma_{e_2}(E_{e_2}, t) = \int_0^\infty \mathrm{d}E_{e_1} \ |a_f(E_{e_1}, E_{e_2}, t)|^2 \ . \tag{5.9}$$

The electron spectrum of e_2, i.e. Eq. (5.8), is equivalent to its time-resolved electron spectrum, e.g. Eq. (5.9), accumulated till $t \to \infty$. Similarly, the time-resolved spectrum of e_1 might be introduced naïvely as

$$\sigma_{e_1}(E_{e_1}, t) = \int_0^\infty \mathrm{d}E_{e_1} \ |a_f(E_{e_1}, E_{e_2}, t)|^2 \ . \tag{5.10}$$

Although Eq. (5.10) indeed reproduces Eq. (5.7) under the limit $t \to \infty$, it surprisingly *cannot* describe how the spectrum evolves in time. The problem of this equation will be discussed in Sec. 5.2. On the other hand, the correct time-resolved spectrum of e_1, i.e. Eq. (5.11):

$$\sigma_{e_1}(E_{e_1}, t) = |a_{d_2}(E_{e_1}, t)|^2 + \int_0^\infty \mathrm{d}E_{e_2} \, |a_f(E_{e_1}, E_{e_2}, t)|^2 \, , \tag{5.11}$$

will also be discussed in in Sec. 5.2.

As a remark, we mentioned that the spectra of e_1 and of e_2 can be solved analytically[2][61]:

$$\sigma_{e_1}(E_{e_1}) = \frac{1}{\pi} \frac{\left(\Gamma_{d_1} + \Gamma_{d_2}\right)/2}{\left(E_{d_2} - E_{d_1} + E_{e_1}\right)^2 + \left(\Gamma_{d_1} + \Gamma_{d_2}\right)^2/4}, \tag{5.12}$$

$$\sigma_{e_2}(E_{e_2}) = \frac{1}{\pi} \frac{\left(\Gamma_{d_2}\right)/2}{\left(E_f - E_{d_2} + E_{e_2}\right)^2 + \left(\Gamma_{d_2}\right)^2/4} \, . \tag{5.13}$$

Both line shapes are Lorentzian functions. As a single step decay process often described in the literatures [58], $\sigma_{e_2}(E_{e_2})$ has a full-width at half maximum (FWHM) Γ_{d_2}. Interestingly, $\sigma_{e_1}(E_{e_2})$ is also a Lorentzian function, but it has an effective width of $\Gamma_{d_1} + \Gamma_{d_2}$. This phenomenon is already known from experiment [60] and explained by theory [62] using the argument of energy uncertainty due to the second intermediate state. Here, we borrow the uncertainty picture to illustrate the line broadening. Due to the finite lifetime of d_1, its energy is between $E_{d_1} - \Gamma_{d_1}/2$ and $E_{d_1} + \Gamma_{d_1}/2$, that is its energy uncertainty is Γ_{d_1}. This resonance state decays to the state d_2 which by itself is also a resonance state with between $E_{d_2} - \Gamma_{d_2}/2$ and $E_{d_2} + \Gamma_{d_2}/2$. The spectrum of e_1 comprises all possible energy differences between the two resonances, and thus varies from $(E_{d_1} - E_{d_2}) - (\Gamma_{d_1} + \Gamma_{d_2})/2$ to $(E_{d_1} - E_{d_2}) + (\Gamma_{d_1} + \Gamma_{d_2})/2$.

5.2 Lifetime of State d_1 and Time-Resolved Spectra

According to the time-energy uncertainty principle, a state with a finite lifetime τ cannot have a definite energy. The intermediate state can decay via electron or photon emission and, in consequence, a spectrum of the emitted particle will have an energy distribution, namely the natural width Γ. It is already known that Γ and τ are related via $\Gamma = \frac{1}{\tau}$ [58] for a single decay process. In practice, measuring the natural width of an electron spectrum or photoelectron spectrum has been applied to determine the lifetime of an intermediate state. Naturally, we ask: does the line width of σ_{e_1} in a cascade process also reflect the lifetime of the state d_1?

---

[2] Using that the energy gaps are substantially larger than the decay widths.

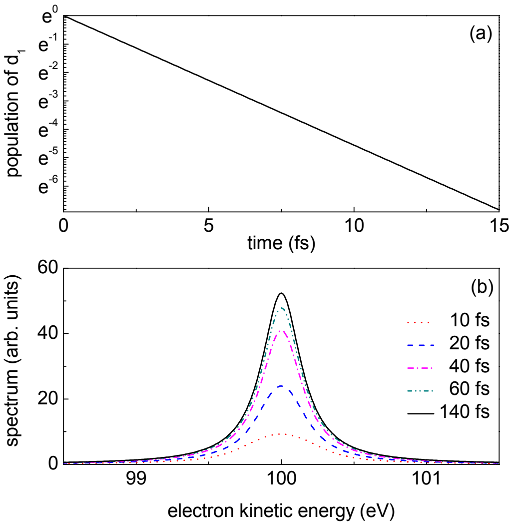

Figure 5.2: The contradictory time scales of the first decay process. Panel (a) depicts how the population $|a_{d_1}(t)|^2$ decreases in time. Since the state d_1 depopulates exponentially, the first decay process is completed in less than 20 fs. Panel (b): the time-resolved spectrum $\sigma_{e_1}(E_{e_1}, t)$ calculated by Eq. (5.10). Strangely, the spectrum does not converge at 20 fs, as one will expect from the depopulation time of state d_1. Instead, the spectrum reaches its final form at about 140 fs.

The line width of σ_{e_1}, as already shown in Eq. (5.12), is $\Gamma_{d_1} + \Gamma_{d_2}$. A naïve estimation of the lifetime according to the usual relation reads $1/(\Gamma_{d_1} + \Gamma_{d_2})$ (with $\hbar = 1$). On the other hand, following Eq. (5.2) the population of state d_1, given by $|a_{d_1}(t)|^2$, reads

$$|a_{d_1}(t)|^2 = e^{-\Gamma_{d_1} t} |a_{d_1}(0)|^2 \; . \tag{5.14}$$

Importantly, according to Eq. (5.14), the *true* lifetime of state d_1 is $1/\Gamma_{d_1}$. Clearly the line width of σ_{e_1} does not give the correct lifetime of state d_1 due to the presence of the second decay process. Then, if we trace the development of the electron spectrum directly in time, i.e. measuring the time-resolved spectrum, $\sigma_{e_1}(E_{e_1}, t)$ should reflect the correct lifetime of state d_1. To test this hypothesis, the numerical time-resolved electron spectrum $\sigma_{e_1}(E_{e_1}, t)$ and the population of state d_1 are evaluated in time for a model system. The energy gaps are chosen to be $E_{d_1} - E_{d_2} = 100$ eV and $E_{d_2} - E_f = 10$ eV. Accordingly, the two emitted electrons are distinguishable by their kinetic energies. Furthermore, the two widths are chosen for the sake of the discussion such that the first decay process is faster than the second one, i.e. decay widths Γ_{d_1} and Γ_{d_2} are chosen as 300 and 30 meV, respectively.

The population of state d_1, decreasing with time, is plotted in Fig. 5.2 panel (a). As we have explained, its lifetime $1/\Gamma_{d_1}$ is around 2.2 fs and the state d_1 is effectively depopulated within 20 fs. In contrast, the time-resolved electron spectrum $\sigma_{e_1}(E_{e_1}, t)$, computed via Eq. (5.10), surprisingly continues to develop its intensity after 20 fs. It finally converges at 140 fs, see Fig. 5.2(b). Since the depopulation of state d_1 and the time-resolved spectrum $\sigma_{e_1}(E_{e_1}, t)$ are both observables of the same decay process, the inconsistency of their development in time question the liability of Eq. (5.10). According to this equation, the time-resolved spectrum is computed via integrating over E_{e_2} of the time-resolve coincidence spectrum. In other words, e_1 can only be detected until the coincidence spectrum shows its intensity. Let us imagine an interesting situation: the state d_1 has a lifetime 1 fs and the state d_2 has a lifetime 1 ms. In this case, the second decay is so slow that it does not even start before the first decay process is completed. For this specific case, electrons e_1 are emitted and detected earlier than one can measure the "coincidence spectrum" Therefore, we conclude that Eq. (5.10) is not the correct time-resolved spectrum $\sigma_{e_1}(E_{e_1}, t)$.

If the time-resolved spectrum of e_1 is desired, one should collect all the probabilities of producing e_1 with kinetic energy E_{e_1}. In fact, Eq. (5.11) is then obtained via operating the operator $\hat{O}$ with the total wave function ansatz. This operator reads

$$\hat{O} = |\Phi_{d_2}, E_{e_1}\rangle\langle\Phi_{d_2}, E_{e_1}| + \int \mathrm{d}E_{e_2}|\Phi_f, E_{e_1}, E_{e_2}\rangle\langle\Phi_f, E_{e_1}, E_{e_2}| \; . \tag{5.15}$$

Therefore, a proper time-resolved spectrum of e_1 naturally also involves the time-dependent amplitude of state d_2. For example, if there is no second decay, $\sigma_{e_1}(E_{e_1}, t)$ reads $|a_{d_2}(E_{e_1}, t)|^2$. When there is a second decay, the population $|a_{d_2}(E_{e_1}, t)|^2$ leaks to the next state, i.e. to the final state f. Thus, one simply adds the leaking part back to $|a_{d_2}(E_{e_1}, t)|^2$ and the time-resolved spectrum of e_1 is as given in Eq. (5.11). In addition, all the population of d_2 decays to the final state f after some time, namely

$$\lim_{t\to\infty} |a_{d_2}(E_{e_1}, t)|^2 = 0 \; ,$$

and the usual non-time-resolved spectrum $\sigma_{e_1}(E_{e_1})$ is then determined by the coincidence spectrum under the limit $t \to \infty$, i.e. Eq. (5.7).

After these theoretical discussions, the same numerical example as used in Fig. 5.2 is employed again to demonstrate that the depopulation time of state d_1 is absolutely consistent with the time-scale of the development of $\sigma_{e_1}(E_{e_1}, t)$, via Eq. (5.11). Fig.5.3(a) depicts the time-resolved spectrum $\sigma_{e_1}(E_{e_1}, t)$, evaluated via Eq.(5.11) as well as the electron spectrum, calculated based on Eq. (5.7). The time-resolved spectrum shows its intensity after 4 fs and continuously develops until it finally converges, i.e. coincides with the black curve, at 20 fs. This time scale agrees perfectly with the state d_1's depopulation time. More interestingly, the partial contributions to $\sigma_{e_1}(E_{e_1}, t)$, namely $|a_{d_2}(E_{e_1}, t)|^2$ and $\int \mathrm{d}E_{e_2}|a_f(E_{e_1}, E_{e_2}, t)|^2$, continue to vary after 20 fs, in spite of the convergence of $\sigma_{e_1}(E_{e_1}, t)$. The population of the state d_2, shown in Fig. (5.3)(b), grows until 15 fs and then decreases slowly with time due to the second decay process. Eventually all the population of the state d_2 disappears. The part $\int \mathrm{d}E_{e_2}|a_f(E_{e_1}, E_{e_2}, t)|^2$, in contrast with $|a_{d_2}(E_{e_1}, t)|^2$, shows its intensity after 20 fs and becomes dominant contribution to the spectrum after a long time.

Studying the depopulation time of the state d_1 leads us to an exciting understanding of the time-resolved spectrum $\sigma_{e_1}(E_{e_1}, t)$, given by Eq. (5.11). Unfortunately, evaluating

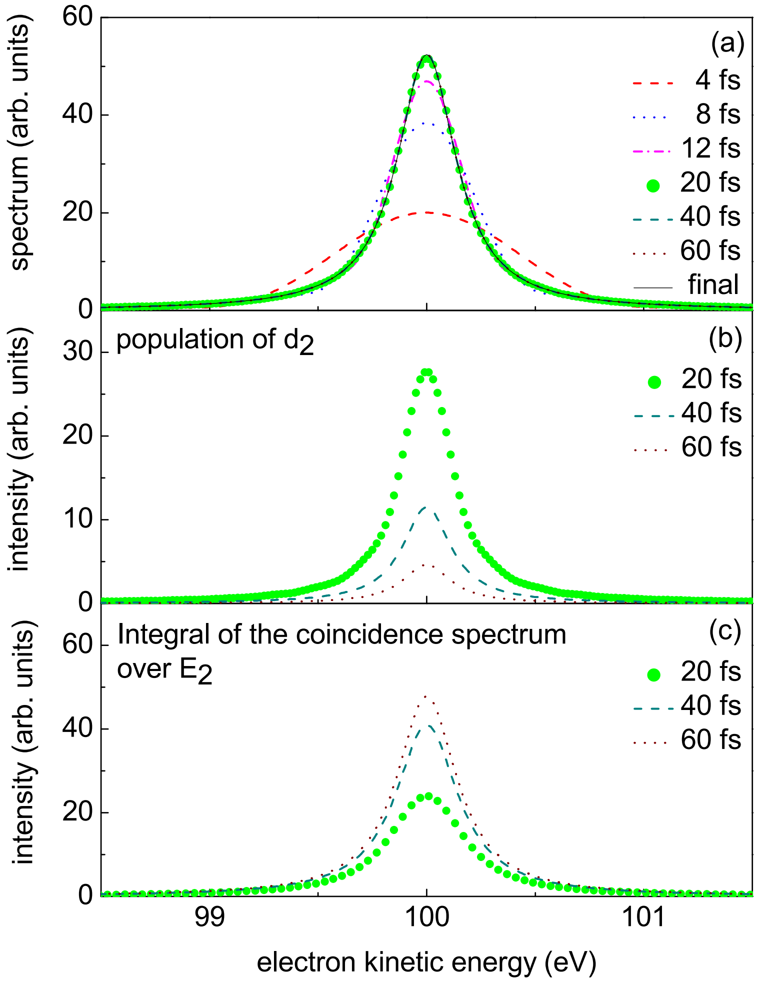

Figure 5.3: Time-resolved electron spectrum $\sigma_1(E_1, t)$ in an cascade process and the breakdown into its contributions. Panel (a) shows the time-resolved electron spectrum $\sigma_1(E_1, t)$, evaluated by Eq. (5.11). The usual spectrum (not time-resolved), evaluated via Eq. 5.11, is also shown as a black curve. As expected, the time-resolved spectrum indeed converges after 20 fs, cf. the green filled circles and the black curve. Panel(b) shows how the population of state d_2, $|a_{d_2}(E_1, t)|^2$, decreases in time. After the second decay process is completed, there is no contribution from $|a_{d_2}(E_1, t)|^2$ to the time-resolved spectrum $\sigma_1(E_1, t)$. Panel (c) shows the "leak" of $|a_{d_2}(E_1, t)|^2$, which is calculated via $\int \mathrm{d}E_2 |a_f(E_1, E_2, t)|^2$. Its intensity gets stronger over time and exactly compensates for the leaking intensity from $|a_{d_2}(E_1, t)|^2$ so that $\sigma_1(E_1, t)$ stays the same after 20 fs. The parameters used are the same as in Fig. 5.2.

the time-resolved spectrum of e_1 by Eq. (5.11) is rather cumbersome in practice due to the integration over all electron energy, i.e. $\int \mathrm{d}E_{e_2}|a_f(E_{e_1}, E_{e_2}, t)|^2$. This term represents the population of the final state with all possible E_{e_2} and can be evaluated more efficiently by

$$\begin{aligned}
&\int \mathrm{d}E_{e_2}|a_f(E_{e_1}, E_{e_2}, t)|^2 \\
&= \int \mathrm{d}E_{e_2} \int_0^t \mathrm{d}t' \int_0^t \mathrm{d}t'' a^*_{d_2}(E_{e_1}, t') W^*_{d_2\to f} e^{-i(E_f+E_{e_1}+E_{e_2})(t'-t)} e^{i(E_f+E_{e_1}+E_{e_2})(t''-t)} W_{d_2\to f} a_{d_2}(E_{e_1}, t'') \\
&= \int_0^t \mathrm{d}t' \int_0^t \mathrm{d}t'' a^*_{d_2}(E_{e_1}, t') W^*_{d_2\to f} e^{iE_{e_1}(t''-t')} \times 2\pi\delta(t''-t') W_{d_2\to f} a_{d_2}(E_{e_1}, t'') \\
&= \int_0^t \mathrm{d}t' 2\pi |W_{d_2\to f}|^2 |a_{d_2}(t')|^2 = \int_0^t \mathrm{d}t' \Gamma_{d_2} |a_{d_2}(t')|^2 \,. \qquad (5.16)
\end{aligned}$$

This equation shows that the population of the final state with the emitted electron e_2 is equal to the accumulated loss of the d_2 population due to the presence of the second decay. Note that we have used the relation $\Gamma_{d_2} = 2\pi|W_{d_2\to f}|^2$ in the derivation. In consequence, Eq. (5.11) can be reformulated as

$$\sigma_{e_1}(E_{e_1}, t) = |a_{d_2}(E_{e_1}, t)|^2 + \int_0^t \mathrm{d}t' \, \Gamma_{d_2} \, |a_{d_2}(E_{e_1}, t)|^2 \,. \qquad (5.17)$$

According to Eq. (5.17), $a_f(E_{e_1}, E_{e_2}, t)$ is not required for computing $\sigma_{e_1}(E_{e_1}, t)$. This equation is numerically more efficient for evaluating the electron spectrum of e_1 than Eq. (5.11), especially when there are many final states. It has been adapted to the ICD following the Ne 1s Auger process for evaluating the time-resolved Auger spectrum, see Eq. (4.10).

5.3 Coincidence Spectra and Time-Resolved Coincidence Spectra

The interrelation between two decay widths, Γ_{d_1} and Γ_{d_2}, can be obtained by analyzing the coincidence spectrum of e_1 and e_2. To visualize the influence of the decay widths on the coincidence spectrum, we evaluate the spectrum in three different situations. Using the order of magnitude of a decay width Γ as $\mathcal{O}(\Gamma)$, we choose the first case as $\mathcal{O}(\Gamma_{d_1}) > \mathcal{O}(\Gamma_{d_2})$, i.e. Γ_{d_1} and Γ_{d_2} are chosen as 300 meV and 30 meV, respectively. The intermediate case is $\mathcal{O}(\Gamma_{d_1}) \simeq \mathcal{O}(\Gamma_{d_2})$, i.e.$\Gamma_{d_1}$ and Γ_{d_2} are chosen as 200 meV and 100 meV, respectively. The last case and also the most interesting one is $\mathcal{O}(\Gamma_{d_1}) < \mathcal{O}(\Gamma_{d_2})$. The latter is closely related to a situation that two electrons are emitted simultaneously, namely a double Auger process. Γ_{d_1} and Γ_{d_2} are chosen, respectively, to be 30 meV and 300 meV in this case. Relative energy gaps are still the same as used previously.

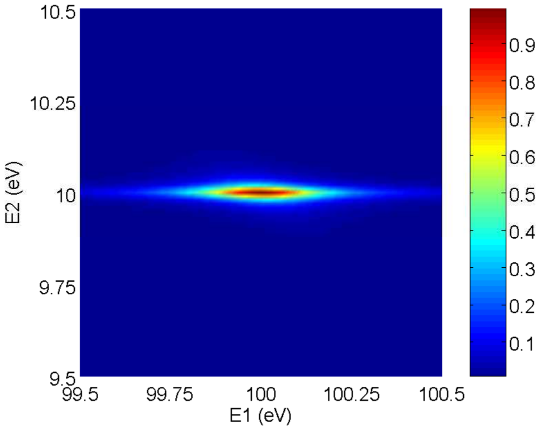

Figure 5.4: Coincidence spectrum of e_1 and e_2 of the first case of the cascade decay process. Shown is the spectrum by the relative intensity, which is provided by the color scale on the right-hand-side of the figure. Coordinates are the energies of two emitted electron, namely E_{e_1} and E_{e_2}. The very large Γ_{d_1} (300 meV) results in a broad energy distribution of E_{e_1}, while the small Γ_{d_2} (30 meV) allows only very little energy distribution of E_{e_2}.

The coincidence spectrum of the first case, calculated via Eq. (5.6) is depicted in Fig.5.4. The spectrum, which centers at the electron kinetic energies $(E_{e_1}, E_{e_2}) = (100\text{ eV}, 10\text{ eV})$, appears like a horizontal stripe. The energy distribution of E_{e_1} is much broader than the distribution of E_{e_2} because Γ_{d_1} (300 meV) is much larger than Γ_{d_2} (30 meV). In consequence, integrating the coincidence spectrum over E_{e_2} yields $\sigma_{e_1}(E_{e_1})$ of a large FWHM in comparison with $\sigma_{e_2}(E_{e_2})$, which is available by integrating the coincidence spectrum over E_{e_1}. The reader may wonder why the coincidence spectrum shown in Fig. 5.4 does not lie on the diagonal of the plot as usually reported in literatures and explained by energy conservation [20]. The answer will be revealed while we introduce the third situation, namely $\mathcal{O}(\Gamma_{d_1}) < \mathcal{O}(\Gamma_{d_2})$.

By choosing Γ_{d_1} and Γ_{d_2} of the same order of magnitude, i.e. the former is 200 meV and the latter is 100 meV, we evaluate the coincidence spectrum for the intermediate case. In contrast to Fig. 5.4, the coincidence spectrum in this case, shown in Fig. 5.5, allows a broad distribution of E_{e_2}. In fact, the spectrum shown in Fig. 5.5 has broad energy distributions for both electrons, and in consequence, the coincidence spectrum appears as a spot located at $(E_{e_1}, E_{e_2}) = (100\text{ eV}, 10\text{ eV})$. For an atomic level system, the shape of the (e_1,e_2) coincidence spectrum is essentially determined by the ratio $\Gamma_{d_1}/\Gamma_{d_2}$. For example, keeping the ratio as 2 and varying the value of both widths changes the size of the spot but never turns the shape into a stripe. More important, the (e_1,e_2) coincidence spectra of the three cases currently under discussion have different shapes (styles). Studying the (e_1,e_2) coincidence spectrum allows to understand the interrelation between the two decay widths.

Last but not least, Γ_{d_1} and Γ_{d_2} are chosen to be 30 and 300 meV, respectively. In this

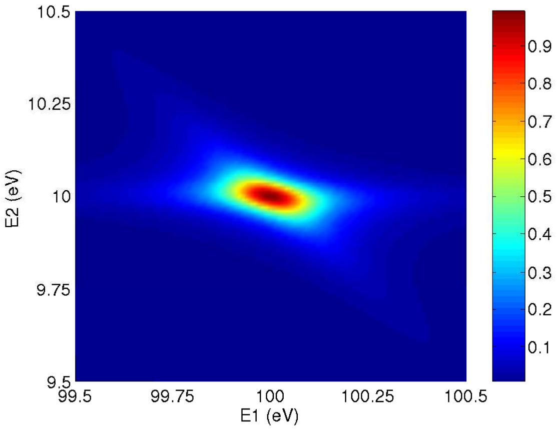

Figure 5.5: Coincidence spectrum of e_1 and e_2 of the second case. Shown is the spectrum by the relative intensity as a function of E_{e_1} and E_{e_2}. Due to the large Γ_{d_1} (200 meV) and Γ_{d_2} (100 meV), both e_1 and e_2 have a broad energy distribution. Hence the coincidence spectrum looks like a spot.

case the coincidence spectrum, shown in Fig. 5.6, appears continuously only on the diagonal of the plot. This feature is often explained by an over-simplified rule, namely the energy conservation, which is not precise enough to explain why the previous two coincidence spectra do not lie on the diagonal of the plot. The real reason of the coincidence spectrum appearing on the diagonal is that the two electrons share the energy within an energy range, i.e. the range of Γ_{d_2}.

As shown in Eq. (5.12), the spectrum of e_1 has a FWHM $\Gamma_{d_1} + \Gamma_{d_2}$, meaning that the energy distribution of e_1 results from the energy uncertainty of state d_1 and state d_2. On the other hand, the energy distribution of e_2 comes only from the energy uncertainty of state d_2, see Eq. (5.13). In short, the energy uncertainty of d_2 are shared by e_1 and e_2. Interestingly, this energy sharing between two electrons becomes extremely pronounced when Γ_{d_2} is much larger than Γ_{d_1}. For example, even when the width Γ_{d_1} is very small, the emitted e_1 can have an energy $E_{d_1} - E_{d_2} + \Delta E$, while the emitted e_2 has an energy $E_{d_2} - E_f - \Delta E$, as long as $|\Delta E|$ is within the energy uncertainty range allowed by d_2. In consequence, the (e_1,e_2) coincidence spectrum lies on the diagonal as we saw in Fig. 5.6. Additionally, the finite lifetime of d_1 broadens the spectrum so that it appears as a diagonal stripe[3]. In conclusion, the coincidence spectrum lies on the diagonal only when the two particles share the same energy.

Consider an extreme case: when the second decay is so fast that its Γ_{d_2} is comparable with the energy gap between $E_{d_1} - E_{d_2}$. In this case, electrons e_1 and e_2 leave the system simultaneously, and hence the process is no longer a cascade process. Such a process has been identified as a double Auger process [63, 64], which results from purely electron correlation. Interestingly, the two emitted electrons continuously share

---

[3] Note that the energy of d_1 actually is uncertain due to its finite lifetime. Therefore, even under the energy conservation, the spectrum still have an energy distribution.

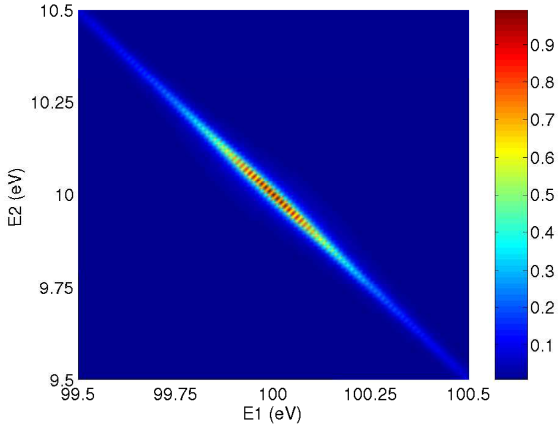

Figure 5.6: Coincidence spectrum of the third case. Used Γ_{d_1} and Γ_{d_2} are 30 meV and 300 meV, respectively. The spectrum appears on the diagonal due to the two electrons sharing the energy $E_{d_1} - E_f$ within the energy range which is allowed by the uncertainty Γ_{d_2}.

the energy so that the coincidence spectrum of a double Auger process again appears on the diagonal [64]. The similarity between the double Auger process and an extreme cascade case still requires further studies. Here we will only stress that *the coincidence spectrum lying on the diagonal shows that the two particles, e.g. two electrons, share the same energy (or energy uncertainty).* If the two particles do not share the same energy, the energy conservation only restricts the center of a coincidence spectrum and cannot determine its shape.

The time-resolved version of Fig. 5.6 is shown in Fig. 5.7. The spectrum has a broader energy distribution in the beginning of the decay process, e.g. 10 fs. Later, the distribution becomes more concentrate on the diagonal when the time increases. This effect is often understood by the time-energy uncertainty principle [61]. However, this reason is also not correct since the final electronic state is stationary. In fact, this is an interference effect [26] (see Sec. 6.4). If one waits long enough, the coincidence spectrum is finally uniquely determined by the decay widths and the energies of the states participating in the cascade process.

5.4 Summary

A simple atomic level system has been employed to study a two step cascade decay process in the time-dependent approach. The major achievement has been to derive the correct time-resolved spectrum for a cascade decay process, i.e. the time-resolved electron spectrum of e_1, which is given by the probability decaying to state d_2 and all its leakages (due to the presence of the second decay). The leakage can be evaluated

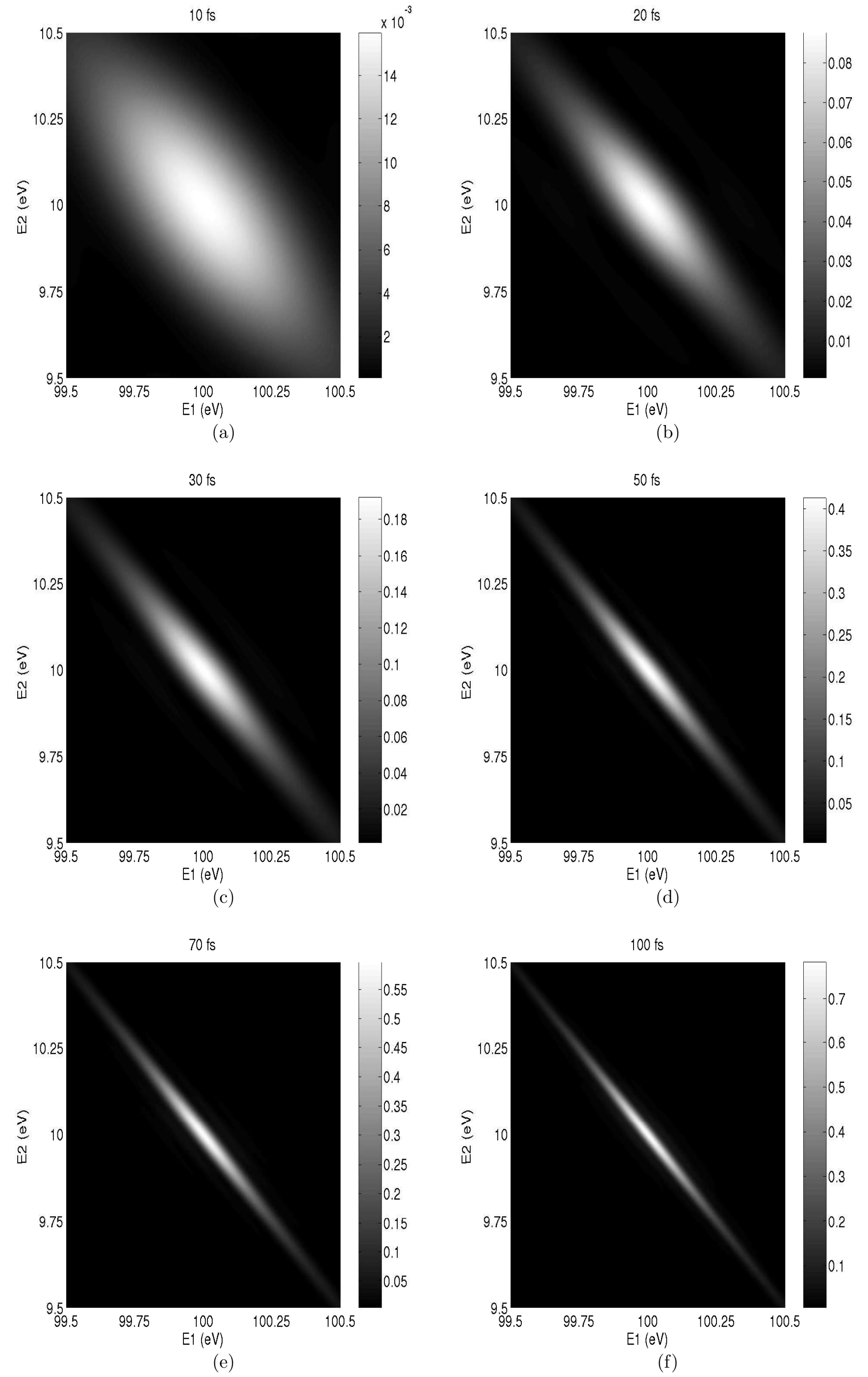

(a) (b) (c) (d) (e) (f)

Figure 5.7: Top view of the time-resolved coincidence spectrum. The energy distribution of the spectrum becomes narrower over time; this effect is an interference of wave functions accumulated trough time.

by collecting all probability of producing e_2 or by collecting the accumulated loss of d_2 population through time. The theory can be easily adapted for a diatomic system and provides a way to evaluate the Auger electron spectrum of the ICD following Auger process. Furthermore, the coincidence spectra of three different cases have been investigated. Results show that the interrelation between two decay widths can be obtained by the shape of the coincidence spectrum. More important, it is found that only when the two particles share the same energy, the spectrum lies on the diagonal. This explanation also applies to the coincidence spectrum of a double Auger process, showing that the rule is more general than a cascade decay process. We have also noticed that the finite lifetimes of the intermediate states broadens a coincidence spectrum.

Chapter 6

Interrelation between the Distribution of Kinetic Energy Release and Emitted Electron Energy following the Decay of Electronic States

In Chapter 4 we have compared our numerical ICD electron spectrum with the experimental kinetic energy release (KER) spectrum through a mirror imaging procedure. This empirical procedure is required due to two reasons: (i) the KER energy distribution is often much better resolved than the electron kinetic energy distribution and (ii) the reported direct numerical simulation of the KER spectrum is too expensive [9, 13, 24]. Fortunately, the electron spectrum and the KER spectrum were found to be mirror image to each other for the ICD process of Ne_2 [8, 10] and has been successfully applied for comparison between numerical ICD electron spectrum and the experimental KER spectrum in other ICD processes [12, 57]. Why is this empirical mirror image principle so successful in obtaining the KER spectrum from the corresponding electron spectrum? A straightforward explanation is the law of energy conservation *under a classical picture* [8, 10].

In this chapter, we shall explain in detail how to obtain the empirical mirror image principle *under a classical picture* and the problem of applying the classical picture to a quantum system. The quantum expression, which allows to evaluate the KER spectrum more efficiently than the method reported before [9, 24, 65], will be derived. This new expression of the KER spectrum sheds light on the underlying physics of the kinetic energy release in a fragmentation process [66, 67].

6.1 The Mirror Image Principle

The KER energy is the translational kinetic energy, which all ionic fragments obtained from a dissociation process [68]. The KER distribution can be precisely measured due to advances in time-of-flight mass spectroscopy [69, 70] and has become one of the most important quantities to study dissociation processes [68]. Naturally, the KER distribution is also studied in an ICD process [5–8, 13] as well as in the dissociation after molecular Auger decay [18, 20]. Both processes belong to the same fragmentation category, namely the fragmentation following electron emission [67]. In these two cases, one can measure the kinetic energy distribution of the emitted Auger/ICD electron (electron spectrum) and the KER distribution (KER spectrum) [8, 18–20].

In spite of belonging to the same fragmentation category, there are some differences between the ICD process in a noble gas dimer and the molecular Auger decay followed by dissociation. The former produces two ions, which then immediately undergo Coulomb explosion since the dimer is weakly bound [6, 8, 13]. The mirror image principle is often confirmed for a diatomic ICD process between the ICD electron spectrum and its corresponding KER distribution [8, 10, 66]. On the other hand, a doubly ionized state, produced by the molecular Auger decay, can be repulsive, but sometimes the molecular bond is strong enough to overcome the Coulomb repulsion, and a temporarily bound final state, namely a resonance, is formed [18, 20]. More importantly, there is hardly any mirror image principle ever being confirmed between an Auger electron spectrum and its corresponding KER distribution. Instead, the two spectra usually differ [18, 19], for instance in: $\mathrm{CO}^+ \to \mathrm{CO}^{2+} + e^-$.

Recalling that the mirror image principle was derived from the law of the energy conservation, then a conflict is immediately raised. Why doesn't the mirror image principle hold for the observations of CO? To answer the question, let us review how the mirror image principle is derived. To keep the physics transparent, a purely repulsive final state CO^{2+} ($^3\Sigma^-$) is taken as an example, but our discussion is also valid for a resonance state, i.e. CO^{2+} (the second $^1\Sigma^+$ state). The potential energy curves are depicted in Fig. 6.1. Potentials of the ground state CO [state i], the intermediate state CO^+ (C $1s^{-1}$) [state d], and the final state CO^{2+} ($^3\Sigma^-$) [state f] are denoted by V_i, V_d, and V_{f_γ}. The asymptotic value of V_{f_γ} at $R \to \infty$ is also shown and labeled as $V_{f_\gamma}^\infty$.

After a $1s$ electron is photoionized from the carbon, the system has a total energy E_T before emitting another electron, see Fig. 6.1. After emitting an electron with kinetic energy E_e, the molecule starts to dissociate, and at the end of the process, all ionic fragments together have the total translational kinetic energy E_{KER} and the final potential energy $V_{f_\gamma}^\infty$ in the asymptotic region[1]. Now, the energy conservation requires $E_T = E_e + E_{\mathrm{KER}} + V_{f_\gamma}^\infty$, giving a one-to-one mapping between E_e and E_{KER}. Under

---

[1] The kinetic energy of the center of mass has been subtracted.

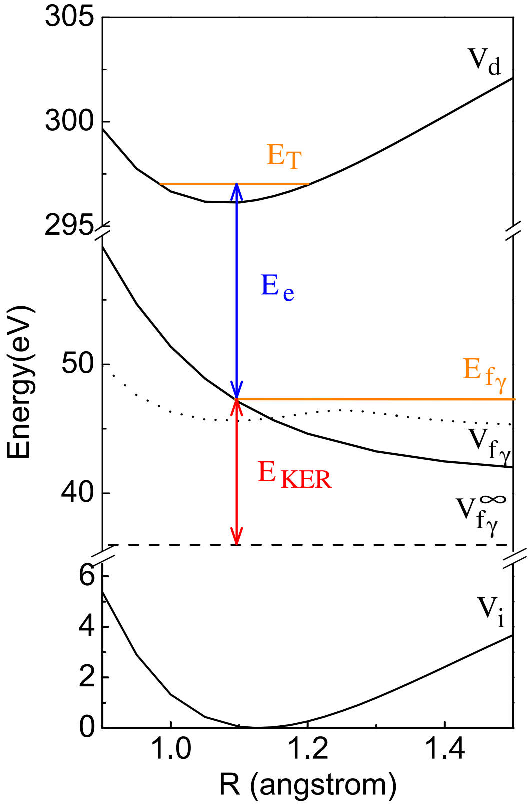

Figure 6.1: Potential energy curves of the molecular Auger process $CO^+(C1s^{-1}) \to CO^{2+}(\,^3\Sigma^-) + e^-$. The internuclear distance is denoted by R. After photoionization, the wave packet is brought to the ionic state d, having a total energy E_T. The wave packet then propagates on potential V_d and gradually decays to the repulsive final state via emitting an electron with kinetic energy E_e and producing the kinetic energy release E_{KER}. Potential curves are taken from Ref. [22, 71]. Additionally, the potential of the resonance state CO^{2+} (the second $^1\Sigma^+$) is also depicted in this figure (dotted curve).

this picture, the probability of measuring the electron with kinetic energy E_e is equal to that of finding all fragments with the KER energy E_{KER}, and therefore, the mirror image principle holds for the electron and KER spectra.

However, the above arguments are based on a classical picture which assumes E_T is constant. It does not take into account the situation where E_T is not uniquely defined, i.e. E_T has an energy distribution of a finite width instead of being a constant. Interestingly, a quantum system very often presents the energy E_T as an energy distribution. For instance, when a molecule or an atom is ionized by a photon of energy well above the ionization threshold, the outgoing photoelectron can carry an arbitrary amount of kinetic energy [22, 72] thus allowing the vibrational levels of the intermediate ionic state d to be populated according to the Franck-Condon principle. Due to the energy distribution of E_T, the mirror image principle breaks down when applied to a pronounced quantum system. In this case, a quantum representation is required in order to simulate the KER spectrum.

6.2 Theory

Equations of Motion

The potential energy curves depicted in Fig. 6.1 provide the essential steps of the fragmentation process following electron emission. In contrast to the previous cascade decay processes, here we concentrate on a single decay process followed by molecular dissociation. Let us review the process again. The molecule initially at the ground state i is photoionized to the ionic intermediate state d. The kinetic energy of the emitted photoelectron is denoted by E_{e_0}. From the state d, the ionic molecule can decay to different repulsive final states f_γ by emitting an electron, having a kinetic energy E_e. Afterwards, the molecule dissociates into ionic fragments, whose total kinetic energy release is denoted by E_{KER}.

The total wave function ansatz for such process reads

$$\begin{aligned} |\Psi(t)\rangle \;=\;& |\psi_i(t)\rangle|\phi_i\rangle + \int \mathrm{d}E_{e_0}\; |\psi_d(E_{e_0},t)\rangle|\phi_d, E_{e_0}\rangle \;+ \\ & \sum_\gamma \iint \mathrm{d}E_{e_0}\;\mathrm{d}E_e\; |\psi_{f_\gamma}(E_{e_0},E_e,t)\rangle|\phi_{f_\gamma}, E_{e_0}, E_e\rangle\;, \end{aligned} \tag{6.1}$$

where $|\phi_\alpha\rangle$ and $|\psi_\alpha\rangle$ denote the electronic and nuclear wave functions of state α, respectively, with $\alpha = i,\ d,\ f$. As before, state d and state f are embedded in the continuum. Their wave functions are hence augmented with the wave function(s) of the outgoing electron(s), see Sec. 2.1. For example, $|\phi_d, E_{e_0}\rangle$ denotes the electronic wave function of the cationic state d augmented with the wave function of the photoelectron with an energy E_{e_0}. The amplitude of this state is then given by $|\psi_d(E_{e_0}, t)\rangle$, which is the nuclear wave function of state d multiplied with the amplitude of finding the photoelectron with an energy E_{e_0}. Similarly $|\phi_{f_\gamma}, E_{e_0}, E_e\rangle$ denotes the electronic wave function of the di-cationic state f augmented with the wave functions of the two outgoing electrons. The corresponding nuclear wave function is denoted by $|\psi_{f_\gamma}(E_{e_0}, E_e, t)\rangle$. Note that all nuclear wave functions also depend on the internuclear distance R.

Removing the trivial term of E_{e_0} via the dressed state method (see Sec. 3.2), we obtain the effective working equations, which read[2]

$$
\begin{aligned}
i|\dot{\psi}_d(t)\rangle &= (\hat{H}_d - \tfrac{i}{2}\Gamma)|\psi_d(t)\rangle && (6.2)\\
i|\dot{\psi}_{f_\gamma}(E_e, t)\rangle &= \hat{W}_{d\to f_\gamma}|\psi_d(t)\rangle + (\hat{H}_{f_\gamma} + E_e)|\psi_{f_\gamma}(E_e, t)\rangle && (6.3)
\end{aligned}
$$

where $\hat{H}_\alpha$ is the nuclear Hamiltonian for state α, and the total decay rate Γ is related to the transition element $\hat{W}_{d\to f_\gamma}$ under the local approximation [26], leading to

$$\Gamma = \sum_\gamma 2\pi|\hat{W}_{d\to f_\gamma}|^2 \ .$$

The wave functions $|\psi_d(t)\rangle$ and $|\psi_{f_\gamma}(E_e, t)\rangle$ are the dressed wave functions and are different from the bare wave functions by only a trivial phase. Finally, the initial wave packet is chosen as the lowest vibrational eigenfunction of the electronic ground state i, namely

$$|\psi_d(0)\rangle = |\chi_i(\nu = 0)\rangle \ .$$

Discrete Continuum Functions

As shown in Fig. 6.1, the potential energy curve of the chosen final state (V_{f_γ}) is purely dissociative. Eigenfunctions of a Hamiltonian containing a dissociative potential are called discrete continuum functions, e.g.

$$\hat{H}_{f_\gamma}|E_{f_\gamma}\rangle = E_{f_\gamma}|E_{f_\gamma}\rangle \ , \tag{6.4}$$

where E_{f_γ} and $|E_{f_\gamma}\rangle$ denote the eigenvalue and the eigenfunction of $\hat{H}_{f_\gamma}$, respectively. The eigenfunctions form a continuum basis set with normalization

$$\langle E_{f_\gamma}|E'_{f_\gamma}\rangle = \delta(E_{f_\gamma} - E'_{f_\gamma}) \ . \tag{6.5}$$

Since the $|E_{f_\gamma}\rangle$ is an eigenfunction of an Hamiltonian, which describes the dissociative nuclear motion, its eigenvalue subtracting the asymptotic potential $V^\infty_{f_\gamma}$ yields the KER

---

[2] The weak field approximation and the broad-band ionization are assumed.

energy E_{KER}, as shown in Fig. 6.1. In other words, subtracting $V_{f_\gamma}^{\infty}|E_{f_\gamma}\rangle$ from both sides of Eq. (6.4) leads to

$$(\hat{H}_{f_\gamma} - V_{f_\gamma}^{\infty})|E_{\text{KER}}\rangle = E_{\text{KER}}|E_{\text{KER}}\rangle \ , \tag{6.6}$$

where the E_{KER} and $|E_{\text{KER}}\rangle$ are given by

$$E_{\text{KER}} = E_{f_\gamma} - V_{f_\gamma}^{\infty} \ , \tag{6.7}$$

$$|E_{\text{KER}}\rangle = |E_{f_\gamma}\rangle \ . \tag{6.8}$$

Eqs. (6.7-6.8) are important. The first one states a one-to-one mapping between E_{KER} and E_{f_γ}; the second one shows that the continuum functions $|E_{\text{KER}}\rangle$ and $|E_{f_\gamma}\rangle$ are identical so that the final state wave packet can be expanded in both functions. Hence the nuclear wave function $|\psi_{f_\gamma}(E_e, t)\rangle$ can be expanded in this basis set as:

$$|\psi_{f_\gamma}(E_e, t)\rangle = \int \mathrm{d}E_{\text{KER}} \, c_{E_{\text{KER}}}(E_e, t)|E_{\text{KER}}\rangle \ . \tag{6.9}$$

Coincidence Spectra

For a fragmentation process following electron emission, the electron and KER distributions can be measured in coincidence, that is, the KER-electron coincidence spectrum. It measures the probability of finding an electron with kinetic energy E_e and the fragmented ions with a total kinetic energy release E_{KER} in coincidence. Define the operator $\hat{P}$ as

$$\hat{P} = |E_{\text{KER}}\rangle\langle E_{\text{KER}}| \otimes |\phi_{f_\gamma}, E_e\rangle\langle\phi_{f_\gamma}, E_e| \ . \tag{6.10}$$

The time-resolved coincidence spectrum of a partial channel γ (with a relative intensity) is obtained as the expectation value of $\hat{P}$:

$$\sigma^{(\gamma)}(E_{\text{KER}}, E_e, t) = \langle\Psi_{\text{tot}}|\hat{P}|\Psi_{\text{tot}}\rangle = |\langle E_{\text{KER}}|\psi_{f_\gamma}(E_e, t)\rangle|^2 = |c_{E_{\text{KER}}}(E_e, t)|^2 \ . \tag{6.11}$$

Note that t is the accumulated time after the ionization pulse and is not related to the time required for measuring the emitted electrons and ions. The usual non time-resolved coincidence spectrum accumulates all results over time, i.e. Eq. (6.11) under the limit $t \to \infty$.

$$\sigma^{(\gamma)}(E_{\text{KER}}, E_e) = \lim_{t\to\infty} |c_{E_{\text{KER}}}(E_e, t)|^2 \tag{6.12}$$

It should be indicated that Eq. (6.11) and Eq. (6.12) are the spectra of a partial channel, i.e. a certain final state f_γ. If the spectrum from all the channels is desired, a summation over all final states (sum over γ) is needed.

KER and Electron Spectra

The time-resolved KER and electron spectra of a partial channel γ are also available from numerical integration of Eq. (6.11) [24]:

$$\sigma_{\mathrm{KER}}^{(\gamma)}(E_{\mathrm{KER}}, t) = \int_0^\infty \mathrm{d}E_e \; \sigma^{(\gamma)}(E_{\mathrm{KER}}, E_e, t) \tag{6.13}$$

$$\sigma_e^{(\gamma)}(E_e, t) = \int_0^\infty \mathrm{d}E_{\mathrm{KER}} \; \sigma^{(\gamma)}(E_{\mathrm{KER}}, E_e, t). \tag{6.14}$$

The strategy to obtain a single spectrum from a coincidence measurement, as shown in Eqs. (6.13-6.14), requires a numerical integration over the coincidence spectrum. Thought the method is simple, it requires a very fine energy mesh to perform a reliable numerical integration. What exacerbates the situation is that the wave packet propagation has to be performed for each energy of the mesh. Hence, this way usually requires an enormous numerical effort to obtain a KER or electron spectrum for comparing with experiment. We mentioned already that the methods reported in Ref. [9, 65] are equivalent to the current method [24] as shown in Ref. [67].

A better way is to carry out these integrations analytically, thus avoiding the evaluation of the coincidence spectrum. The expression of the electron spectrum shown in Eq. (6.14) can be rearranged to a different form by inserting an integral with a Dirac delta function, which is given by the orthonormality shown in Eq. (6.5):

$$\begin{aligned} \sigma_e^{(\gamma)}(E_e, t) &= \int_0^\infty \mathrm{d}E_{\mathrm{KER}} \; |c_{E_{\mathrm{KER}}}(E_e, t)|^2 \\ &= \int_0^\infty \mathrm{d}E_{\mathrm{KER}} \int_0^\infty \mathrm{d}E'_{\mathrm{KER}} \; c^*_{E'_{\mathrm{KER}}}(E_e, t)\langle E'_{\mathrm{KER}}|E_{\mathrm{KER}}\rangle c_{E_{\mathrm{KER}}}(E_e, t) \\ &= \langle \psi_{f_\gamma}(E_e, t)|\psi_{f_\gamma}(E_e, t)\rangle \end{aligned} \tag{6.15}$$

This yields the well-known result for the time-resolved electron spectrum as the final state population [9, 26]. The non-time-resolved electron spectrum is then given by accumulating all results over time, and reads

$$\sigma_e^{(\gamma)}(E_e) = \lim_{t\to\infty} \langle \psi_{f_\gamma}(E_e, t)|\psi_{f_\gamma}(E_e, t)\rangle \; . \tag{6.16}$$

It takes, however, more effort to obtain the equation for the time-resolved KER spectrum. Taking into account that the probability of finding an electron with a negative kinetic energy is zero allows us to lower the bound of Eq. (6.13) to $-\infty$.[3] In addition, from Eqs. (6.3) and (6.9) it follows

$$c_{E_{\mathrm{KER}}}(E_e, t) = -i \int_0^t e^{i(E_{\mathrm{KER}} + V^\infty_{f_\gamma} + E_e)(t'-t)} \langle E_{\mathrm{KER}}|\hat{W}_{d\to f_\gamma}|\psi_d(t')\rangle \, \mathrm{d}t' \; . \tag{6.17}$$

---

[3] If the potential curves V_d and V_{f_γ} are well separated, the coincidence probability is always zero when E_e is negative.

Inserting this expression into Eq. (6.13), we arrive at another form of the time-resolved KER distribution:

$$\begin{aligned}
&\sigma^{(\gamma)}_{\mathrm{KER}}(E_{\mathrm{KER}}, t) \\
&= \int_0^t \mathrm{d}t' \int_0^t \mathrm{d}t'' \int_{-\infty}^{\infty} \mathrm{d}E_e \; e^{i(E_{\mathrm{KER}}+V^{\infty}_{f_\gamma}+E_e)(t''-t')} \; \langle\psi_d(t')|\hat{W}^{\dagger}_{d\to f_\gamma}|E_{\mathrm{KER}}\rangle\langle E_{\mathrm{KER}}|\hat{W}_{d\to f_\gamma}|\psi_d(t'')\rangle \\
&= \int_0^t \mathrm{d}t' \int_0^t \mathrm{d}t'' \; 2\pi\delta(t''-t')\langle\psi_d(t')|\hat{W}^{\dagger}_{d\to f_\gamma}|E_{\mathrm{KER}}\rangle\langle E_{\mathrm{KER}}|\hat{W}_{d\to f_\gamma}|\psi_d(t'')\rangle \\
&= 2\pi \int_0^t \mathrm{d}t' \; |\langle E_{\mathrm{KER}}|\hat{W}_{d\to f_\gamma}|\psi_d(t')\rangle|^2 \; . \qquad (6.18)
\end{aligned}$$

This new formulation provides a vivid physical interpretation of the KER spectrum [66] as an "accumulated" generalized Franck-Condon factor. "Generalized" is in the sense that the usual Franck-Condon factor assumes that $\hat{W}_{d\to f_\gamma}$ is independent of R. This interpretation differs remarkably from the one of the electron spectrum, cf. Eq. (6.15), as the latter depends only on $|\psi_{f_\gamma}\rangle$.

The non-time-resolved KER spectrum is obtained by accumulating the results over time. It reads

$$\sigma^{(\gamma)}_{\mathrm{KER}}(E_{\mathrm{KER}}) = 2\pi \int_0^{\infty} \mathrm{d}t' \; |\langle E_{\mathrm{KER}}|\hat{W}_{d\to f_\gamma}|\psi_d(t')\rangle|^2 \; . \qquad (6.19)$$

When letting $t \to \infty$, our equations are proved [67] to be equivalent to those derived from scattering theory [9, 43]. The expressions for the spectra shown in Eqs. (6.15-6.16) and Eqs. (6.18-6.19) are meant for a single partial channel. Again, if a spectrum over all final states is desired, a summation over γ is required.

As a remark, we mentioned that the time-resolved KER spectrum can also be interpreted as the accumulated amount of the wave packet $|\psi_d(t)\rangle$ mapped onto an eigenfunction of a single final electronic state by the following operator

$$\hat{O}^{(\gamma)}_{\mathrm{KER}} = 2\pi\hat{W}^{\dagger}_{d\to f_\gamma}|E_{\mathrm{KER}}\rangle\langle E_{\mathrm{KER}}|\hat{W}_{d\to f_\gamma} \; . \qquad (6.20)$$

The term $|E_{\mathrm{KER}}\rangle\langle E_{\mathrm{KER}}|$ can be evaluated in a numerical efficient manner with the complex absorbing potential (CAP). A detailed explanation is given in Appendix F. It is important that the mapping is weighted by the transition matrix element between two electronic states. More importantly, Eq. (6.20) can also applied to the usual pump-probe experiments [73, 74] by replacing the transition matrix element by the interaction between a transition dipole moment and the external laser field.

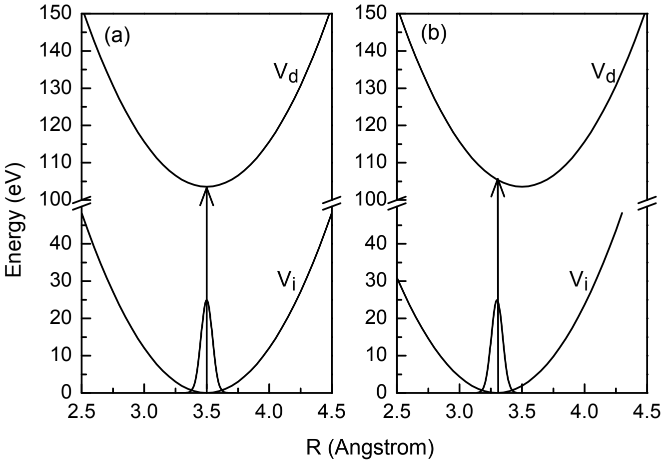

Figure 6.2: The model potentials of V_i and V_d. Panel (a) depicts the case of vertically shifted parabola and panel (b) shows the case of displaced parabola. The mass is chosen to be that of a Ne dimer, but the energy gap between two adjacent vibrational levels is chosen to be 200 meV, which is identical to Γ. The final state potential V_f, although it is not depicted in this figure, is chosen to be $2/R$ (a.u.) with $V_f^\infty = 81.55$ eV. The initial wave packet is always chosen to be the lowest vibrational eigenfunction (a Gaussian) of V_i and is directly placed on potential V_d. In panel (a) this Gaussian function centers at 3.5 Å, in panel (b) at 3.3 Å.

6.3 Understanding the Results: Harmonic Oscillators

To understand the features of a KER spectrum, a single channel model (without index γ) is employed. Namely, there is only one final state f in the current model and its potential is chosen to be Coulomb repulsion ($2/R$ in atomic units). Potentials V_i and V_d are chosen to be those of harmonic oscillators with the same curvature (see Fig. 6.2). They could be centered at the same R, i.e. vertically shifted parabola, or at different R, i.e. displaced parabola. In the former example, only one vibrational level is populated state d after photoionization, while in the latter example, there are many different vibrational levels coherently populated on state d and hence forms a wave packet. The decay rate Γ is chosen to be 200 meV, the same as the energy gap between two adjacent vibrational levels of the potentials, e.g. V_d.

We begin with the example of vertically shifted parabola, where only the lowest vibrational level $|n_d\rangle$ is populated on state d after photoionization. Correspondingly, no nuclear dynamics takes place on V_d, and the intermediate state population simply decays exponentially. What to expect for such a simple case? The KER spectrum shown in Eq. (6.19) can be solved analytically, yielding

$$\sigma_{\mathrm{KER}}(E_{\mathrm{KER}}) = |\langle E_{\mathrm{KER}}|n_d\rangle|^2 \ ,$$

which is the usual Franck-Condon factor [67]. Interestingly, for such a simple case where $|\psi_d\rangle$ is an eigenstate, the KER spectrum does not depend on the decay rate Γ. In other words, the finite lifetime of the intermediate state d does not broaden the KER spectrum. On the other hand, the electron spectrum can also be evaluated analytically, and it yields [67]

$$\begin{aligned}
\sigma_e(E_e) &= \int_{-\infty}^{\infty} \mathrm{d}E' \frac{\Gamma/(2\pi)}{E'^2+\Gamma^2/4} |\langle E_{\mathrm{KER}}|n_d\rangle|^2 \\
&= \int_{-\infty}^{\infty} \mathrm{d}E' \frac{\Gamma/(2\pi)}{E'^2+\Gamma^2/4} \sigma_{\mathrm{KER}}((E_{n_d} - V_f^{\infty}) - (E_e - E')) \\
&= \int_{-\infty}^{\infty} \mathrm{d}E' \frac{\Gamma/(2\pi)}{E'^2+\Gamma^2/4} \sigma_{\mathrm{mKER}}(E_e - E') \ .
\end{aligned}$$

where $E' = E_{\mathrm{KER}} + V_f^{\infty} + E_e - E_{n_d}$ and σ_{mKER} denotes the mirror imaging of KER spectrum. In this case, the electron spectrum is the mirror image of its corresponding KER spectrum and additionally is convoluted with a Lorentzian function with a FWHM of Γ to account for the finite lifetime broadening.

Numerical results for such a simple case are shown in Fig. 6.3 (a). The mirror image of the numerical electron spectrum, computed by Eq. (6.16), is denoted as "predicted KER". Obviously, the exact KER spectrum is narrower and exhibits a nodal structure at its high-energy wing being a fingerprint of the dissociative eigenfunctions of state f. Accordingly we have this KER spectrum convoluted with a Lorentzian of FWHM Γ, and it reproduces exactly the classically predicted KER spectrum.

Shifting the equilibrium distance of V_i to smaller values (3.3 Å), introduces nuclear dynamics of $|\psi_d(t)\rangle$ on the decaying state d. The decay process now becomes more intricate even for a constant Γ and harmonic curves. The electron spectrum exhibits two humps, which are composed by the vibrational progression stemming from many vibrational levels of state d and the discrete continuum functions of state f, see the blue curve in Fig. 6.3 (b). Interestingly, the exact KER spectrum essentially consists of a small and a pronounced sharp peak at low energy and a long high-energy tail, instead of resembling the classically predicted mirror imaging of the electron spectrum. These two peaks are contributed by the decay of $|\psi_d(t)\rangle$ at the classical turning points and was proved by tracing the time-resolved KER spectrum.

As a conclusion in this section, it has been proven that quantum effects can be substantial and break the classical picture. In consequence, the mirror image principle holds only when the populated vibrational levels of state d are quasi-degenerate (as if only one vibrational level is populated) and the decay process is slow so that the finite lifetime broadening is negligible [66, 67]. These conditions are not always fulfilled in an electronic decay process, see Sec. 6.5 for comparison with experiments.

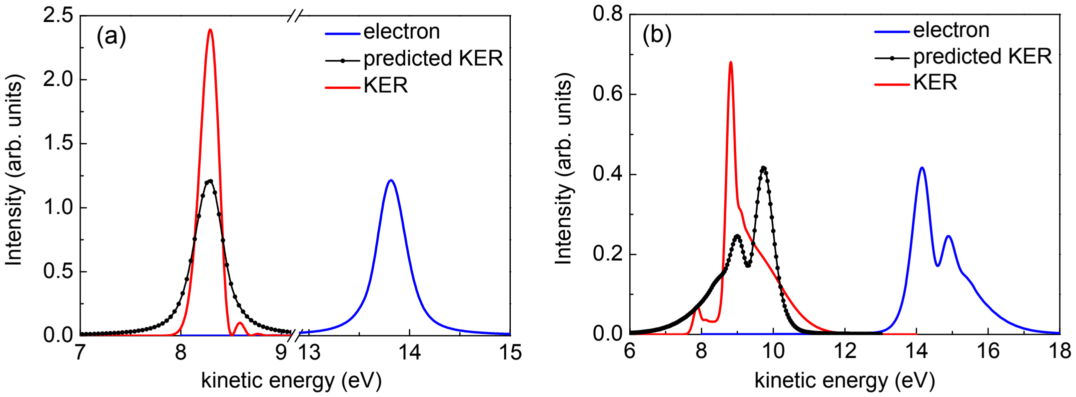

Figure 6.3: The electron and KER spectra of model studies, computed via Eqs. (6.19) and (6.16). The potential energy curves and Γ and are given in Fig. 6.2. The spectra shown in panel (a) and (b) are the result of a vertically shifted parabola and the result of a displaced parabola, respectively. The exact KER spectra (in the left hand side of both panels) in both cases differ remarkably from the classically predicted KER spectra, obtained by mirroring the electron spectra.

6.4 Time-Resolved KER and Electron Spectra

As techniques for measuring the time-resolved spectra are within reach [55, 73, 74], it becomes more and more relevant to investigate how a spectrum develops in time due to those valuable insights (into nuclear dynamics) that a time-resolved spectrum can provide. Naturally, both the KER and electron energy distributions can be used for tracing the molecular motion through measuring the time-resolved spectra. However, as it was already pointed out in Eq. (6.15) and Eq. (6.18), the time-resolved electron spectrum shows the population of the final state f, while the time-resolved KER spectrum measures the accumulated generalized Franck-Condon factor, leading to the information on the nuclear dynamics of the intermediate state d.

In this section, the differences between these two spectra will be illustrated by showing their evolution in time. To proceed, the Auger decay process

$$\mathrm{CO}^{+}(\mathrm{C}\,1s^{-1}) \rightarrow \mathrm{CO}^{2+}(\,^{3}\Sigma^{-}) + e^{-}$$

is chosen as an example. Potential curves of the involved states were already depicted in Fig. 6.1, and the total Auger width is 95 meV for this process [22]. The KER distribution of this channel has been observed in experiment and it was found to be a broad distribution (with low intensity) above 10 eV [19].

The numerical results are presented in Fig. 6.4: Panels (a) and (b) show the time-resolved KER spectrum and the time-resolved electron spectrum, respectively. Both time-resolved spectra finish to develop within 100 fs, and the electron spectrum is

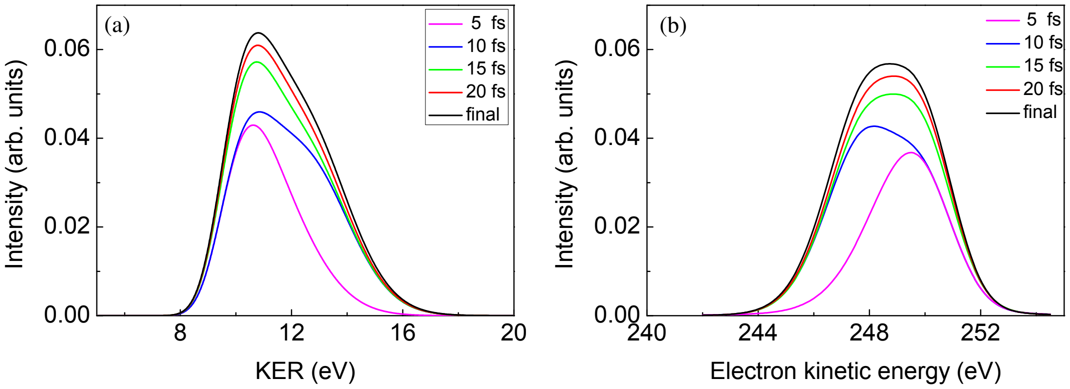

Figure 6.4: Numerical time-resolved KER and electron spectra of channel $\mathrm{CO}^+ \to \mathrm{CO}^{2+}(\,^3\Sigma^-) + e^-$. (a) Time-resolved KER spectrum. It is distributed broadly in energy due to the repulsive potential of the final state. In this case, the peak intensity increases over time until it is converged, i.e. the state CO^+ is completely depopulated. (b) Time-resolved electron spectrum. It is slightly broader than the corresponding KER spectrum. Both spectra converge before 100 fs, and no mirror image relation is found.

slightly broader than the KER spectrum. However, the difference between the two time-resolved spectra is not very pronounced in Fig. 6.4 due to the purely repulsive final state potential. To overcome this problem, we introduce the concept of “finite difference of spectra,” which also allows us to relate the time-evolution of a spectrum to the motion of $|\psi_d(t)\rangle$. The finite difference of spectra is defined as

$$\frac{\Delta\sigma}{\Delta t} = \frac{\sigma(t_2) - \sigma(t_1)}{t_2 - t_1}\ . \tag{6.21}$$

We will set $t_2 = t$ and $t_1 = t - 1\,\mathrm{fs}$, so the finite difference of the time-resolved spectra is merely the difference of the spectra between $t - 1\,\mathrm{fs}$ and t.

For the time-resolved KER spectrum, the finite differences are shown in Fig. 6.5(a). The peak swings back-and-forth in the energy interval from 10 to 13.4 eV, which are contributed from the decay of wave packet $|\psi_d(t)\rangle$ at the classical turning points. The oscillation period of the wave packet motion is also immediately available from the oscillation period shown in Fig. 6.5(a), namely 14 fs. In addition, due to depopulation of the state d, the quadrature (area) of the peak decreases monotonously over time. The peak also continuously spreads wider over the KER energy, which is an evidence for the dispersion of $|\psi_d\rangle$.[4] Overall, measuring the time-resolved KER spectrum allows one to trace the wave packet's motion in the intermediate state.

The differential electron spectrum depicted in Fig. 6.5(b) also indicates the oscillation period of $|\psi_d\rangle$. However, the evolution of the peak in panel (b) is rather non intuitive.

---

[4] The wave packet dispersion is not observable in the current CO case, but it is very pronounced in the ICD following Auger decay in NeAr due to the flat potential curves there.

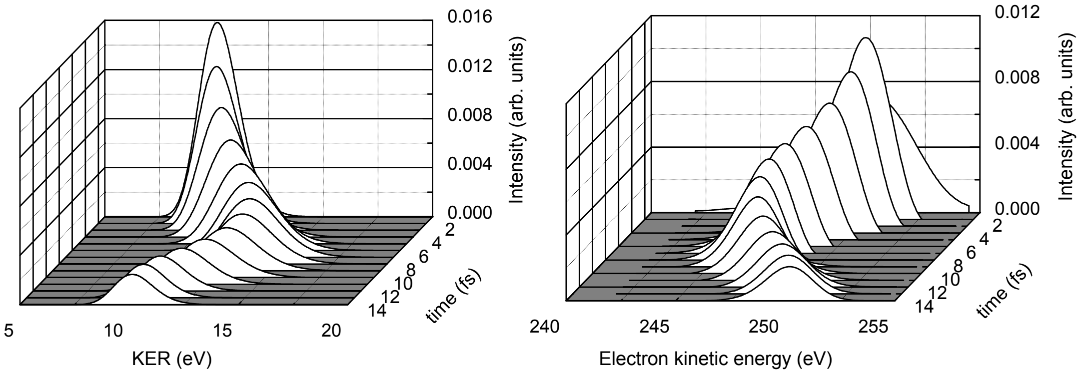

Figure 6.5: Finite difference of the time-resolved KER spectrum, panel (a), and electron spectrum, panel (b), within the first 14 fs. The development of the spectrum in panel (a) can be related to the motion of $|\psi_d(t)\rangle$: the period of oscillation, the depopulation of state d, and the dispersion of the wave packet. Finite difference of time-resolved electron spectrum (b) shows a strange development within the first 2 fs: a broad distribution followed by a narrow distribution. This strange development can be explained by the interference effect (see text and Fig. 6.6), which comes from the final state wave packet.

Take the peak at 1 fs and at 2 fs for example: the peak is very broad in the beginning but then quickly becomes narrow. This strange development is related to the physical meaning of the time-resolved electron spectrum, which is known as the final state population in time [26], see also Eq. (6.15). It is shown in Eq. (6.3) that $|\psi_{f_\gamma}(E_e,t)\rangle$ is generated from $|\psi_d(t)\rangle$ and is then propagated by $\hat{H}_{f_\gamma} + E_e$. Therefore, there is a unique interference between the propagated $|\psi_{f_\gamma}(E_e,t)\rangle$ and the incoming source term $\hat{W}_{d\to f_\gamma}|\psi_d(t)\rangle$. This interference sometimes can lead to the final state's depopulation if the source term has a different phase than the final state wave packet. This phenomenon leaves a trace which becomes more evident if we zoom in to Fig. 6.5(b), see Fig. 6.6. When t increases, the peak moves toward smaller electron energies, and there is a negative tail on the right hand side of the peak. This negative part is caused by a destructive interference, appearing only in the electron spectrum but not in the KER spectrum. In fact, we can take the finite difference of the spectrum to the limit $\Delta t \to 0$, i.e. taking the time derivative of the spectrum. The time-derivative of the KER spectrum yields

$$\frac{\partial}{\partial t}\sigma^{(\gamma)}_{\mathrm{KER}} = 2\pi|\langle E_{\mathrm{KER}}|W_{d\to f_\gamma}|\psi_d(t)\rangle|^2$$

while the electron spectrum gives

$$\frac{\partial}{\partial t}\sigma^{(\gamma)}_{e} = 2\ \mathrm{Im}[\langle\psi_{f_\gamma}(E_e,t)|W_{d\to f_\gamma}|\psi_d(t)\rangle]\ .$$

This shows that a part of the relative phase information can be extracted from the time-derivative electron spectrum, but not from the time-derivative KER spectrum.

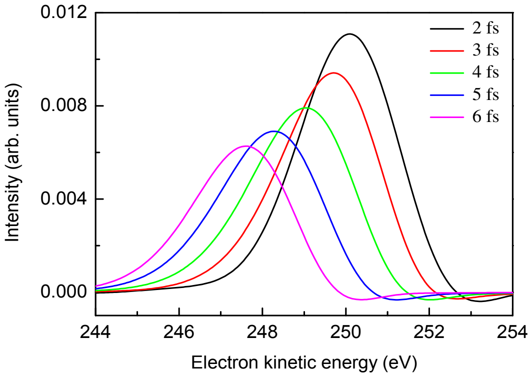

Figure 6.6: Zoom of Fig. 6.5 (b). The peak moves to lower electron energies within 2 to 6 fs, and there is always a negative tail at the right hand side of the peak. This negative value stems from the interference term $2\,\mathrm{Im}[\langle\psi_f(E_e,t)|W_{d\to f}|\psi_d(t)\rangle]$ (see text).

6.5 Electron and KER Spectra of an Auger and an ICD Processes

As already mentioned in Sec. 6.3, the KER spectrum in principle is not the mirror image of the electron spectrum. Only when the finite lifetime broadening is negligible and populated vibrational levels are quasi-degenerate, the mirror image principle holds. Such special case occurs for ICD processes between noble gas dimers but usually not for dissociation following a molecular Auger process.

Let us now compare these two situations, namely a molecular Auger decay and an ICD process. The molecular Auger channel is chosen as $\mathrm{CO}^+(\mathrm{C}\ 1s^{-1}) \rightarrow \mathrm{CO}^{2+}(2\,{}^1\Sigma^+) + e^-$, whose electron and KER spectra have been measured [18, 19]. Potential curves (Fig. 6.1) and Γ (95 meV) are taken from literature [22, 71]. Since the final state is not purely repulsive, there are at least two resonances in the final state $\mathrm{CO}^{2+}(2\,{}^1\Sigma^+)$ [18], i.e. the dotted line in Fig. 6.1. According to Ref. [18], this quasi-bound state then couples to the purely dissociative state $\mathrm{CO}^{2+}({}^3\Sigma^-)$, i.e. the solid curve in Fig. 6.1, which leads to the dissociation limit $\mathrm{C}^+({}^2P) + \mathrm{O}^+({}^4S)$. In principle, the simulation of KER should include this coupling process. On the other hand, it is known that the spin-orbital coupling is not strong in the current process. Hence, we assume that the coupling does not change the local potential but merely shifts the spectrum to a dissociation limit of $\mathrm{C}^+({}^2P) + \mathrm{O}^+({}^4S)$. Under this assumption, the numerical KER spectra can be evaluated again directly by Eq. (6.19) and additionally convoluted with a Gaussian of 0.15 eV FWHM to compare with experiment. The result is depicted by the red-solid curve in Fig. 6.7(a), which agrees surprisingly well with experiment (open circles). The pronounced three peaks in the spectrum were assigned to the three resonance levels of the final state $\mathrm{CO}^{2+}(2\,{}^1\Sigma^+)$ [19]. Different from the KER spectrum, the numerical electron spectrum is essentially a single peak structure (see Fig. 6.7(b) blue curve), due to the fact that the potentials of the intermediate state and the final

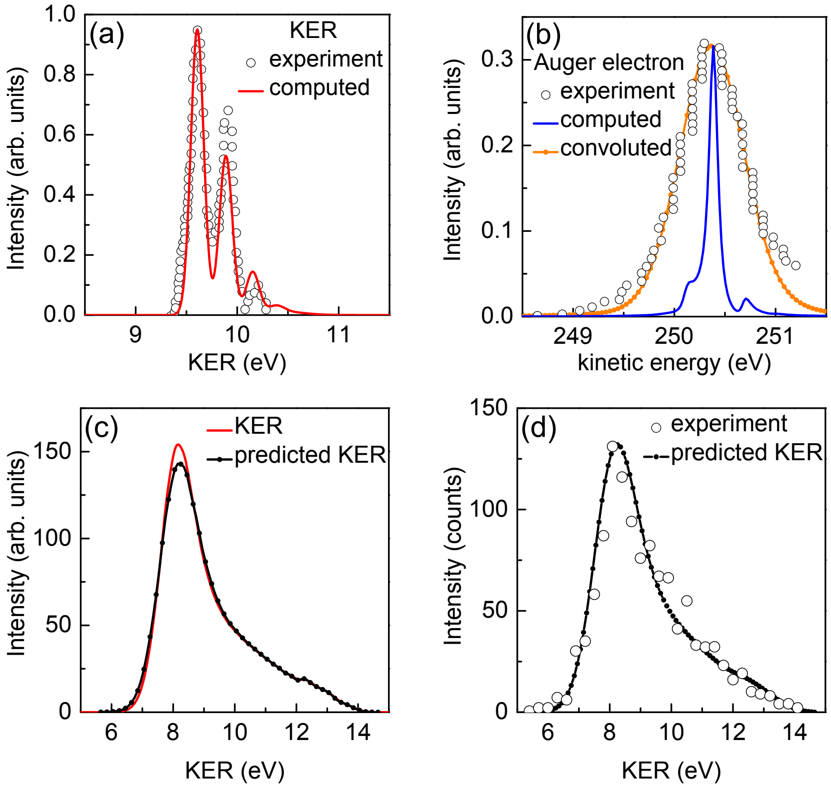

Figure 6.7: Computed and experimental KER and electron spectra for two different processes. Upper panels are spectra of Auger process in CO: $\mathrm{CO}^+ \to \mathrm{CO}^{2+}(2\,^1\Sigma^+) + e^-$. Lower panels are spectra of ICD in NeAr following the K-LL Auger decay of Ne: $\mathrm{Ne}^{2+}(2s^{-1}2p^{-1}\,^1P)\mathrm{Ar} \to \mathrm{Ne}^{2+}(2p^{-2}\,^1D)\text{-}\mathrm{Ar}^+(3p^{-1}) + e^-$. (a) Auger KER spectra. The experimental result is taken from Ref. [19], and the computed KER spectrum (red curve) is convoluted with a Gaussian of 0.15 eV FWHM in order to compare with the experiment. (b) Auger electron spectra. The experimental result is taken from Ref. [18]. The numerical result is calculated by using Eq. (6.16) (blue curve) and additionally convoluted with a Gaussian of 0.68 eV FWHM to account for the experimental resolution (orange curve). Clearly, the electron and KER spectra are far from being the mirror image of each other. (c) ICD KER spectra. Shown are the KER spectrum calculated via Eq. (6.19) (red curve) and the mirror imaged ICD electron spectrum, evaluated by Eq. (6.16), to provide the predicted KER spectrum (black curve). In this example the prediction of classical theory works very well and the electron and KER spectra are the mirror image of each other. (d) The experimental KER spectrum [57] is compared with the predicted KER spectrum, obtained by convoluting the black curve in panel (c) with the experimental resolution 0.7 eV FWHM [57].

state are almost parallel in the Franck-Condon region. This numerical spectrum then is convoluted with a Gaussian resolution function, and the outcome agrees well with the experiment [18]. Regardless of the experimental resolution, it is obvious from these calculations that the KER and Auger electron spectra are far from being the mirror image of each other as expected classically.

Contrary to the molecular Auger process, the electron and KER spectra obtained for the ICD processes in noble gas dimers are usually considered to be the mirror images of each other. The ICD process of interest is, of course, the ICD channel 1. Namely, $\mathrm{Ne}^{2+}(2s^{-1}2p^{-1}\,{}^1P)\mathrm{Ar} \rightarrow \mathrm{Ne}^{2+}(2p^{-2}\,{}^1D)\text{-}\mathrm{Ar}^{+}(3p^{-1})+\ e^{-}$ following the Auger decay of $\mathrm{Ne}^{+}(1\mathrm{s}^{-1})$, which were discussed in Ch. 3 and Ch. 4 . With the plausible fast Auger decay assumption and the value of Γ suggested in Ref. [57], the computed KER spectrum shown in Fig. 6.7 (c) agrees well with the predicted KER spectrum, which is the mirror image of the numerical electron spectrum. This agreement is due to the facts that the potential V_d is very shallow and the rate Γ is rather small. Consequently, several quasi-degenerate vibrational levels of V_d are initially populated, and the system behaves as if a single effective level is populated. A comparison with the experiment is provided in Fig. 6.7(d).

6.6 Summary

For decay processes where electrons are emitted and molecular fragmentation occurs, the fully time-dependent approach for calculating the (time-resolved) KER spectrum is discussed in detail. A numerically efficient expression for obtaining the (time-resolved) KER spectrum is derived. It has a vivid physical interpretation: the spectrum is given by the accumulated generalized Franck-Condon factor [66, 67]. On the other hand, the time-resolved electron spectrum is known from the final state population [26]. The two spectra have different physical interpretations and it can be shown that they are not the mirror image of each other in systems with pronounced quantum effects, e.g. the Auger decay followed by molecular fragmentation in CO [18, 19]. The empirical mirror image principle holds for the two spectra of a diatomic system only if the populated levels of d are quasi-degenerate and the decay width is rather small, e.g. ICD [8] or ICD after Auger [11, 57].

Additionally, the time-resolved KER and electron spectra are compared. It is found that they are rather similar, due to the repulsive final state potential. Consequently, a method for comparing the time development of these spectra is proposed, namely evaluating the change of the time-resolved spectrum during a small but finite time interval. It is found that such a "finite differences spectrum" can provide valuable insight into the nuclear dynamics, especially for the wave packet motion of $|\psi_d(t)\rangle$.

Chapter 7

Resonant Auger Processes in Intense X-Ray Laser Fields

When a core electron of an atom (or molecule) is excited by an external laser field, the core excited atom can relax via electron emission, that is, a resonant Auger process [3, 21, 26, 75–82]. It is known that the energy spectrum of an electron emitted in such a resonant Auger process depends very much on the incident photon energy and bandwidth. For example, a well-known feature, termed *Auger resonant Raman effect* (ARRE), has been observed: the emitted electron energy becomes a function of the detuned photon energy of the exciting radiation [3], and a narrow photon bandwidth causes an Auger line width narrower than the natural decay width [75]. These experiments [3, 21, 26, 75–82] were performed with laser intensities that can be treated within the usual perturbative regime.

In this chapter, we will leave this perturbative regime and discuss what will happen when an intense laser pulse interacts with a molecule. Interest in this topic originated mainly due to the availability of the 4th generation X-ray free-electron lasers (FELs) [83–85]. These new light sources provide a peak brilliance of up to 10^9 times higher than the current synchrotron radiation. For example, a pulse intensity of 10^{18} W/cm^2 is reported in Ref. [86]. The interaction between an atom (or a molecule) and such an intense pulse is nonlinear, and consequently the first order time-dependent perturbation theory, i.e. the Fermi's golden rule, is no longer suitable for such a strong interaction. In this case, it has been proposed theoretically [52] that the resonant Auger process from the Ne ground state to Ne ($1s^{-1}3p$) starts undergoing Rabi oscillation at high X-ray intensity. Interesting phenomena have been found like the appearance of multipeak Auger spectra [52, 87] and the interference effect due to the direct photoionization [88].

Pursuing this example, we will first extend this idea to diatomic molecules which undergo resonant Auger decay under an intensive and coherent laser pulse. The diatomic molecule HCl is chosen as an illustrative example due to the simple structure of its spectrum, and the idea of light-induced strong non-adiabatic effects for diatomic molecules [34, 89] will be explained in detail. Then, the influence of direct photoionization, which is not included in Ref. [34], will be investigated at the end of this chapter.

Before we begin, there is one more issue regarding the experiments with the 4th generation FELs. The pulses [83–85] built based on the so-called self-amplified spontaneous emission (SASE) are found to be completely chaotic, namely each pulse is full of random spikes with random amplitudes [90]. In addition, the X-ray pulse will be reshaped during the propagation through a resonant medium [40, 91]. For such a chaotic pulse, Nina Rohringer and Robin Santra proposed two different ways to perform an experiment [90]. On one hand, there is a single-shot experiment, i.e. one performs only once the experiment and tries to understand the result based on every detail of the specific pulse used in that experiment. On the other hand, one can perform many times the same experiment and build up a statistical description. The second approach is extremely useful if one only knows that the statistically averaged pulse envelope is a Gaussian function but has no details on any single pulse. In addition, two kinds of numerical simulations were also reported in Ref. [90]. One is an ensemble averaged result, calculated via many random pulses. The other is a single simulation result, calculated from an averaged pulse envelope, which is a Gaussian function. It is shown in Ref. [90] that a calculation[1] via the averaged pulse envelope, i.e. no spikes, is sufficient to describe the interaction between atoms and FEL pulses based on SASE. Due to the chaotic behavior, experiments and calculations become more cumbersome as described in Ref. [90]. In order to stabilize the pulse, work is under way for building FEL pulses by a "seeding" procedure [92]. Such a pulse will provide a coherent light source without spikes and allows one to concentrate on the physics of a single molecule interacting with a coherent, smooth pulse. In the following discussion, we will also consider a single molecule interacting with a coherent, smooth FEL pulse.

7.1 The HCl System

Among all the studies of resonant Auger processes, the molecule HCl has attracted a lot of attention [25, 93–98] due to its unique dissociative intermediate states, e.g. HCl($2p_{3/2}^{-1}\sigma^*$). In this case, the intermediate state d, viz. HCl($2p_{3/2}^{-1}\sigma^*$), undergoes both electron emission and molecular fragmentation due to its repulsive potential curves, see Fig. 7.1. The competition between fragmentation and electron emission results in a simple structure of the resonant Auger electron spectrum. Namely, the Auger electron spectrum can be separated into the molecular background, which comes from the Auger decay before dissociation, and a unique atomic peak, which comes from the electron

---

[1] except for the populations of core-hole states

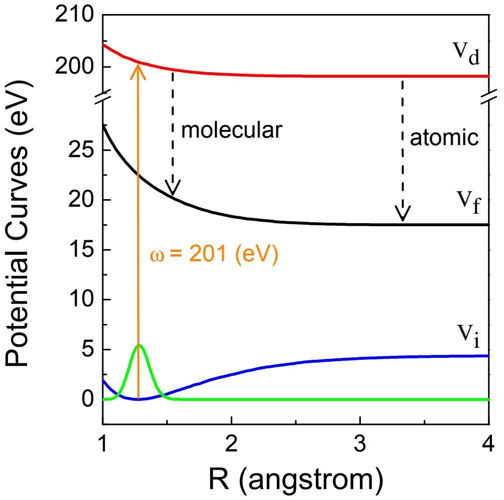

Figure 7.1: Potential curves of the resonant Auger process HCl (ground state) → HCl($2p_{3/2}^{-1}\sigma^*$). The ground state potential V_i and the intermediate state potential V_d of the Cl $2p \to \sigma^*$ core-excited state, i.e. HCl($2p_{3/2}^{-1}\sigma^*$), are taken from Ref. [25]. The final state potential V_f of HCl$^+$($^2\Sigma^-$) is taken from [99]. This example is very interesting because both the intermediate state and final state are repulsive. The potential energy difference $V_d - V_f$ in the asymptotic region ($R \to \infty$) is 180.7 eV, according to the experiments [25].

emission after dissociation [25, 82, 94].

To have a short review on resonant Auger processes in HCl, the measured electron spectrum, taken from [25], is depicted in Fig. 7.2(a). The experiment was performed under the resonant photon energy ω=201 eV for the process HCl → HCl($2p_{3/2}^{-1}\sigma^*$). Eight peaks are labeled in panel (a). Peaks 1-5 result from the *atomic* limits of the resonant Auger processes. They are the fingerprints of the dissociative intermediate state *d*. The other peaks i-iii, are produced exclusively by the photoionization process [25]. Following the analysis in Ref. [25], we associate each individual peak with its possible channels, see Table 7.1. Also, under the one electron picture, the photoionization process and the resonant Auger processes access different ionic final states. Unfortunately, there are still many final states, e.g. $^4\Sigma^-$, $^2\Sigma^-$, $^4\Pi$, $^2\Delta$, (2) $^2\Sigma^+$, (3) $^2\Pi$, (3) $^2\Sigma^+$, whose potentials lie in the same energy range, see Fig. 7.3, and consequently it is impossible to distinguish individual final state contribution from experiments. Most literature studies hence rely on numerical simulations to suggest the *shape* of a chosen final state [25, 97, 98] without considering the absolute intensity.

To carry out our simulations, the first issue is to choose a channel and its transition rate. Here we have chosen the channel HCl($2p^5\sigma^*$) → HCl$^+$($^2\Sigma^-$), which dissociates into Cl$^+$ ($3p^{-2}\ ^3P$) and H. Potential curves for this channel are depicted in Fig. 7.1. The potential curves V_i and V_d for the ground state and intermediate state [HCl($2p_{3/2}^{-1}\sigma^*$)] are taken from Ref. [25], while the final state [HCl$^+$($^2\Sigma^-$)] potential is taken from Ref. [99].

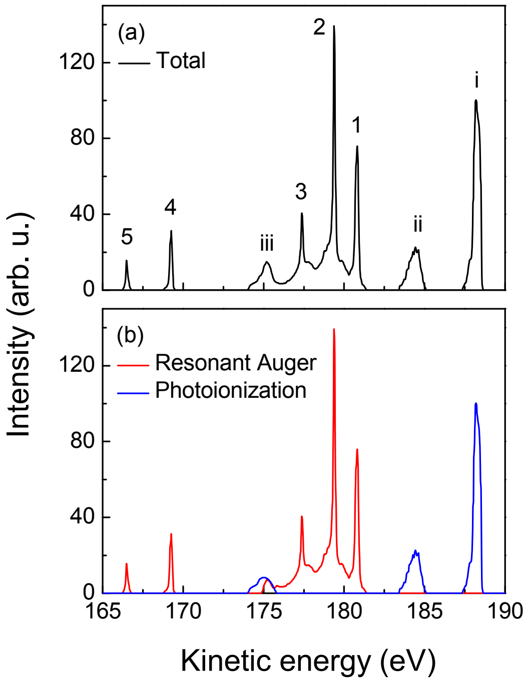

Figure 7.2: The experimental observation of the electron spectrum measured from HCl($2p_{3/2}^{-1}\sigma^*$) under the photon energy $\omega = 201$eV. In panel (a) the total electron spectrum, which is taken from Ref. [25], is depicted. Eight major peaks are labelled and can be divided into two groups: the photoelectrons, labelled by the Roman numerals, and the resonant Auger electrons, labelled by the Arabic numerals. Detailed labels for each peak are given in Table 7.1. The spectrum shown in panel (a) is then decomposed into the photoelectron and resonant Auger spectra, shown in panel (b). The former is also taken from Ref. [25].

Line	Process	Final States	Dissociation limit (Cl^+)
1	resonant Auger	$^4\Sigma^-$, $^2\Sigma^-$, $^4\Pi$	$3p^{-2}$ (^3P)
2		$^2\Delta$, (2) $^2\Sigma^+$, (3) $^2\Pi$	$3p^{-2}$ (^1D)
3		(3) $^2\Sigma^+$	$3p^{-2}$ (^1S)
4		not listed	$3s^{-1}3p^{-1}$ (^3P)
5			$3s^{-1}3p^{-1}$ (^1P)
i	photoionization	$2\pi^{-1}$ ($X\,^2\Pi$)	bound states
ii		$5\sigma^{-1}$ ($A\,^2\Sigma^+$)	
iii		$4\sigma^{-1}$ and satellites	

Table 7.1: The channel analysis based on Refs. [25, 99].

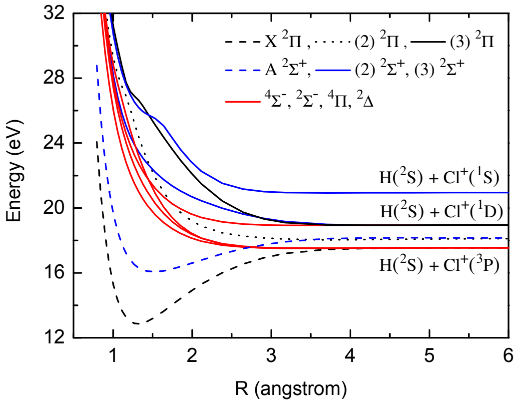

Figure 7.3: Potential curves of HCl$^+$. Bound states $X\,^2\Pi$ and $A\,^2\Sigma^+$, depicted by dashed lines, are populated exclusively by direct photoionization. The state $(2)\,^2\Pi$, depicted by the dotted line, converges to a different dissociation limit, viz. H$^+$ + Cl(^2P), which is not populated. All other states, depicted by solid lines, are populated via resonant Auger processes. The four red curves are (energetically from low to high) $^4\Sigma^-$, $^2\Sigma^-$, $^4\Pi$, $^2\Delta$ as listed in the legend. Similarly, the two solid blue curves depict $(2)\,^2\Sigma^+$ and $(3)\,^2\Sigma^+$, and are sorted according to ascending energy. All these curves are taken from Ref. [99].

This channel has an atomic Auger peak at 180.7 eV [25], see also Fig. 7.2. How to obtain the transition rate of this channel? The transition rate can be evaluated via multiplying the total Auger width (or Auger transition rate), which is suggested to be 90 meV from the experiments [25], with the branching ratio, i.e. the percentage going into the channel. To obtain the branching ratio into HCl$^+$($^2\Sigma^-$), the resonant Auger spectrum is separated from the ionization contribution, see Fig. 7.2(b). Unfortunately, due to many final states lying in the same energy range, we can only estimate the averaged branching ratio for a single final state. The quadrature of the Cl$^+$ ($2p^{-2}$) spectrum, between 175 eV and 181 eV, is 92.27 % of all quadrature available from the current resonant Auger spectrum. If the states are assumed to be equally populated, the averaged branching ratio is 7.098 % for a single non-degenerate final state, e.g. $^2\Sigma^-$. The transition rate of this state is then 6.39 meV.

The transition dipole moment is also required for simulating the resonant Auger process. Due to the spin-orbit coupling, the relativistic transition dipole moment to the excited state HCl($2p_{3/2}^{-1}6\sigma^*$) is 0.02877 a.u. [100], which is significantly smaller than the one for the major configuration HCl($2p\,\pi^{-1}6\sigma^*\ ^1\Pi$), which is 0.0365 a.u. [100]. For most of our simulations the *relativistic* transition dipole moment (0.02877 a.u.) is used. The *non-relativistic* transition dipole moment is only employed to show the influence of using an inaccurate transition dipole moment. Finally, when the direct photoionization is considered, the photoionization cross section σ_i (0.0152317 a.u.) is evaluated from the oscillator strength density $\frac{df(\varepsilon)}{d\varepsilon}$ (0.003886 eV^{-1}) [101] according to the formula $\sigma_i = \frac{2\pi^2}{c}\frac{df(\varepsilon)}{d\varepsilon}$ [102].

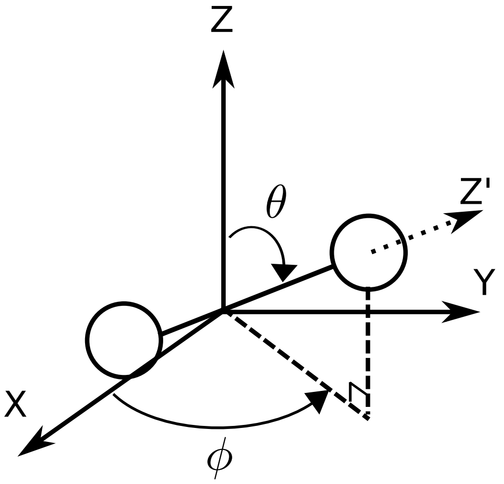

Figure 7.4: A diatomic molecule in the laboratory frame. The origin is chosen at the center of mass. The orientation of the internuclear axis Z' can be described by the angles θ and ϕ, which are the usual variables for spherical coordinates. The angle between the internuclear axis Z' and the lab Z axis is θ. The projection of the axis Z' onto the X-Y plane and the X axis define another angle ϕ.

7.2 Theory

A time dependent approach for the resonant Auger process in the a weak laser field regime has been reported in Ref. [26]. It is almost identical to what was introduced in Ch. 2, except that the initial process now is a photoexcitation process instead of a photoionization process, i.e. no photoelectron is produced, and now the decay process is a single step decay instead of a cascade decay. The total wave function ansatz for the current system of interest reads [26],

$$|\Psi(t)\rangle = |\psi_i(t)\rangle|\phi_i\rangle \,+\, |\psi_d(t)\rangle|\phi_d\rangle \,+\, \sum_\gamma \int \mathrm{d}E_e \; |\psi_{f_\gamma}(E_e,t)\rangle|\phi_{f_\gamma},E_e\rangle \;, \tag{7.1}$$

where $|\phi_\alpha\rangle$ and $|\psi_\alpha\rangle$ denote the electronic and nuclear wave functions of state α, respectively, with $\alpha = i, d$. Due to the presence of the emitted Auger electron, the final states are embedded in the continuum, and $|\phi_{f_\gamma}, E_e\rangle$ denotes the electronic wave function of state f_γ combined with the wave function of the emitted Auger electron, having a kinetic energy E_e. The amplitude to have such an electronic state is then given by the nuclear wave function $|\psi_{f_\gamma}(E_e,t)\rangle$, which depends on E_e. After the center-of-mass motion is separated, all the nuclear wave functions depend on the variables R, θ, and ϕ, where R denotes the internuclear distance, and θ and ϕ describe the orientation of the internuclear axis (Z') in the laboratory frame, see Fig. 7.4 for illustration. However, one should keep in mind that for more and more intense fields the direct photoionization of the valence electrons will become more and more important, and in consequence the ansatz shown in Eq. (7.1) will become invalid. For simplicity, here we first concentrate on only the resonant Auger process, as is usually done for weak laser pulses [26] as a starting point to investigate what can happen under intense laser fields. The process including the direct photoionization will be discussed in Sec. 7.4.

Following the same procedure as described in Ch. 2, the EOMs for the nuclear wave functions are

$$
\begin{aligned}
i|\dot{\psi}_i(t)\rangle &= \hat{H}_i|\psi_i(t)\rangle + \hat{F}^\dagger(t)|\psi_d(t)\rangle && (7.2)\\
i|\dot{\psi}_d(t)\rangle &= \hat{F}(t)|\psi_i(t)\rangle + (\hat{H}_d - i\frac{\Gamma}{2})|\psi_d(t)\rangle && (7.3)\\
i|\dot{\psi}_{f_\gamma}(E_e,t)\rangle &= \hat{W}_{d\to f_\gamma}(E_e)|\psi_d(t)\rangle + (\hat{H}_{f_\gamma} + E_e)|\psi_{f_\gamma}(E_e,t)\rangle \ , && (7.4)
\end{aligned}
$$

where the decay rate Γ and the matrix element $W_{d\to f_\gamma}$ are connected by

$$\Gamma = \sum_\gamma 2\pi |W_{d\to f_\gamma}|^2 \ .$$

The interaction between the molecule and the external laser field is given by

$$\hat{F}(t) = \boldsymbol{\mu} \cdot \mathbf{E}(t) \ ,$$

where $\boldsymbol{\mu}$ denotes the transition dipole moment $\langle \Phi_d|\hat{\mathbf{D}}|\Phi_i\rangle$, where $\hat{\mathbf{D}}$ is the electric dipole operator, and $\mathbf{E}(t)$ denotes the external laser electric field.

How to choose the external laser electric field? To keep the model simple, we begin with linearly polarized light for which the electric field is oscillating in the Z direction with an amplitude ε_0, and the light itself is propagating in the X direction of the laboratory frame. In addition, the pulse is assumed to have a Gaussian envelope $g(t)$, and hence the laser electric field reads

$$\mathbf{E}(t) = \varepsilon_0 \cos(kx - \omega t) g(t) \hat{z} \ , \tag{7.5}$$

where $\hat{z}$ is the unit vector in the Z direction. x, k, and ω are the X coordinate of the Lab frame, the wave number of the pulse, and the incident photon energy, respectively. The pulse envelope $g(t)$, whose duration is much longer than the oscillation period of $\cos \omega t$, is often chosen as a Gaussian function, namely $g(t) = e^{-(t/\tau)^2}$. For such a pulse, the cycle-averaged intensity of the laser field reads

$$I(t) = \frac{1}{8\pi\alpha}\varepsilon_0^2 g^2(t) \ , \tag{7.6}$$

where α is the fine structure constant. Since the pulse is time-dependent, comparing the pulse intensities of two different pulses has to be done at the same t. The easiest choice is to compare the maximum (peak) intensity, which is the intensity of the top of the envelope, i.e. when $g^2(t) = 1$. Hence the pulse intensity will be referred to the maximum intensity hereafter.

How to evaluate $\hat{F}(t)$ for a given electric field as shown in Eq. (7.5)? The molecule, located at the center of the Lab frame, is composed of atoms at different coordinates (in the Lab frame). Each atom experiences an electric field depending on its coordinate x, the magnitude of which is around the same size of the molecule, e.g. HCl bond length is 1.28 Å. For photon energies of interest, i.e. around 201 eV, the wavelength of the photon (61.8 Å) is still much larger than this size. Hence the term kx is negligible inside the molecule, yielding

$$\cos(kx - \omega t) \simeq \cos(\omega t) ,$$

which is often called the *long wavelength approximation* [37, 38]. In consequence, the whole molecule experiences the same field strength. Additionally, $\cos(\omega t)$ can be separated into

$$\cos(\omega t) = \frac{1}{2} e^{-i\omega t} + \frac{1}{2} e^{i\omega t} ,$$

where the first term is dominant in a photon absorption process, while the second term is dominant in a photon emission process [37, 38]. Keeping only the dominant term, according to the process of interest, is called the *rotating wave approximation* [37, 38]. Let us take $\hat{F}(t)|\psi_i(t)\rangle$, shown in Eq. (7.3), as an example. This term describes a photon absorption process from state i to state d, and under the mentioned approximations, it reads

$$\hat{F}(t)|\psi_i(t)\rangle = V(\theta, t)e^{-i\omega t}|\psi_i(t)\rangle , \tag{7.7}$$

where

$$V(\theta, t) = \boldsymbol{\mu} \cdot \hat{z}\, \frac{\varepsilon_0}{2} g(t) .$$

The term $V(\theta, t)$ can be further simplified by evaluating the inner product $\boldsymbol{\mu} \cdot \hat{z}$. The transition dipole moment of a diatomic molecule is either parallel, e.g. Σ to Σ transition, or perpendicular, e.g. Σ to Π transition, to the molecular axis. If the transition dipole moment with magnitude μ is parallel to the molecular axis, the term $\boldsymbol{\mu} \cdot \hat{z}$ results in[2] $\mu \cos\theta$, see Fig. 7.5.

On the other hand, if the transition dipole moment is perpendicular to the molecular axis, the situation is not so trivial. Let us explain. In Fig. 7.5, the other two axes of the molecular frame can be chosen freely as long as they are perpendicular to the molecular axis Z'. A usual choice is to keep one of the molecular axes always *perpendicular* to the laboratory Z axis, and the other one always coplanar with the Z-Z' plane. Fig. 7.5 is a snapshot of the molecular rotation when the molecular Z' axis lies in the Y-Z plane. Only half of the molecule is depicted here. The molecular X' axis is chosen to be coplanar with the Z and Z' axes, so that the molecular Y' axis, currently pointing outside the paper, is perpendicular to the laboratory Z axis.

Due to rotational symmetry around the Z' axis, the Π state is doubly degenerate in the X' and Y' direction, but only one micro-state of Π (X') is going to be populated when we choose a linearly polarized light in the laboratory Z direction, because the

---

[2] $\mu = |\boldsymbol{\mu}|$

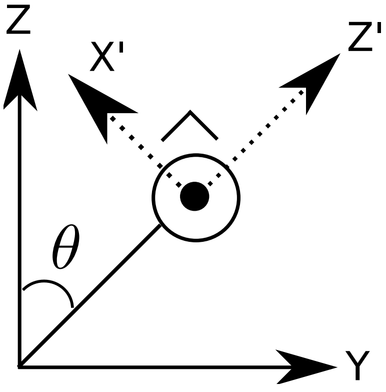

Figure 7.5: A snapshot of the molecular rotation in the molecular frame detail showing only half of the molecule. The molecule rotates in the laboratory frame and at some point its molecular axis Z' lies on the Y-Z plane. The other two molecular axes then can be chosen as follows: X' being coplanar with the Y-Z plane, and Y' (shown by the black circle) pointing outside the Y-Z plane. With this choice, the molecular Y' axis is perpendicular to the laboratory Z axis all the time during the molecular rotation, and the molecular X' axis is always coplanar with the Z-Z' plane.

other (Y') is always *perpendicular* to the Z axis. In consequence, the transition dipole moment with magnitude μ perpendicular to the molecular axis provides $\boldsymbol{\mu}\cdot\hat{z} = \mu\sin\theta$.

In the case of core-excited HCl($2p_{3/2}^{-1}6\sigma^*$), the leading configuration is a Π state, and hence $\boldsymbol{\mu}\cdot\hat{z} = \mu\sin\theta$ is used in our calculation. Using Eq. 7.7, the EOMs now read

$$\begin{aligned} i|\dot{\psi}_i(t)\rangle &= \hat{H}_i|\psi_i(t)\rangle + V(\theta,t)e^{i\omega t}|\psi_d(t)\rangle && (7.8)\\ i|\dot{\psi}_d(t)\rangle &= V(\theta,t)e^{-i\omega t}|\psi_i(t)\rangle + (\hat{H}_d - i\Gamma/2)|\psi_d(t)\rangle && (7.9)\\ i|\dot{\psi}_{f_\gamma}(E_e,t)\rangle &= \hat{W}_{d\to f_\gamma}(E_e)|\psi_d(t)\rangle + (\hat{H}_{f_\gamma} + E_e)|\psi_{f_\gamma}(E_e,t)\rangle\ , && (7.10)\end{aligned}$$

where

$$V(\theta,t) = \frac{\varepsilon_0}{2}g(t)\mu\sin\theta\ .$$

As before, the initial wave packet is chosen as the lowest vibrational eigenfunction of state i, $|\psi_i(0)\rangle = |\chi_i(\nu=0)\rangle$, while other nuclear wave functions are initially zero.

In principle Eqs. (7.8–7.10) can be employed as the working equations without any modification. In practice, one likes to smooth the time-dependent part of the Hamiltonian to improve the numerical stability. For example, the phases $e^{\pm i\omega t}$ appearing in Eqs. (7.8-7.9) can be removed by replacing the wave functions $|\psi_d(t)\rangle$ and $|\psi_f(E_e,t)\rangle$ by $e^{-i\omega t}|\tilde{\psi}_d(t)\rangle$ and $e^{-i\omega t}|\tilde{\psi}_f(E_e,t)\rangle$. Consequently, the working equation of the final state becomes

$$i|\dot{\tilde{\psi}}_{f_\gamma}(E_e,t)\rangle = \hat{W}_{d\to f_\gamma}(E_e)|\tilde{\psi}_d(t)\rangle + (\hat{H}_{f_\gamma} + E_e - \omega)|\tilde{\psi}_{f_\gamma}(E_e,t)\rangle\ , \qquad (7.11)$$

where $|\tilde{\psi}_d(t)\rangle$ and $|\tilde{\psi}_{f_\gamma}(E_e,t)\rangle$ are the dressed nuclear wave functions of states d and f. Additionally, the working equations of the coupled first two states (i and d) can be grouped together and written as

$$i|\dot{\psi}_{id}(t)\rangle = \hat{H}_{id}(t)|\psi_{id}(t)\rangle \ , \tag{7.12}$$

where $|\psi_{id}(t)\rangle$ is a column vector with components $|\psi_i(t)\rangle$ and the dressed nuclear wave function $|\tilde{\psi}_d(t)\rangle$. The 2-by-2 Hamiltonian matrix reads

$$\hat{H}_{id}(t) = \hat{T}_N + \begin{pmatrix} V_i(R) & V(\theta,t) \\ V(\theta,t) & V_d(R) - i\Gamma/2 - \omega \end{pmatrix} . \tag{7.13}$$

Here, $\hat{T}_N$ is the common nuclear kinetic energy operator for the stretching motion along the internuclear distance R as well as for the rotational motion. V_i and V_d are the potential curves of the states i and d, respectively. The photon energy now appears in Eq. (7.13), and this can be viewed as having an effective potential which is shifted by ω from the original potential. In consequence, if one plots the effective potential curves for the state i and the dressed state d, one immediately sees the intersections between the potential curves.

Eq. (7.13) is also an exciting result because the Hamiltonian $\hat{H}_{id}$ is exactly the diabatic representation for two coupled electronic states [103, 104]. If $V(\theta,t)$ is not time dependent, e.g. if $g(t) = 1$ for all t, and if there is no decay from state d to state f, i.e. if Γ is zero, then the potential energy surfaces between the two coupled states exhibit a conical intersection at $V(\theta) = 0$ [89], i.e. $\theta = 0$ in our case. The impact of such light-induced conical intersections (LICI) on the molecular dynamics has been recently demonstrated [89]. If we still keep $g(t) = 1$ but allow the presence of a non-vanishing Γ, the situation becomes more complicated. The two adiabatic potential energy surfaces in R and θ space (obtained by diagonalizing the potential energy matrix $\hat{H}_{id} - \hat{T}_N$) are now complex and in consequence exhibit *two* intersecting points where the real as well as the imaginary part of the two electronic energies are degenerate [104]. Take $g(t) = 1$ and the pulse intensity 10^{19} W/cm^2 for example. The adiabatic potential surfaces of the HCl ground state and the dressed HCl core excited state are depicted in Fig. 7.6. The left panel shows the real part of the two adiabatic potential energy surfaces, and a seam of intersection is clearly depicted in the zoomed inset. Due to the presence of a decay rate, the imaginary parts of the two adiabatic potential energy surfaces also intersect, as shown in the right panel. More importantly, the imaginary parts of the potential surfaces do not intersect where the real parts of the surfaces intersect, except at the two edges of the seams where both the real and the imaginary part of the potential surfaces intersect. This analogue to a conical intersection in the continuum has been termed [104] *doubly intersecting complex electronic surfaces* (DICES). Recall that $V(\theta,t)$ actually depends on t, and hence the intersection positions of the DICES vary with time (i.e. with the pulse). Therefore we speak of *dynamic* DICES, which are induced by light, and this gives rise to dramatic dynamic effects.

The numeric solution of the equations of motion is carried out with the Heidelberg Multi-Configuration Time-Dependent Hartree (MCTDH) package [105, 106], and as

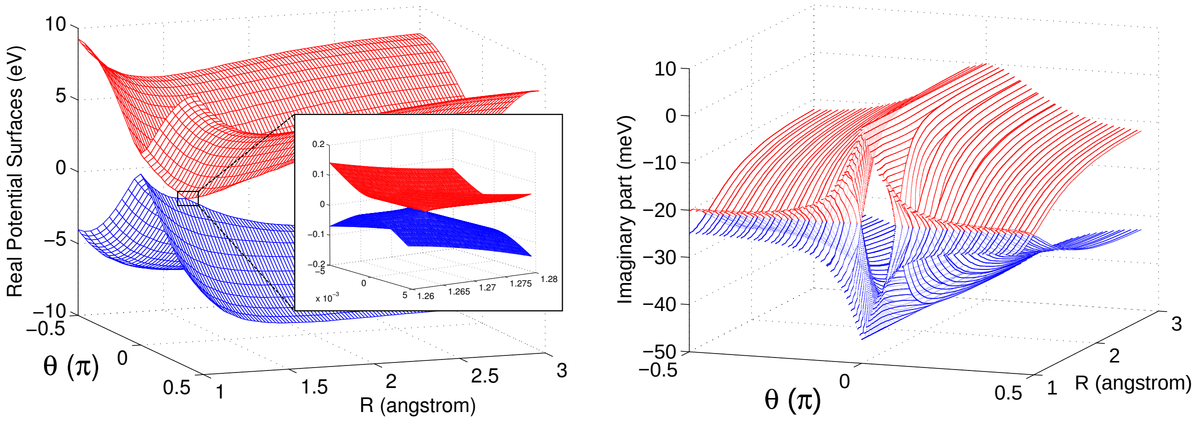

Figure 7.6: Adiabatic (effective) potential energy surfaces in HCl under an intense laser field. When dressed by X-ray laser light of frequency $\omega = 201$ eV and intensity 10^{19} W/cm^2, the ground state and intermediate core excited state potentials become doubly intersecting surfaces in R and θ space. Their real part is shown in the left panel and the imaginary part in the right panel.

before, the resonant Auger electron spectrum for a single partial channel is computed via

$$\sigma_e^{(\gamma)}(E_e) = \lim_{t\to\infty} \langle \psi_{f_\gamma}(E_e,t)|\psi_{f_\gamma}(E_e,t)\rangle = \lim_{t\to\infty} \langle \tilde{\psi}_{f_\gamma}(E_e,t)|\tilde{\psi}_{f_\gamma}(E_e,t)\rangle \ . \tag{7.14}$$

Finally, there are two remarks. The first one concerns the numerical details. In the MCTDH method [105, 106], the nuclear wave functions are always written in a product form, for instance $|\psi_i(t)\rangle = \sum_{j_1,j_2} A_{j_1,j_2}(t)|\varphi^R_{j_1}(R,t)\rangle|\varphi^{\theta,\phi}_{j_2}(\theta,\phi,t)\rangle$. $A_{j_1,j_2}(t)$ is the time-dependent coefficient of a specific configuration, and each configuration is a Hartree product of $|\varphi^R_{j_1}(R,t)\rangle$ and $|\varphi^{\theta,\phi}_{j_2}(\theta,\phi,t)\rangle$. The former denotes a one-dimensional *single particle function* (SPF) of the stretching motion along R, and the latter denotes the two-dimensional SPF for the molecular rotation, for which the underlying basis are the usual spherical harmonics Y_{lm}. However, only $|Y_{00}\rangle$ or $|Y_{10}\rangle$ will be populated by a linear polarized light with a weak X-ray intensity[3], and the standard treatment is to write the wave function as a single Hartree product $|\chi(R,t)\rangle|Y_{00}\rangle$ or $|\chi(R,t)\rangle|Y_{10}\rangle$. Projecting out the $|Y_{lm}\rangle$, the effective equations of motion depend only[4] on R for each electronic state, and θ in the Hamiltonian is replaced by $\langle Y_{00}|\sin\theta|Y_{00}\rangle = \pi/4$ or $\langle Y_{00}|\cos\theta|Y_{10}\rangle = 1/\sqrt{3}$.[5] We refer to such a calculation as a *1D* calculation since the effective number of degrees of freedom is only one. Of course, the dynamic DICES cannot be described in such calculations. On the other hand, many rotational levels are accessible via non-linear processes under intense pulses, which introduces strong rotations of the molecule. For this situation, it is necessary to keep θ as a variable

---

[3] The initial wave packet is chosen to be the product of $|Y_{00}\rangle$ and the ground vibrational level of the electronic ground state.

[4] For $l \neq 0$, one has an additional centrifugal potential $\frac{l(l+1)}{2mR^2}$, where m is the reduced mass.

[5] Note that $\langle Y_{00}|\sin\theta|Y_{20}\rangle \neq 0$ but it is omitted due to the low population assumption.

during the calculations, so that all the rotational levels can be populated according to the selection rules. We call this a 2D calculation because two degrees of freedom (R and θ) are included in the calculation. Note that the quantum number m, associated with the variable ϕ, does not change after the excitation process, due to the fact that we have chosen linearly polarized light instead of circularly polarized light in our example.

The second remark concerns Ref. [34], where we mistakenly took $V(\theta, t) \sim \cos\theta$, which does not apply to HCl($2p_{3/2}^{-1}6\sigma^*$), due to the author's neglect of considering the spin-orbital coupling. Additionally, the transition dipole moment used in Ref. [34] is incorrect, namely it is three times larger compared to the actual nonrelativistic value. Using a larger transition dipole moment μ results in a DICES effect of the same strength under a weaker intensity. A transparent comparison of using different values of μ is given in the next section.

7.3 Computations of the Molecular Resonant Auger Process in HCl

Ion Yield and Rabi Oscillation

As we already mentioned, we first neglect the direct photoionization in the following discussion and focus on the interplay between molecular dynamics and the external pulse. To determine when the system enters the non-perturbative regime, the ion yield ($1 - \lim_{t\to\infty}\langle\psi_i(t)|\psi_i(t)\rangle$ [52]) is investigated as a function of the pulse intensity, see Fig. 7.7. Two pulse durations are taken: $\tau = 2$ fs (a shorter pulse) and $\tau = 6.2$ fs (a longer pulse). For the shorter pulse, the ion yield obtained via a 2D calculation (black solid curve) quickly deviates from the one evaluated by a 1D calculation (black circles) at pulse intensities higher than 10^{16} W/cm^2, and it also starts to oscillate due to the fact that Rabi oscillation now can take place during the excitation process. In addition, the 1D calculation exhibits oscillations with a larger amplitude than the other. The disagreement between the two confirms that strong molecular rotation occurs and a full 2D simulation is necessary to accurately describe the dynamics in the strong field (intense pulse) regime.

The weak field regime refers to the intensity region where most of the population, e.g. 90 percent, still remains in the ground state after interaction with the pulse. In contrast, a strong field regime refers to the pulse intensity which is strong enough to introduce Rabi oscillations or other nonlinear processes during an excitation process. According to this definition, a pulse intensity like 10^{14} W/cm^2 is still considered to be weak (see the curves in Fig. 7.7), even though a laser field of this intensity is often

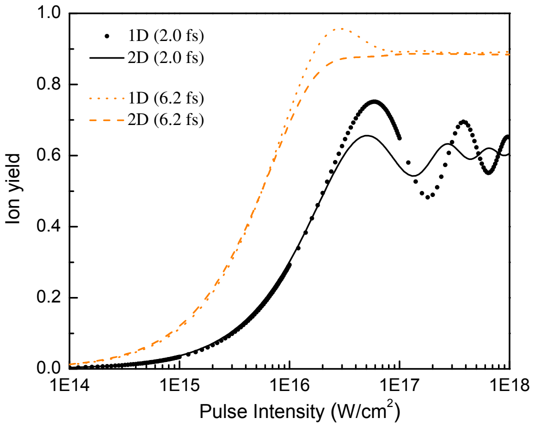

Figure 7.7: Ion yield plotted against pulse intensity in logarithmic scale, for the resonant Auger process of HCl($2p_{3/2}^{-1}6\sigma^*$). Black circles and the black solid curve show the ion yields for a pulse duration $\tau = 2$ fs, obtained by 1D and 2D calculations, respectively. When the pulse intensity is above 10^{16} W/cm^2, the two results start to deviate from each other, and both exhibit oscillatory structures, which are the fingerprint that Rabi oscillation takes place during the excitation process. Note that the 1D result has a larger oscillatory amplitude than the 2D result. The ion yields for a longer pulse duration ($\tau = 6.2$ fs) are also depicted in the figure. Surprisingly, neither the 1D (orange dotted curve) nor the 2D (orange dashed curve) simulation shows oscillatory character in comparison with the shorter pulse.

hardly considered as a weak field. This is simply because the transition dipole moment for the HCl core excitation is rather small.

Speaking of the oscillation feature of the ion yield, a similar feature was also found in the atom case [52] and was explained by Rabi oscillation. The Rabi oscillation concerns a *two level system* coupled by a pulse with photon energy on resonance, i.e. the same as the energy gap between the two levels, and no decay process is considered [38]. In such a model the ground state population oscillates in time, and the number of oscillations corresponds to the Rabi cycles. After the pulse is over, the probability of finding the population remaining in the ground state is related to the area of the pulse [107].[6] When the population is completely inverted, i.e. zero population remaining in the ground state, the area of the pulse can be π (half a Rabi cycle), 3π(one and a half Rabi cycles) and so on. Similarly, when the area of the pulse is 2π (one Rabi cycle), all the population returns to the ground state, and the excited state is not populated when the pulse is over [107]. If the excited state decays, this oscillatory structure is then represented in the resulting ion yield, and its maxima and minima are related to the area of the pulse as well as to the number of half Rabi cycles which the atom completes during the pulse [52]. Also, the maximal ion yield in an atomic level system is always 1 since the ground state population can be inverted and decays completely.

---

[6] The dimensionless quantity termed "area" is defined as $\frac{1}{\hbar}\int 2\mu E(t)\mathrm{d}t$ for an atomic level case.

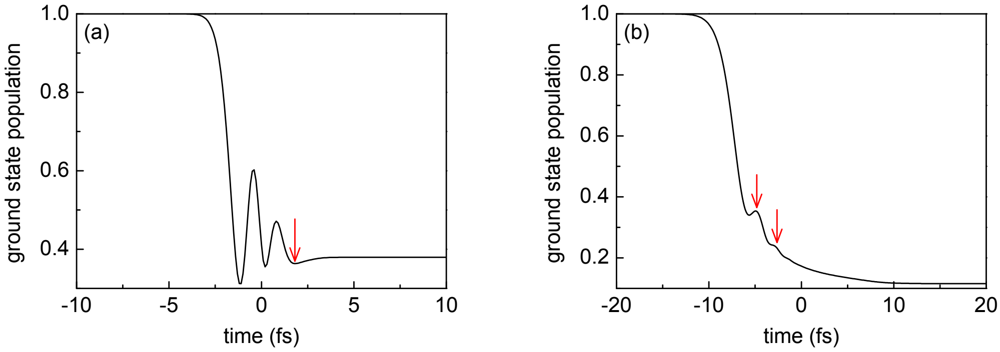

Figure 7.8: The HCl ground state population as a function of time. The pulse intensity is chosen to be 6.5×10^{17} W/cm^2, which corresponds to the third maximum of the black solid curve in Fig. 7.7. The ground state population for a pulse duration of 2 fs is depicted in panel (a), and the one for the longer pulse duration (6.2 fs) is depicted in panel (b). The population indeed undergoes Rabi oscillations but they are much less pronounced than what is known from atomic systems [52, 107].

The situation becomes more intricate for a molecule. First, shown in Fig. 7.7 is no ordinary Rabi oscillation since the maximal ion yield never reaches 1. Second, the extrema observed in Fig. 7.7 do not coincide with the number of half Rabi cycles. The two differences can be seen also from the time evolution of the ground state population. Take the ground state population of the third maximum (pulse intensity 6.5×10^{17} W/cm^2) of the black curve in Fig. 7.7 for example. According to the atomic level system, the third maximum ion yield is related to the 5th half Rabi cycle. However, the time evolution of the ground state population, shown in Fig. 7.8 (a), is never depleted completely and does not even stay in the third minimum (pointed out by an arrow) when the pulse is over.

Ion yields for a longer pulse (6.2 fs) are also depicted in Fig. 7.7. The 1D (orange dotted curve) and 2D (orange dashed curve) results deviate from the short pulse ones when the pulse intensity is stronger than 10^{15} W/cm^2. None of them shows a pronounced oscillatory structure in comparison with the ion yields obtained for a shorter pulse. Similarly, the time evolution of the ground state population in the longer pulse case shows some sort of oscillation (pointed out by arrows) but its amplitude is not very pronounced, e.g. see Fig. 7.8 (b) for a 2D calculation for the pulse intensity 6.5×10^{17} W/cm^2. In short, the atomic picture, based on a two level model, cannot explain our molecular simulation, where both R and θ must be included for an intense pulse. As we shall reveal, strong nonadiabatic effects dominate the molecular case.

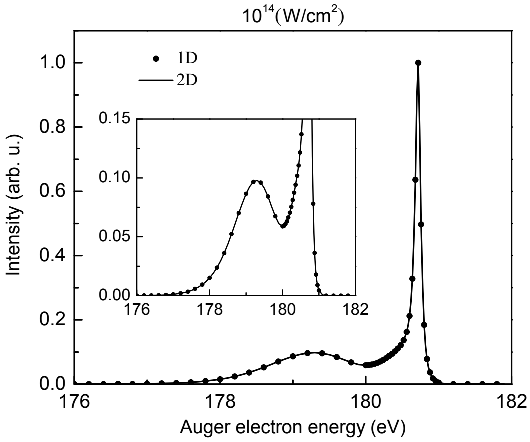

Figure 7.9: The resonant Auger spectra of $\mathrm{HCl}(2p_{3/2}^{-1}6\sigma^*)$ in the weak field regime. The parameters, e.g. the transition dipole moment and the decay rate, are illustrated in Sec. 7.1. The pulse duration τ is chosen to be 2 fs, and the pulse intensity is chosen to be 10^{14} W/cm^2. The 2D calculation (multiplied by 42.97) with the full dynamics of R and θ is shown by the black solid curve, and the 1D simulation (multiplied by 46.43) is depicted by the black circles. The two spectra coincide with each other, showing that mainly only the lowest rotational level $|Y_{00}\rangle$ is populated under the weak external field.

Resonant Auger Spectra and the Pulse Intensity

Our particular interest is on the resonant Auger electron spectrum under an intense laser field. For comparison, all Auger electron spectra will be scaled to the same height (set maximum peak to 1) and the scaling parameter will be given in each figure caption.

The resonant Auger electron spectra obtained by the 1D and 2D calculation for a shorter pulse ($\tau = 2$ fs) with intensity 10^{14} W/cm^2 are depicted in Fig. 7.9. In the 1D calculation, only the lowest rotational level $|Y_{00}\rangle$ is considered to be populated, and $\langle Y_{00}|\sin\theta|Y_{00}\rangle = \pi/4$ is used. The full 2D dynamics (R and θ) calculation coincides with the 1D spectrum, confirming that shapes of resonance Auger spectra can be obtained by numerically cheaper 1D simulations in the weak field regime.

Although a 1D simulation is sufficient to produce the shape of a spectrum for comparison with experiments that are performed under weak intensity, this procedure is expected to be inaccurate when the pulse intensity increases because the molecular rotation can then play a significant role. It is known that an atomic Auger spectrum develops multi-peak structure along with the Rabi cycles [52], e.g. atomic Auger spectra exhibit single, double, and triple peak structures while the pulse intensity reaches the first three maxima of the ion yield. This is, however, not the case for the molecular resonant Auger spectrum. Fig. 7.10 shows the resonant Auger spectra for the intensities corresponding to the first three maxima of the ion yield. Along with the increasing pulse intensity, the spectrum broadens, but no multi-peak structure is found.

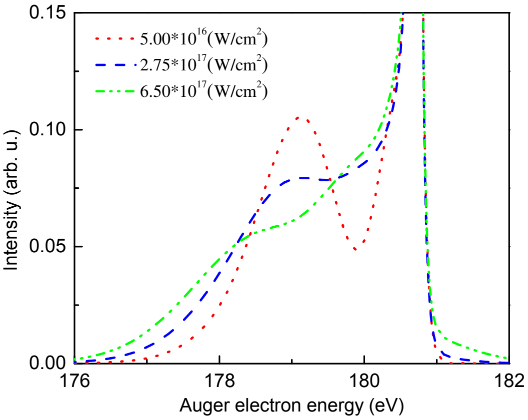

Figure 7.10: The resonant Auger spectra of HCl($2p_{3/2}^{-1}6\sigma^*$) obtained via 2D simulation. The pulse intensity is chosen to be 5×10^{16} (multiplied by 0.26), 2.75×10^{17} (multiplied by 0.29), and 6.5×10^{17} (multiplied by 0.30) W/cm^2, which corresponds to the first, second, and third maximum of the ion yield, respectively. The spectrum becomes broader with increasing intensity but no multi-peak structure is found, due to the dynamic DICES effect.

This smooth broadening without peak splitting is purely due to the molecular dynamics influence. In fact, as we already mentioned in Sec. 7.2, the molecular motion under a strong laser field can be viewed as being caused by a strong nonadiabatic effect between the ground state and the dressed excited state. Due to the decay of the dressed excited state, the adiabatic surfaces of the two states have generally two intersections, and hence the surfaces have been named DICES. It is the effect of DICES that keeps the spectrum from splitting. This idea is supported by comparing the spectra evaluated by 2D (DICES) and 1D (no DICES) calculations, see Fig. 7.11. Apart from the atomic peak at 180.72 eV, the 1D simulation shows additionally two molecular peaks at 175.3 eV and 184 eV. The energy gap between the two molecular peaks depends on the pulse intensity. In contrast with the 1D simulation (no DICES), the 2D spectrum shows that DICES effectively quenches the peak splitting behavior and results in a smooth broadening, i.e. a flat molecular background from 172 eV to 185 eV.

The strong molecular rotation induced by the external intense laser field is a crucial step for light-induced DICES (or LICI). In Fig. 7.12 the distribution of the angular momentum for the HCl ground state after the pulse (10^{19} W/cm^2) is depicted. Even though the angular momentum is chosen to be $J = 0$ for the ground state initial wave packet, the angular momentum now has a wide distribution up to $J = 40$.

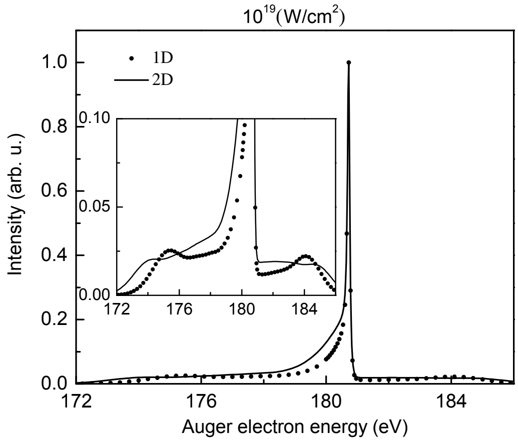

Figure 7.11: The resonant Auger spectra of of HCl($2p^{-1}_{3/2}6\sigma^*$) obtained via 1D (black circles) and 2D (black solid line) simulations under a pulse intensity of 10^{19} W/cm^2. The 1D and 2D results have been multiplied by 0.36 and 0.47, respectively, for comparison. Both spectra spread over a large energy range. The pronounced peak at 180.72 eV is due to the atomic contribution. A zoom of the spectra focusing on the molecular contribution is depicted in the inset. The 1D (no DICES) spectrum has an obvious two peak structure at 175.3 eV and 184 eV. In contrast to the 1D result, the 2D (DICES) spectrum only spreads out smoothly and exhibits no peaks.

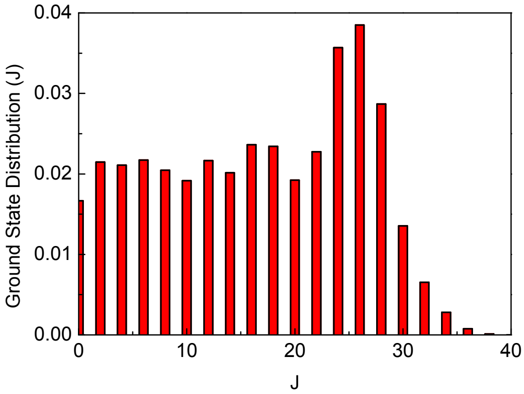

Figure 7.12: The angular momentum distribution for the ground state of HCl after the pulse. The pulse intensity and duration are the same as used in Fig. 7.11. The initial ground state angular momentum is chosen as $J = 0$. After the pulse, the ground state angular momentum distribution extends up to $J = 40$.

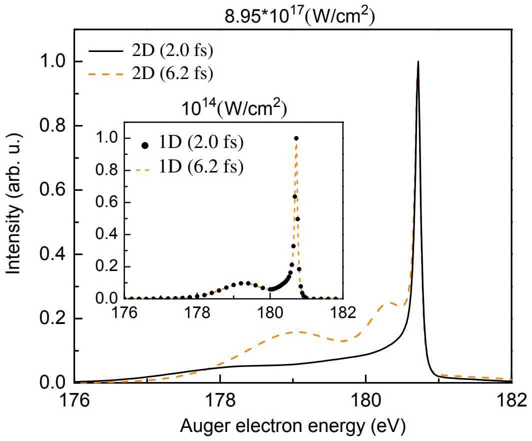

Figure 7.13: The role of the pulse duration in the weak field and strong field regimes. The 1D spectra for $\tau = 2$ fs (multiplied by 46.43) and $\tau = 6.2$ fs (multiplied by 13.38) under the pulse intensity 10^{14} W/cm^2 (weak field) are depicted in the inset. No peak narrowing effect is found in this case due to the strongly dissociative state d. In contrast, 2D spectra for $\tau = 2$ fs (multiplied by 0.32) and $\tau = 6.2$ fs (multiplied by 0.34) under an intense intensity of 8.95×10^{17} W/cm^2 have very different shape. The latter exhibits a stronger molecular background than the former, showing that the dynamic DICES effect is much stronger in an intense long pulse excitation.

Role of the Pulse Duration

What is the role of the pulse length during the resonant Auger process? Performing a Fourier transform of the pulse envelope $g(t)$, we obtain the frequency (energy) distribution of the pulse $\tilde{g}(\omega)$, shifted by the photon energy. The excitation width Δ, usually referred to as *photon bandwidth* in experiments, is defined [26] as the FWHM of $|\tilde{g}(\omega)|^2$. For pulse durations $\tau = 2$ fs and $\tau = 6.2$ fs, these pulse excitation widths Δ are 0.776 eV and 0.25 eV, respectively. The former is comparable to the core excited HCl Auger decay rate $\Gamma = 0.9$ eV, while the latter excitation width, i.e. 0.25 eV, is much narrower. According to the ARRE effect, a narrow photon bandwidth, namely $\Delta < \Gamma$, causes an Auger line width narrower than the natural width [75]. The same effect could also take place in a molecular resonant Auger process, e.g. see Ref. [26] for the core excited N_2 molecule. However, for a molecule with a dissociative final state, a strong molecular dissociation can suppress the peak narrowing effect, e.g. see Ref. [108] for the resonant Auger of HF. The inset of Fig. 7.13 shows a similar scenario: for a weak intensity of 10^{14} W/cm^2, the 1D resonant Auger spectra of HCl obtained from the two different pulse durations coincide with each other.

On the other hand, the 2D spectra for the same two pulse lengths under an intensive pulse intensity of 8.95×10^{17} W/cm^2 show a strong difference. The spectrum for $\tau = 6.2$ fs has a more pronounced molecular background than the one for $\tau = 2$ fs. This is clearly not an effect of the usual ARRE line narrowing nor the one of molecular dissociation quenching line narrowing. In fact, the result indicates that under the same pulse intensity, the dynamic DICES has a stronger impact on the molecular dynamics in a longer pulse.

Transition Dipole Moment and Pulse Intensity

Previously it was mentioned that the actual location of the strong field regime depends on the transition dipole moment μ of a system. Hence the simulated results are sensitive to the value of μ. Recall that precise direct experimental measurements of μ are currently not available, and our current value of μ is taken from a relativistic *ab initio* calculation [100]. The impact of employing a different transition dipole moment μ in the current model is trivial and can be understood from the calculations of the ion yield. Let us compare the ion yields obtained from two different *ab initio* calculated μ, namely a relativistic one and a nonrelativistic one [100]. The pulse duration is again chosen as $\tau = 2$ fs.

Fig. 7.14 shows the ion yields calculated with a nonrelativistic μ (0.0365 a.u.) and with a relativistic μ (0.02877 a.u.). At first glance, the two results look similar. If we shifted the non-relativistic result (red dashed line) toward a larger pulse intensity, we expect that the two ion yields coincide, cf. black solid curve and the red open circles. This fact is easy to understand. The transition dipole moment appears in the term $V(\theta, t)$ in the DICES Hamiltonian given by Eq. (7.13). This term contains $\frac{\varepsilon_0 \mu}{2} g(t) \sin\theta$, where the pulse intensity also comes into play through ε_0. Accordingly, exactly the same $V(\theta, t)$ can be obtained for two different transition dipole moments as long as the chosen field intensities compensate the difference. For instance, if μ is doubled from its original value, the predicted result will appear at a 4 times lower intensity than the original. Therefore, under the current model, using an inaccurate μ influences only the pulse intensity by a factor, while the ion yield or spectrum remain unchanged.

7.4 Including the Impact of Ionization in an Intense X-Ray Field

Although providing many interesting insights into the light-induced strong nonadiabatic effects, e.g. DICES in our example, the previous model is unfortunately not fully correct because it neglects the direct photoionization under an intense X-ray field, as well as the possibility for non-resonant transitions to higher core-excited states, e.g. $\mathrm{HCl}(2p_{1/2}^{-1} 6\sigma^*)$. The Auger process of this non-resonant transition is not observed in the usual weak field measurements [25], but it could be important in the strong field measurement. To demonstrate the problem, let us first include only the direct pho-

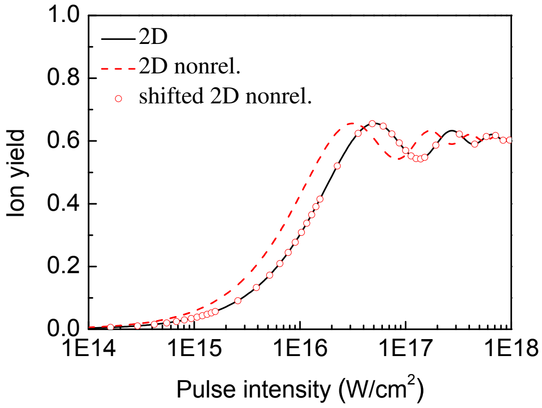

Figure 7.14: Influence of the value of μ on the ion yield. The ion yield evaluated by using the relativistic μ is depicted by the black solid curve, while the one evaluated by using the nonrelativistic μ is depicted by the red dashed line. The open circles depict the nonrelativisitc ion yield shifted toward higher pulse intensity, and the result completely coincides with the black solid curve. This agreement demonstrates that the transition dipole moment μ and the pulse intensity together determine the results.

toionization of the valence electrons into our simulation.

The direct photoionization of the valence electron in HCl is already not negligible under weak intensity [25]. Besides, it has also been shown for atomic cases that the direct photoionization of valence electrons is relevant under an intense X-ray field [40, 88, 91]. The rate of photoionization has been illustrated in Ch. 2 and Appendix C. It reads [40]

$$\Gamma_{\text{ph}} = \frac{\sigma_i \, I(t)}{\omega} \,, \tag{7.15}$$

where σ_i[7] is the ionization cross section of the valence electron for the molecule being in its electronic ground state, $I(t)$ is the intensity, and ω is the energy of the photons. Since the direct photoionization and the resonant Auger decay populate different final states, as it was explained in Sec. 7.1, the interference between these different channels is negligible.

Following a similar process as in Sec. 7.2 but using a total wave function ansatz including the direct photoionization to different final states, the working equations for the HCl molecule[8] are equivalent to simply inserting the ionization rate into the Hamiltonian from Eq. (7.13). The working equations for the ground state and the dressed

---

[7] The value is 0.0152317 a.u. for HCl.

[8] For HCl, the direct photoionization and the resonant Auger process populate different ionic states and hence there is no interference between these channels.

intermediate state now read [109]

$$i \begin{pmatrix} |\dot{\psi}_i(t)\rangle \\ |\dot{\psi}_d(t)\rangle \end{pmatrix} = \begin{pmatrix} H_i(R) - i\Gamma_{\mathrm{ph}}^{(i)}/2 & V(\theta, t) \\ V(\theta, t) & H_d(R) - i(\Gamma + \Gamma_{\mathrm{ph}}^{(d)})/2 - \omega \end{pmatrix} \begin{pmatrix} |\psi_i(t)\rangle \\ |\psi_d(t)\rangle \end{pmatrix}, \tag{7.16}$$

where $\Gamma_{\mathrm{ph}}^{(i)}$ and $\Gamma_{\mathrm{ph}}^{(d)}$ are the ionization rates of the valence electrons from state i and state d, respectively. They are approximately the same [40, 88, 109] and can be evaluated from Eq. (7.15). For a short pulse duration, further ionization after the Auger decay is neglected and the working equation for the dressed final state is the same as Eq. (7.11). With the additional imaginary potential, which originates from the direct photoionization, the Hamiltonian in Eq. (7.16) still describes the two coupled states in the diabatic representation. More importantly, both potential surfaces are now complex, and hence we still have DICES in our system. Including or omitting the direct photoionization will not change the existence of DICES but will influence the position of the intersections and hence affect the molecular motions.

Full 2D simulations for the resonant Auger process with the competition from direct photoionization were performed and are presented in Fig. 7.15. Due to the strong ionization under the intense laser field, the ion yield $1 - \lim_{t\to\infty}\langle\psi_i(t)|\psi_i(t)\rangle$ (red solid curve) deviates from the result without ionization (black dashed line) already from rather weak intensity, i.e. 10^{15} W/cm^2, as shown in Fig. 7.15 (a). Unsurprisingly, such strong ionization directly competes with the probability that the system undergoes the resonant Auger process, especially when the pulse intensity increases. When the pulse intensity reaches 10^{17} W/cm^2, the HCl molecule is completely ionized, mainly by the direct photoionization and partially by the resonant Auger process.

The impact of the photoionization on the resonance Auger electron spectrum for a pulse intensity of 5×10^{16} W/cm^2 is shown in Fig. 7.15 (b). Due to the competition from the direct photoionization, the contribution going into the resonant Auger process is, of course, strongly reduced. Interestingly, the direct photoionization also quenches the dissociation of the core excited HCl molecule and enlarges the molecular contribution to the electron spectrum. If the pulse is more intense (or longer), more core excited HCl molecules are ionized before they dissociate, and hence the atomic peak can disappear. The molecular dissociation thus can serve as a clock for timing the pulse duration or for estimating the pulse intensity. Finally, the shape of the resonant Auger spectrum is changed[9], cf. the red solid curve and the black dashed line, because the direct photoionization shifts the positions of the DICES.

Being an unfortunate case, the resonant Auger process in HCl is not as strong as the direct photoionization. In this example, the DICES effect on the resonant Auger spectrum is not as pronounced as we first expected. However, our model study has

---

[9] Here we only show the result for a stronger intensity. Simulations show that the shape of the spectrum for a weak intensity as 10^{14} W/cm^2 does not depend on the presence of direct photoionization.

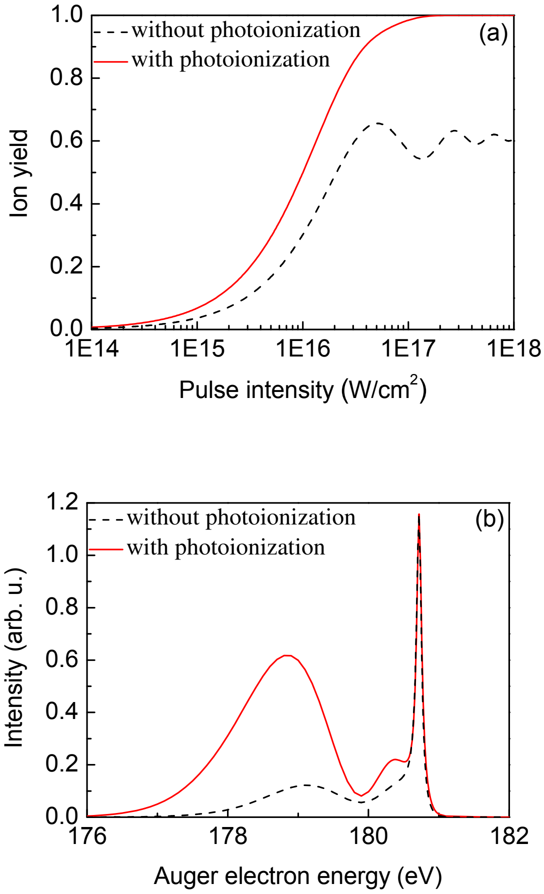

Figure 7.15: Simulations with and without the direction photoionization. The ion yields for the pulse duration $\tau = 2$ fs obtaining by 2D calculations are depicted in panel (a): the black dashed line shows the result without considering the photoionization, and the red solid curve shows the result with the direct photoionization. Due to the competition between direct photoionization and the resonant Auger process, the ion yield changes dramatically. Most population undergoes direct photoionization instead of the resonant Auger decay. For the pulse intensity $5 \times 10^{16}\mathrm{W/cm}^2$, spectra calculated with direct photoionization (multiplied by 9.36) and without direct photoionization (multiplied by 0.26) are depicted in panel (b). The strong direct photoionization not only reduces the total probability for the ground state molecule undergoing the resonant Auger process, but also quenches the probability for the excited HCl to dissociate and decay via electron emission. In comparison to the atomic contribution to the Auger spectrum, the molecular contribution becomes dramatically dominant. In addition, the photoionization changes the positions of DICES and hence the spectral shape is altered significantly.

confirmed the importance of the DICES (at least the molecular rotation) under an intense X-ray pulse. Concerning experimental observations under intense laser pulses, one is well advised to look for other more “lucky” cases, where the transition dipole moment is much larger and the photoionization cross section is much smaller. For instance, the CO molecule has been suggested [109]. On the other hand, core excited HCl demonstrates a strong dissociation tendency, and shows its potential for timing the pulse duration as well as for estimating the pulse intensity via analyzing the ratio of the molecular peak and atomic peak.

Chapter 8

Summary

In this work, we first investigated a cascade decay process, namely an interatomic Coulombic decay (ICD) following an Auger decay, in the NeAr dimer. This process starts from the photoionization of a core $1s$ electron of Ne. The resulting ionic state immediately decays through the Auger process and produces $\mathrm{Ne}^{2+}\mathrm{Ar}$. The produced doubly ionic states, namely the singlet and triplet $\mathrm{Ne}^{2+}(2s^{-1}2p^{-1})\mathrm{Ar}$, can then further decay by ICD via emitting a valence electron from Ar. After the ICD process, the resulting Ne^{2+}-Ar^{+} then undergoes Coulomb explosion. Such a process can be identified by measuring the energies of the emitted ICD electrons or of the ionic fragments, separately or in coincidence. Experiments often measure the kinetic energy release (KER) spectrum, where KER is the sum of the translational energies of all ionic fragments minus the translational energy of the center of mass. Usually, the ICD electron spectrum and its corresponding KER spectrum are considered to be mirror images of each other, which is based on an empirical rule [8, 10]. Our investigation began with a computation of the ICD electron spectrum for this process, based on a time-dependent approach and using potential energy curves and ICD rates which are obtained from *ab initio* calculations [42].

In Ch. 3, our calculations showed that the triplet state $\mathrm{Ne}^{2+}(2s^{-1}2p^{-1}\ {}^3P)\mathrm{Ar}$ (ICD channel 3) exhibits a strong impact of the the nuclear dynamics on the spectrum, while the single state $\mathrm{Ne}^{2+}(2s^{-1}2p^{-1}\ {}^1P)\mathrm{Ar}$ (ICD channel 1) does not. However, when a comparison with the experimental KER spectrum is performed (via the mirror image relation), the experimental KER spectrum of ICD channel 1 also shows a strong fingerprint of the nuclear dynamics. In contrast, the theoretical and experimental results agree well for ICD channel 3. To understand how the discrepancy between theory and experiment in ICD channel 1 can be explained, we have studied (i) the fast Auger decay approximation and (ii) the impact of varying the ICD transition rates in Ch. 4. Within the fast Auger decay approximation, it is assumed that the Auger decay is much faster than the nuclear motion of $\mathrm{Ne}^{+}\mathrm{Ar}$, so that the nuclear dynamics in the first decay step can be ignored. To test this assumption, we have carried out a full cascade calculation for the ICD following the Ne 1s Auger decay in NeAr. The ICD electron spectrum obtained from this calculation agrees well with our previous result, which has been obtained using the fast Auger decay approximation. Hence the validity of the fast Auger decay approximation is confirmed. We then turned to the possibility that the *ab initio* ICD transition rates were overestimated. By performing simulations with modified transition rates, it is possible to find the best fit for the experimental spectrum. This procedure suggests that the actual ICD transition rate differs from the *ab initio* one by a factor of 0.4. (see Ch. 4).

As an additional result, our full cascade calculation for the ICD following Auger decay in NeAr also showed that the presence of subsequent ICD processes broadens the Auger electron spectrum. Namely, the FWHM of the Auger electron spectrum for such a cascade decay process is given by the sum of the Ne 1s Auger natural width and the total ICD width at equilibrium internuclear distance R. Hence we suggest to measure the FWHM of the Auger electron spectrum of the Ne K-LL Auger process, in order to confirm our current conclusion. This effect of broadening the Auger spectrum, as well as the correct formulation of a time-resolved electron spectrum, is explained in detail by employing an atomic level model of a cascade decay process in Ch. 5.

As previously mentioned, there exists an empirical rule which states that an electron spectrum and its corresponding KER spectrum are mirror images of each other. In Ch. 6, this empirical rule has been studied in detail by considering the general case of a fragmentation accompanying a decay by electron emission. We have derived an important new formula for evaluating the (time-resolved) KER spectrum more efficiently than by the methods reported in Refs. [9, 24, 65]. Our new formula shows that, in a diatomic system, the (time-resolved) KER spectrum for a fragmentation following an electronic decay process is given by the generalized Franck-Condon factor accumulated over time. In contrast to the KER spectrum, the electron spectrum for this process is given by the final state population, as has been previously known [26, 44]. The two spectra together contain complete information on the decay process followed by fragmentation. Our further studies showed that the KER distribution can indeed be very different from the mirror image of the electron spectrum, by considering the dissociation following the molecular Auger process in CO as example. All our computed spectra agree well with experiment. Additionally, we also concluded that within a diatomic system the mirror image principle holds if all the populated levels are quasi-degenerate and the lifetime broadening is small. These two conditions are often fulfilled in ICD processes between noble gas dimers. Our simulations confirmed that in these cases, the KER spectrum is indeed very close to the mirror image of its corresponding ICD electron spectrum.

Finally, the role of a laser pulse has been studied in Chapter 7, where we have investigated the photoexcitation of a core electron in a diatomic molecule, which results in a *resonant* Auger process. For this case, the interplay between the pulse duration and the nuclear dynamics has already been extensively studied under a weak field approximation [26]. Here, the direct application to an intense X-ray laser is tested with parameters of a realistic example, namely the HCl molecule, which was chosen due to its unique dissociative intermediate state. Our simulations show that not only the stretch motion (internal motion) but also the rotation (an overall rotation in the laboratory frame) is relevant when the molecule interacts with an intense laser field. Including both molecular rotation and stretching motion on the two coupled electronic states (ground state and dressed excited state) enables us to describe a strong non-adiabatic effect which is induced by light [34, 89]. In our example, the excited state decays via electron emission, and hence its potential surface contains an imaginary part, stemming from the decay rate. In consequence, the adiabatic potentials of the two coupled states are complex-valued and in general have two intersections. This effect has been termed [104] doubly intersecting complex electronic surfaces (DICES). Our simulations show that this effect is important even for a diatomic molecule under an intense laser field. However, studying HCl without considering photoionization is incorrect because ionization can become substantial and could compete with the resonant Auger process. In the last section of Chapter 7, our simulations showed that the direct photoionization could even quench the resonant Auger of HCl when the laser intensity is increased. But the light-induced non-adiabatic effect is still important for simulating the resonant Auger spectrum at lower laser intensities where the photoionization isn't dominating yet, see also [109]. Finally, we have suggested that the resonant Auger process in HCl can serve as a clock for timing the laser pulse duration or for measuring the pulse intensity, due to its unique dissociative core-excited state and large ionization cross-section.

Chapter 9

Appendix

Appendix A: The Local Approximation

The last term of Eq. (2.11) reads

$$-i \iint \mathrm{d}t'\mathrm{d}E_{e_2}\, \hat{W}^{\dagger}_{d_2\to f}(E_{e_2}) e^{i(\hat{H}_f+E_{e_0}+E_{e_1}+E_{e_2})(t'-t)} \hat{W}_{d_2\to f}(E_{e_2})|\psi_{d_2}(E_{e_0},E_{e_1},t')\rangle \ .$$

Note that the integration limits are from 0 to ∞ for E_{e_2} and from $-\infty$ to t for t'. Here the local approximation [26] is applied to carry out this integration.

To proceed, first the integration over energy is evaluated by assuming that the energy dependence of the transition matrix element is separable, i.e. $\hat{W}_{d_2\to f}(E_{e_2}) = \hat{W}_{d_2\to f} f(E_{e_2})$, and $|f(E_{e_2})|^2$ is 1 within the energy range 0 to 2ε and 0 elsewhere [26]. The value of ε will be determined in the later derivation.

$$\begin{aligned}
&\int_{-\infty}^{t} \mathrm{d}t' \int_0^{\infty} \mathrm{d}E_{e_2}\, \hat{W}^{\dagger}_{d_2\to f}(E_{e_2}) e^{i(\hat{H}_f+E_{e_0}+E_{e_1}+E_{e_2})(t'-t)} \hat{W}_{d_2\to f}(E_{e_2})|\psi_{d_2}(E_{e_0},E_{e_1},t')\rangle \\
&\approx \int_{-\infty}^{t} \mathrm{d}t' \int_0^{\infty} \mathrm{d}E_{e_2}\, |f(E_{e_2})|^2 e^{i(E_{e_2}-\varepsilon)(t'-t)}\, \hat{W}^{\dagger}_{d_2\to f} e^{i(\hat{H}_f+E_{e_0}+E_{e_1}+\varepsilon)(t'-t)} \hat{W}_{d_2\to f}|\psi_{d_2}(E_{e_0},E_{e_1},t')\rangle \\
&= \int_{-\infty}^{t} \mathrm{d}t' \int_0^{2\varepsilon} \mathrm{d}E_{e_2}\, e^{i(E_{e_2}-\varepsilon)(t'-t)}\, \hat{W}^{\dagger}_{d_2\to f} e^{i(\hat{H}_f+E_{e_0}+E_{e_1}+\varepsilon)(t'-t)} \hat{W}_{d_2\to f}|\psi_{d_2}(E_{e_0},E_{e_1},t')\rangle \\
&= \int_{-\infty}^{t} \mathrm{d}t' \frac{2\sin\varepsilon(t'-t)}{(t'-t)}\, \hat{W}^{\dagger}_{d_2\to f} e^{i(\hat{H}_f+E_{e_0}+E_{e_1}+\varepsilon)(t'-t)} \hat{W}_{d_2\to f}|\psi_{d_2}(E_{e_0},E_{e_1},t')\rangle \qquad (1)
\end{aligned}$$

The next step is to evaluate the integral over time. To do so, note that the wave function $|\psi_{d_2}(E_{e_0},E_{e_1},t')\rangle$ can be approximately written as $e^{-i(\langle\hat{H}_{d_2}\rangle+E_{e_0}+E_{e_1})t'}|\psi_{d_2}\rangle$, where $|\psi_{d_2}\rangle$

varies only slowly in time, and $\langle \hat{H}_{d_2} \rangle$ is the approximated energy for state d_2.[1] Hence we can replace $|\psi_{d_2}(E_{e_0}, E_{e_1}, t')\rangle$ by $e^{-i(\langle \hat{H}_{d_2}\rangle + E_{e_0} + E_{e_1})(t'-t)}|\psi_{d_2}(E_{e_0}, E_{e_1}, t)\rangle$. Continuing with Eq. (1), the integral approximately reads

$$\begin{aligned}
&\int_{-\infty}^{t} \mathrm{d}t' \frac{2\sin\varepsilon(t'-t)}{(t'-t)}\, \hat{W}^{\dagger}_{d_2\to f} e^{i(\hat{H}_f + \varepsilon - \langle \hat{H}_{d_2}\rangle)(t'-t)} \hat{W}_{d_2\to f} |\psi_{d_2}(E_{e_0}, E_{e_1}, t)\rangle \\
&\approx \int_{-\infty}^{t} \mathrm{d}t' \frac{2\sin\varepsilon(t'-t)}{(t'-t)}\, |\hat{W}_{d_2\to f}|^2 |\psi_{d_2}(E_{e_0}, E_{e_1}, t)\rangle \\
&= \frac{1}{2}\int_{-\infty}^{\infty} \mathrm{d}(t'-t) \frac{2\sin\varepsilon(t'-t)}{(t'-t)}\, |\hat{W}_{d_2\to f}|^2 |\psi_{d_2}(E_{e_0}, E_{e_1}, t)\rangle \\
&= \pi |\hat{W}_{d_2\to f}|^2 |\psi_{d_2}(E_{e_0}, E_{e_1}, t)\rangle \ . \qquad (2)
\end{aligned}$$

Note that we have chosen $\varepsilon = \langle \hat{H}_{d_2}\rangle - \langle \hat{H}_f \rangle$ so that the phase becomes approximately zero, i.e.

$$\hat{H}_f + \varepsilon - \langle \hat{H}_{d_2}\rangle = \hat{H}_f - \langle \hat{H}_f \rangle \approx 0 \ .$$

Defining the total transition rate as $\Gamma_{d_2} = 2\pi |\hat{W}_{d_2\to f}|^2$, where $\hat{W}_{d_2\to f}$ now is only a R-dependent, potential-like operator, we arrive at

$$\begin{aligned}
&-i \iint \mathrm{d}t' \mathrm{d}E_{e_2}\, \hat{W}^{\dagger}_{d_2\to f}(E_{e_2}) e^{i(\hat{H}_f + E_{e_0} + E_{e_1} + E_{e_2})(t'-t)} \hat{W}_{d_2\to f}(E_{e_2}) |\psi_{d_2}(E_{e_0}, E_{e_1}, t')\rangle \\
&\approx -i \frac{\Gamma_{d_2}}{2} |\psi_{d_2}(E_{e_0}, E_{e_1}, t)\rangle \ .
\end{aligned}$$

Similarly, the local approximation is applied to carry out the double integral in Eq. (2.14).

$$\begin{aligned}
&-i \int_{-\infty}^{t} \mathrm{d}t' \int_{0}^{\infty} \mathrm{d}E_{e_1}\, \hat{W}^{\dagger}_{d_1\to d_2}(E_{e_1}) e^{i(\hat{\mathcal{H}}_{d_2} + E_{e_0} + E_{e_1})(t'-t)} \hat{W}_{d_1\to d_2}(E_{e_1}) |\psi_{d_1}(E_{e_0}, t')\rangle \\
&\approx -i \int_{-\infty}^{t} \mathrm{d}t' \frac{2\sin\varepsilon(t'-t)}{(t'-t)} e^{\Gamma_{d_2}(t'-t)/2} \hat{W}^{\dagger}_{d_1\to d_2} e^{i(\hat{H}_{d_2} + \varepsilon - \langle \hat{H}_{d_1}\rangle)(t'-t)} \hat{W}_{d_1\to d_2} |\psi_{d_1}(E_{e_0}, t)\rangle \\
&\approx -2i \arctan\left(\frac{\varepsilon}{\Gamma_{d_2}/2}\right) |\hat{W}_{d_1\to d_2}|^2 |\psi_{d_1}(E_{e_0}, t)\rangle \\
&\approx -i\pi |\hat{W}_{d_1\to d_2}|^2 |\psi_{d_1}(E_{e_0}, t)\rangle \qquad (3)
\end{aligned}$$

Due to the presence of the decay rate Γ_{d_2}, the integration over time results in $\arctan(2\varepsilon/\Gamma_{d_2})$, where ε is now chosen to be the energy gap between state d_1 and state d_2. Since the energy gap is often much larger than the decay width, $\arctan(2\varepsilon/\Gamma_{d_2})$ is practically $\pi/2$, and the total decay rate of state d_1 again reads $\Gamma_{d_1} = 2\pi |\hat{W}_{d_1\to d_2}|^2$.

---

[1] The potential V_{d_2} is sometimes taken as the value of $\langle \hat{H}_{d_2} \rangle$. In this case, it is termed "frozen nuclei approximation."[33]

Appendix B: Rate of Photoionization

To carry out the non-local term in Eq. (2.17), let us begin with the operator $\hat{F}(E_{e_0}, t)$.

$$\hat{F}(E_{e_0}, t) = \boldsymbol{\mu}(E_{e_0}) \cdot \mathbf{E}(t)$$

where $\boldsymbol{\mu}(E_{e_0}) = |\langle \Phi_{d_1}, E_{e_0}|\hat{\mathbf{D}}|\Phi_i\rangle|$. The linearly polarized laser field can be approximated by $\mathbf{E}(t) = \frac{1}{2}\varepsilon_0 e^{-i\omega t} g(t)\hat{z}$, using the long wavelength and rotating wave approximations [37, 38]. ε_0 denotes the laser electric field amplitude; $g(t)$ denotes the envelope function of the field, and ω denotes the incident photon energy. The operator now reads

$$\hat{F}(E_{e_0}, t) = \mu(E_{e_0})\frac{\varepsilon_0}{2} e^{-i\omega t} g(t)\cos\theta \tag{4}$$

where the θ denotes the angle between the directions of the dipole transition moment and of the electric field polarization. The incident photon energy is chosen to be well above the ionization threshold, so that $\mu(E_{e_0}) = |\boldsymbol{\mu}(E_{e_0})|$ varies very slowly with E_{e_0} and hence can be considered as independent of E_{e_0} for performing the integration. Besides, the envelope of the pulse $g(t)$ is also assumed to be slowly varying in time and does not affect the integration. Using Eq. (4), the non-local term of Eq. (2.17) now reads

$$\begin{aligned}
&-i\int_{-\infty}^{t} \mathrm{d}t' \int_0^{\infty} \mathrm{d}E_{e_0}\, \hat{F}^{\dagger}(E_{e_0}, t) e^{i(\hat{\mathcal{H}}_{d_1}+E_{e_0})(t'-t)} \hat{F}(E_{e_0}, t')|\psi_i(t')\rangle \\
&= -i\int_{-\infty}^{t} \mathrm{d}t' \int_0^{\infty} \mathrm{d}E_{e_0}\, \frac{\varepsilon_0}{2} g(t)\cos\theta e^{i\omega t} \mu e^{i(\hat{\mathcal{H}}_{d_1}+E_{e_0})(t'-t)} \frac{\varepsilon_0}{2} g(t')\cos\theta e^{-i\omega t'} \mu|\psi_i(t')\rangle \\
&\approx \frac{-i}{4}\int_{-\infty}^{t} \mathrm{d}t' \int_0^{2\varepsilon} \mathrm{d}E_{e_0}\, e^{i(E_{e_0}-\varepsilon)(t'-t)} \varepsilon_0 g(t')\cos\theta \mu e^{i(\hat{\mathcal{H}}_{d_1}-\omega+\varepsilon)(t'-t)} \varepsilon_0 g(t)\cos\theta \mu|\psi_i(t')\rangle \\
&\approx \frac{-i}{4}\int_{-\infty}^{t} \mathrm{d}t' \frac{2\sin\varepsilon(t'-t)}{(t'-t)} \varepsilon_0 g(t)\cos\theta \mu e^{i(\hat{\mathcal{H}}_{d_1}+\varepsilon-\omega-\langle\hat{\mathcal{H}}_{d_1}\rangle)(t'-t)} \varepsilon_0 g(t)\cos\theta \mu|\psi_i(t)\rangle \\
&\approx \frac{-i}{4}\pi\varepsilon_0^2 g^2(t)\cos^2\theta |\mu|^2|\psi_i(t)\rangle \\
&= -i\pi|\boldsymbol{\mu}\cdot\mathbf{E}(t)|^2|\psi_i(t)\rangle\ .
\end{aligned} \tag{5}$$

Note that $E(t) = \varepsilon_0 e^{-i\omega t} g(t)/2$.

The term $\boldsymbol{\mu}\cdot\mathbf{E}(t)$ in Eq. (5) can be further connected to the ionization cross-section of state i, the incident photon energy ω and the cycle-averaged laser intensity $I(t)$. Consider a system, e.g. atoms or molecules, in its rotational ground state. Namely, the system is not aligned and its orientation in space is isotropic. Hence the inner product between $\boldsymbol{\mu}$ and the external field must be averaged over the solid angle. Namely, we need to perform the average of

$$2\pi|\boldsymbol{\mu}\cdot\mathbf{E}(t)|^2 = 2\pi|\mu|^2|E(t)|^2\cos^2\theta$$

over the solid angle. This is done as follows:

$$\frac{1}{4\pi}\int_0^{2\pi}\mathrm{d}\phi\int_0^{\pi}\cos^2\theta\sin\theta\mathrm{d}\theta=\frac{1}{4\pi}\,2\pi\,\frac{2}{3}=\frac{1}{3}\ . \tag{6}$$

In addition, $|\mu|^2$ is related to the photoionization cross-section from state i to state d_1, i.e. σ_i, by [36]

$$|\mu|^2=\frac{3}{4\pi^2\alpha\omega}\sigma_i(\omega)\ ,$$

and $|E(t)|^2$ is related to the cycle-averaged laser intensity $I(t)$ by [52]

$$|E(t)|^2=\frac{\varepsilon_0^2g^2(t)}{4}=2\pi\alpha I(t)\ ,$$

where α is the fine structure constant. In consequence, the rate of ionization (from state i) reads [40]

$$\Gamma_{\mathrm{ph}}=2\pi|\boldsymbol{\mu}\cdot\mathbf{E}(t)|^2=\frac{\sigma_i(\omega)I(t)}{\omega}\ . \tag{7}$$

Different from Ref. [40], here we do not consider the reshaping of the pulse while it is traveling through the medium, and hence $I(t)$ is simply the cycle-averaged intensity.

Appendix C: Proof of Eq. 2.31

The proof of Eq. 2.31 is given below.

$$\begin{aligned}
&\iint\mathrm{d}t'\mathrm{d}E_{e_1}\,\hat{W}^{\dagger}_{d_{1_\alpha}\to d_{2_\beta}}(E_{e_1})e^{i(\hat{\mathcal{H}}_{d_{2_\beta}}+E_{e_0}+E_{e_1})(t'-t)}\frac{\Lambda_{\beta,\beta'}}{2}|\psi_{d_{2_{\beta'}}}(E_{e_0},E_{e_1},t')\rangle\\
&\approx\iint\mathrm{d}t'\mathrm{d}E_{e_1}\,\hat{W}^{\dagger}_{d_{1_\alpha}\to d_{2_\beta}}(E_{e_1})e^{i(\hat{\mathcal{H}}_{d_{2_\beta}}+E_{e_0}+E_{e_1})(t'-t)}\frac{\Lambda_{\beta,\beta'}}{2}e^{-i(\langle\hat{H}_{d_{2_{\beta'}}}\rangle+E_{e_0}+E_{e_1})(t'-t)}|\psi_{d_{2_{\beta'}}}(E_{e_0},E_{e_1},t)\rangle\\
&\approx\int_0^{\infty}\mathrm{d}E_{e_1}\int_{-\infty}^{t}\mathrm{d}t'e^{\Gamma_{d_{2_\beta}}(t'-t)/2}\hat{W}^{\dagger}_{d_{1_\alpha}\to d_{2_\beta}}(E_{e_1})\frac{\Lambda_{\beta,\beta'}}{2}|\psi_{d_{2_{\beta'}}}(E_{e_0},E_{e_1},t)\rangle\\
&\approx\frac{2}{\Gamma_{d_{2_\beta}}}\int_0^{\infty}\mathrm{d}E_{e_1}\hat{W}^{\dagger}_{d_{1_\alpha}\to d_{2_\beta}}(E_{e_1})\frac{\Lambda_{\beta,\beta'}}{2}|\psi_{d_{2_{\beta'}}}(E_{e_0},E_{e_1},t)\rangle\\
&\approx\frac{2}{\Gamma_{d_{2_\beta}}}\int_{-\infty}^{\infty}\mathrm{d}E_{e_1}\hat{W}^{\dagger}_{d_{1_\alpha}\to d_{2_\beta}}(E_{e_1})\frac{\Lambda_{\beta,\beta'}}{2}e^{-i(\langle\hat{H}_{d_{2_{\beta'}}}\rangle+E_{e_0}+E_{e_1})t}|\psi_{d_{2_{\beta'}}}\rangle\\
&\approx 0\ .
\end{aligned}\tag{8}$$

The rapid oscillating phase $e^{-iE_{e_1}t}$ leads the integration over E_{e_1} to zero.

Appendix D: EOMs for a Cascade Decay Following a Photoexcitation Process

EOMs for a cascade decay process, initiated by photoexcitation, can be obtained by the same procedure as shown in Ch. 2 with an initial wave function ansatz without the wave function of the photoelectron, i.e. no E_{e_0}. A separable cascade process with a non-degenerate excited state d_1 is chosen as an example. The EOMs are

$$\begin{aligned}
i|\dot{\psi}_i(t)\rangle &= \hat{H}_i|\psi_i(t)\rangle + \hat{F}^\dagger(t)|\psi_{d_1}(t)\rangle && (9)\\
i|\dot{\psi}_{d_1}(t)\rangle &= \hat{F}(t)|\psi_i(t)\rangle + \hat{\mathcal{H}}_{d_1}|\psi_{d_1}(t)\rangle && (10)\\
i|\dot{\psi}_{d_{2_\beta}}(E_{e_1},t)\rangle &= \hat{W}_{d_1\to d_{2_\beta}}|\psi_{d_1}(t)\rangle + (\hat{\mathcal{H}}_{d_{2_\beta}} + E_{e_1})|\psi_{d_{2_\beta}}(E_{e_1},t)\rangle && (11)\\
i|\dot{\psi}_{f_\gamma}(E_{e_1},E_{e_2},t)\rangle &= \hat{W}_{d_{2_\beta}\to f_\gamma}|\psi_{d_{2_\beta}}(E_{e_1},t)\rangle + (\hat{H}_{f_\gamma} + E_{e_1} + E_{e_2})|\psi_{f_\gamma}(E_{e_1},E_{e_2},t)\rangle. && (12)
\end{aligned}$$

The EOMs are almost identical to Eq. (2.54), except that there is no E_{e_0} nor ionization rate of state i in the current equations, and instead, the excited state d_1 is allowed to transition back to state i via a stimulated emission process.

Appendix E: Computational Details

For a time-independent non-Hermitian Hamiltonian (NeAr case and CO case), we employed the complex short iterative Lanczos (CSIL) integration scheme [43, 110], which makes use of the Lanczos-Arnoldi method [111], to propagate the wave function. In this scheme, the time-evolution operator $e^{i\hat{H}\tau}$ is evaluated and applied to the wave function at each time step, here with a time step $\tau = 0.05$ fs for NeAr and $\tau = 0.005$ fs for CO. This time step can be adjusted automatically by the program according to the chosen integration accuracy, e.g. 10^{-9}, and the allowed maximal Lanczos order, e.g. 20. While performing the integration, the Fast Fourier Transform (FFT) [112] is employed in order to evaluate the kinetic energy part of $\hat{H}^n|\Psi(t)\rangle$ $(n \geq 1)$. A uniformly spaced grid with the typical grid spacing 0.5 pm is used. The number of grid points is often chosen as the power of 2, usually 2048 or larger. The grid range, of course, has to cover the reaction region. For example, the grid range for NeAr stretches from 180 to 1203.5 pm. Note that once the computation is converged, the calculated spectrum does not depend on which integration method is employed or which discrete variable representation is used. For more information on CSIL and FFT, see Refs. [33, 43] and the references therein.

For a time-dependent non-Hermitian Hamiltonian (HCl case), we employ the 8th order Runge-Kutta method (RK8) for the wave function propagation. To evaluate $\hat{H}|\Psi(t)\rangle$, FFT is again used for the stretching motion, while the basis for molecular overall rotation (θ) is chosen as associated Legendre polynomials. A grid spacing of 2.5 pm and 1600 grid points are used for FFT; 40 associated Legendre polynomials are used for θ.

Appendix F: Discrete Continuum Functions

For simplicity, the model of a single channel (f without γ label) is chosen. The computation of the KER spectrum via Eq. (6.18) requires a representation of the δ-normalized continuum state $|E_{\mathrm{KER}}\rangle$, or more precisely $|E_{\mathrm{KER}}\rangle\langle E_{\mathrm{KER}}|$. It can be expressed by a δ-function and, in turn, by a representation

$$|E_{\mathrm{KER}}\rangle\langle E_{\mathrm{KER}}| = \delta(E_{\mathrm{KER}} - (H_f - V_f^{\infty})) = \frac{1}{\pi} \lim_{\epsilon\to 0^+} \mathrm{Im} \frac{-1}{E_{\mathrm{KER}} - (H_f - V_f^{\infty}) + i\epsilon} \ . \tag{13}$$

The constant $i\epsilon$ can be replaced [113] by a complex absorbing potential (CAP) [114], introducing the CAP-augmented Hamiltonian

$$\tilde{H}_f = H_f - i\eta W_{\mathrm{CAP}} \ ,$$

where W_{CAP} is a non-negative potential-like function which vanishes in the interior region but increases for large distances. We have used

$$W_{\mathrm{CAP}}(R) = (R - R_c)^3 \, \theta(R - R_c) \ ,$$

where θ denotes the Heaviside step function and R_c is the point where the CAP is switched on. The CAP strength η must be chosen large enough such that high energy wave functions are absorbed before they reach the end of the grid, but small enough to ensure that the CAP does not introduce significant reflections [115]. Note that the eigenfunctions of the CAP-augmented Hamiltonian $\tilde{H}_f$ are purely discrete, and its complex eigenvalues $\tilde{E}_j$ have negative imaginary parts. Performing the inverse in Eq. (13) by diagonalisation leads Eq. (6.18) to the working equation of the KER spectrum

$$\sigma_{\mathrm{KER}}(E_{\mathrm{KER}}, t) = -2 \sum_j \ \mathrm{Im} \int_0^t \mathrm{d}t' \ \frac{\langle \psi_d(t')|\hat{W}^{\dagger}_{d\to f}|\phi_j)(\phi_j|\hat{W}_{d\to f}|\psi_d(t')\rangle}{E_{\mathrm{KER}} - (\tilde{E}_j - V_f^{\infty})} \ . \tag{14}$$

This equation is very stable and allows us to vary η over more than three orders of magnitude without virtually changing the computed KER spectrum. Only when η is too small we observe an artificial high frequency oscillation in the high energy part of the KER spectrum, and when η is too large there appear low-frequency oscillations in the low energy part of the KER spectrum.

Acknowledgements

The author thanks Prof. L. S. Cederbaum for the opportunity to work in a wonderful group as well as many interesting ideas, discussions, and support. Especially the author appreciates the freedom for thinking and studying independently but not lonely. Additionally, the author is in debt to Prof. H.-D. Meyer and Dr. F. Otto for countless scientific discussions and technical support during the PhD study.

Prof. J. Schirmer, Prof. H. Köppel, Dr. A. I. Kuleff, Dr. S. Stoychev, Dr. S. Scheit, Dr. A. Dutoi, Dr. K. Gokhberg, Dr. N. Sisourat, Dr. A. Bande, Dr. D. Peláez-Ruiz, Dr. M. Schröder, Dr. S. Klaiman, Dr. D. Davis, Dr. F. Pont, V. Vysotskiy, G. Jabbari, T. Miteva, K. Sadri, M. Eroms, and E. Faßhauer are acknowledged for sharing their knowledge with the author as a friend.

Dr. F. Otto, Dr. M. Schröder, and Dr. D. Peláez-Ruiz are acknowledged for proofreading this thesis.

The author would also like to thank her parents and Frank Otto for their spiritual support.

IMPRS-QD is acknowledged for the financial support from August 2008 till August 2011.

GK-850 is acknowledged for the financial support from September 2011 till March 2012.

Bibliography

[1] A. Temkin. *Autoionization.* Plenum Press, New York, 1985.

[2] P. Auger. Sur l'effet photolectrique compos. *J. Phys. Radium* **6** (1925), 205–208.

[3] G. S. Brown, M. H. Chen, B. Crasemann, and G. E. Ice. Observation of the Auger Resonant Raman Effect. *Phys. Rev. Lett.* **45** (1980), 1937–1940.

[4] G. Herzberg. *Atomic Spectra and Atomic Structure*, 2nd. ed. Dover, New York, 1945.

[5] L. S. Cederbaum, J. Zobeley, and F. Tarantelli. Giant intermolecular decay and fragmentation of clusters. *Phys. Rev. Lett.* **79** (1997), 4778.

[6] R. Santra, J. Zobeley, L. S. Cederbaum, and N. Moiseyev. Interatomic Coulombic decay in van der Waals clusters and impact of nuclear motion. *Phys. Rev. Lett.* **85** (2000), 4490–4493.

[7] S. Marburger, O. Kugeler, U. Hergenhahn, and T. Möller. Experimental evidence for interatomic Coulombic decay in Ne clusters. *Phys. Rev. Lett.* **90** (2003), 203401.

[8] T. Jahnke, A. Czasch, M. S. Schöffler, S. Schössler, A. Knapp, M. Käsz, J. Titze, C. Wimmer, K. Kreidi, R. E. Grisenti, A. Staudte, O. Jagutzki, U. Hergenhahn, H. Schmidt-Böcking, and R. Dörner. Experimental observation of interatomic Coulombic decay in neon dimers. *Phys. Rev. Lett.* **93** (2004), 163401.

[9] S. Scheit, L. S. Cederbaum, and H.-D. Meyer. Time-dependent interplay between electron emission and fragmentation in the interatomic Coulombic decay. *J. Chem. Phys.* **118** (2003), 2092.

[10] S. Scheit, V. Averbukh, H.-D. Meyer, N. Moiseyev, R. Santra, T. Sommerfeld, J. Zobeley, and L. S. Cederbaum. On the interatomic Coulombic decay in the Ne dimer. *J. Chem. Phys.* **121** (2004), 8393–8398.

[11] K. Kreidi, T. Jahnke, T. Weber, T. Havermeier, X. Liu, Y. Morisita, S. Schössler, L. P. H. Schmidt, M. Schöffler, M. Odenweller, N. Neumann, L. Foucar, J. Titze, B. Ulrich, F. Sturm, C. Stuck, R. Wallauer, S. Voss, I. Lauter, H. K.

Kim, M. Rudloff, H. Fukuzawa, G. Prümper, N. Saito, K. Ueda, A. Czasch, O. Jagutzki, H. Schmidt-Böcking, S. Stoychev, P. V. Demekhin, and R. Dörner. Relaxation processes following 1s photoionization and Auger decay in Ne_2. *Phys. Rev. A* **78** (2008), 043422.

[12] P. V. Demekhin, S. Scheit, S. D. Stoychev, and L. S. Cederbaum. Dynamics of interatomic Coulombic decay in a Ne dimer following the k-$L_1L_{2,3}(^1p)$ Auger transition in the Ne atom. *Phys. Rev. A* **78** (2008), 043421.

[13] N. Sisourat, N. V. Kryzhevoi, P. Kolorenč, S. Scheit, T. Jahnke, and L. S. Cederbaum. Ultralong-range energy transfer by interatomic Coulombic decay in an extreme quantum system. *Nature Phys.* **6** (2010), 508.

[14] T. Havermeier, T. Jahnke, K. Kreidi, R. Wallauer, S. Voss, M. Schöffler, S. Schössler, L. Foucar, N. Neumann, J. Titze, H. Sann, M. Kühnel, J. Voigtsberger, J. H. Morilla, W. Schöllkopf, H. Schmidt-Böcking, R. E. Grisenti, and R. Dörner. Interatomic Coulombic decay following photoionization of the helium dimer: Observation of vibrational structure. *Phys. Rev. Lett.* **104** (2010), 133401.

[15] M. Mucke, M. Braune, S. Barth, M. Förstel, T. Lischke, V. Ulrich, T. Arion, U. Becker, A. Bradshaw, and U. Hergenhahn. A hitherto unrecognized source of low-energy electrons in water. *Nature Phys.* **6** (2010), 143.

[16] T. Jahnke, H. Sann, T. Havermeier, K. Kreidi, C. Stuck, M. Meckel, M. Schöffler, N. Neumann, R. Wallauer, S. Voss, A. Czasch, O. Jagutzki, A. Malakzadeh, F. Afaneh, T. Weber, H. Schmidt-Böcking, and R. Dörner. Ultrafast energy transfer between water molecules. *Nature Phys.* **6** (2010), 139.

[17] S. D. Stoychev, A. I. Kuleff, and L. S. Cederbaum. On the intermolecular Coulombic decay of singly and doubly ionized states of water dimer. *J Chem Phys* **133** (2010), 154307.

[18] T. Weber, M. Weckenbrock, M. Balser, L. Schmidt, O. Jagutzki, W. Arnold, O. Hohn, M. Schöffler, E. Arenholz, T. Young, T. Osipov, L. Foucar, A. D. Fanis, R. Díez Muiño, H. Schmidt-Böcking, C. L. Cocke, M. H. Prior, and R. Dörner. Auger electron emission from fixed-in-space CO. *Phys. Rev. Lett.* **90** (2003), 153003.

[19] T. Weber, O. Jagutzki, M. Hattass, A. Staudte, A. Nauert, L. Schmidt, M. H. Prior, A. L. Landers, A. Bräuning-Demian, H. Bräuning, C. L. Cocke, T. Osipov, I. Ali, R. D. Muiño, D. Rolles, F. J. G. de Abajo, C. S. Fadley, M. A. V. Hove, A. Cassimi, H. Schmidt-Böcking, and R. Dörner. K-shell photoionization of CO and N_2: is there a link between the photoelectron angular distribution and the molecular decay dynamics? *J. Phys. B: At. Mol. Opt. Phys.* **34** (2001), 3669.

[20] W. Eberhardt, E. W. Plummer, I. W. Lyo, R. Carr, and W. K. Ford. Auger-electron ion coincidence studies of soft-x-ray–induced fragmentation of N_2. *Phys. Rev. Lett.* **58** (1987), 207–210.

[21] M. Neeb, J.-E. Rubensson, M. Biermann, and W. Eberhardt. Coherent excitation of vibrational wave functions observed in core hole decay spectra of O_2, N_2 and CO. *J. Electron Spectrosc. Relat. Phenom.* **67** (1994), 261.

[22] T. X. Carroll, K. J. Børve, L. J. Sæthre, J. D. Bozek, E. Kukk, J. A. Hahne, and T. D. Thomas. Carbon 1s photoelectron spectroscopy of CF_4 and CO: Search for chemical effects on the carbon 1s hole-state lifetime. *J. Chem. Phys.* **116** (2002), 10221.

[23] G. Herzberg. *Molecular Spectra and Molecular Structure: I. Spectra of Diatomic Molecules*, 2nd. ed. Van Nostrand Reinhold, Cincinnati, 1950.

[24] N. Sisourat, N. V. Kryzhevoi, P. Kolorenč, S. Scheit, and L. S. Cederbaum. Impact of nuclear dynamics on interatomic Coulombic decay in a He dimer. *Phys. Rev. A* **82** (2010), 053401.

[25] E. Kukk, H. Aksela, O. Sairanen, S. Aksela, A. Kivimki, E. Nmmiste, A. Ausmees, A. Kikas, S. J. Osborne, and S. Svensson. Auger decay of the dissociating coreexcited states in the HCl and DCl molecules. *J. Chem. Phys.* **104** (1996), 4475.

[26] E. Pahl, H.-D. Meyer, and L. S. Cederbaum. Competition between excitation and electronic decay of short-lived molecular states. *Z. Phys. D* **38** (1996), 215.

[27] F. Gel'mukhanov and H. Ägren. Resonant Raman X-ray scattering. *Phys. Rep.* **312** (1999), 87.

[28] D. J. Tannor. *Introduction to Quantum Mechanics.* University Science Books, California, 2007.

[29] H.-D. Meyer, F. Gatti, and G. A. Worth, Eds. *Multidimensional Quantum Dynamics.* WILEY-VCH Verlag GmbH & Co. KGaA, Weinheim, Germany, 2009.

[30] M. O. Krause and T. A. Carlson. Vacancy cascade in the reorganization of krypton ionized in an inner shell. *Phys. Rev.* **158** (1967), 18–24.

[31] S.-M. Huttula, S. Heinäsmäki, H. Aksela, E. Kukk, M. Huttula, and S. Aksela. Experimental and theoretical study of the cascade Auger transitions in Kr and Xe. *Phys. Rev. A* **67** (2003), 052703.

[32] K. Ueda, Y. Shimizu, H. Chiba, Y. Sato, M. Kitajima, H. Tanaka, and N. M. Kabachnik. Experimental determination of Auger-decay amplitudes from the angular correlations in Auger cascade following the $2p4s$ photoexcitation in Ar. *Phys. Rev. Lett.* **83** (1999), 5463.

[33] S. Scheit. *Nuclear dynamics in the decay of excited electronic states: theory including cascades and multimechanism decays and applications to the Interatomic Coulombic Decay.* PhD thesis, Ruperto-Carola University of Heidelberg, Germany, 2007.

[34] L. S. Cederbaum, Y.-C. Chiang, P. V. Demekhin, and N. Moiseyev. Resonant Auger decay of molecules in intense X-ray laser fields: Light-induced strong nonadiabatic effects. *Phys. Rev. Lett.* **106** (2011), 123001.

[35] V. Averbukha and L. S. Cederbaum. Ab initio calculation of interatomic decay rates by a combination of the Fano ansatz, Greens-function methods, and the Stieltjes imaging technique. *J. Chem. Phys.* **123** (2005), 204107.

[36] K. Gokhberg, V. Vysotskiy, L. S. Cederbaum, L. Storchi, F. Tarantelli, and V. Averbukh. Molecular photoionization cross sections by stieltjes-chebyshev moment theory applied to lanczos pseudospectra. *J. Chem. Phys.* **130** (2009), 064104.

[37] G. C. Schatz and M. A. Ratner. *Quantum Mechanics in Chemistry.* Dover Publications, INC., New York, 2002.

[38] D. J. Griffiths. *Introduction to Quantum Mechanics.* Prentice-Hall, INC., Englewood Cliffs, New Jersey, 1994.

[39] G. H. Wagnière. *Linear and Nonlinear Optical Properties of Molecules.* Verlag Helvetica Chimica Acta, Basel, Switzerland, 1993.

[40] J.-C. Liu, Y.-P. Sun, C.-K. Wang, H. Ågren, and F. Gel'mukhanov. Auger effect in the presence of strong x-ray pulses. *Phys. Rev. A* **81** (2010), 043412.

[41] S. Kopelke. *Quenching of Molecular Photodissociation by interatomic Coulombic Decay.* PhD thesis, Ruperto-Carola University of Heidelberg, Germany, 2011.

[42] P. V. Demekhin, Y.-C. Chiang, S. D. Stoychev, P. Kolorenč, S. Scheit, A. I. Kuleff, F. Tarantelli, and L. S. Cederbaum. Interatomic Coulombic decay and its dynamics in NeAr following K-LL Auger transition in the Ne atom. *J. Chem. Phys.* **131** (2009), 104303.

[43] M. H. Beck, A. Jäckle, G. A. Worth, and H.-D. Meyer. The multiconfiguration time-dependent Hartree (MCTDH) method: a highly efficient algorithm for propagating wavepackets. *Phys. Rep.* **324** (2000), 1.

[44] L. S. Cederbaum and F. Tarantelli. Nuclear dynamics of decaying states: A time-dependent formulation. *J. Chem. Phys.* **98** (1993), 9691.

[45] R. Santra and L. S. Cederbaum. Coulombic energy transfer and triple ionization in clusters. *Phys. Rev. Lett.* **90** (2003), 153401.

[46] S. D. Stoychev, A. I. Kuleff, F. Tarantelli, and L. S. Cederbaum. On the intermolecular electronic processes following Auger decay in neon dimer. *J Chem Phys* **129** (2008), 074307.

[47] A. Inoyatov, D. V. Filosofov, V. M. Gorozhankin, A. Kovalik, N. A. Lebedev, A. V. Lubashevskiy, A. F. Novgorodov, L. L. Perevoshchikov, T. Vylov, and E. A. Yakushev. The KLL Auger spectrum of neon from the EC-decay of ^{2}2Na. *J. Electron Spectrosc. Relat. Phenom.* **154** (2007), 79.

[48] P. Kolorenč, V. Averbukh, K. Gokhberg, and L. S. Cederbaum. Ab initio calculation of interatomic decay rates of excited doubly ionized states in clusters. *J. Chem. Phys.* **129** (2008), 244102.

[49] K. Gokhberg, S. Kopelke, N. V. Kryzhevoi, P. Kolorenč, and L. S. Cederbaum. Dependence of interatomic decay widths on the symmetry of the decaying state: Analytical expressions and *ab initio* results. *Phys. Rev. A* **81** (2010), 013417.

[50] J. Zobeley, R. Santra, and L. S. Cederbaum. Electronic decay in weakly bound heteroclusters: Energy transfer versus electron transfer. *J. Chem. Phys.* **115** (2001), 5076.

[51] K. Sakai, S. Stoychev, T. Ouchi, I. Higuchi, M. Schöffler, T. Mazza, H. Fukuzawa, K. Nagaya, M. Yao, Y. Tamenori, A. I. Kuleff, N. Saito, and K. Ueda. Electron-transfer-mediated decay and interatomic coulombic decay from the triply ionized states in argon dimers. *Phys. Rev. Lett.* **106** (2011), 033401.

[52] N. Rohringer and R. Santra. Resonant Auger effect at high X-ray intensity. *Phys. Rev. A* **77** (2008), 053404.

[53] M. Nisoli and G. Sansone. New frontiers in attosecond science. *Prog. Quantum Electron.* **33** (2009), 17–59.

[54] F. Krausz and M. Ivanov. Attosecond physics. *Rev. Mod. Phys.* **81** (2009), 163.

[55] M. Drescher, M. Hentschel, R. Klenberger, M. Ulberacker, V. Yakovlev, A. Scrinzl, T. Westerwalbesloh, U. Kleineberg, U. Heinzmann, and F. Krausz. Time-resolved atomic inner shell spectroscopy. *Nature* **419** (2002), 803.

[56] R. Schinke. *Photodissociation Dynamics.* Press Syndicate of the University of Cambridge, Cambridge, 1993.

[57] T. Ouchi, K. Sakai, H. Fukuzawa, I. Higuchi, P. V. Demekhin, Y.-C. Chiang, S. D. Stoychev, A. I. Kuleff, T. Mazza, M. Schöffler, K. Nagaya, M. Yao, Y. Tamenori, N. Saito, and K. Ueda. Interatomic Coulombic decay following Ne 1*s* auger decay in NeAr. *Phys. Rev. A* **83** (2011), 053415.

[58] M. Weissbluth. Atoms And Molecules. Academic Press, INC., 1978.

[59] V. Averbukh and L. S. Cederbaum. Ab initio calculation of interatomic decay rates by a combination of the Fano ansatz, Greens-function methods, and the Stieltjes imaging technique. *J. Chem. Phys.* **123** (2005), 204107.

[60] S.-M. Huttula, S. Heinäsmäki, H. Aksela, M. Jurvansuu, and S. Aksela. Many-electron effects in the Ar $2p^{-1}4s3s^{1}3p^{5}(^{3}p)4s$ resonant Auger transitions. *J. Phys. B: At. Mol. Opt. Phys.* **34** (2001), 2325.

[61] Y.-C. Chiang, P. V. Demekhin, A. I. Kuleff, S. Scheit, and L. S. Cederbaum. Linewidth and lifetime of atomic levels and the time evolution of spectra and coincidence spectra. *Phys. Rev. A* **81** (2010), 032511.

[62] S. Heinäsmäki, S.-M. Huttula, E. Kukk, and H. Aksela. *Surf. Rev. Lett.* **9** (2002), 137.

[63] J. Viefhaus, A. N. Grum-Grzhimailo, N. M. Kabachnik, and U. Becker. Electron-electron coincidence study of double Auger processes in atoms. *J. Electron Spectrosc. Relat. Phenom.* **141** (2004), 121.

[64] Y. Hikosaka, P. Lablanquie, F. Penent, P. Selles, T. Kaneyasu, E. Shigemasa, J. H. D. Eland, and K. Ito. Probing the mechanism of simultaneous two-electron emission on core-hole decay. *Phys. Rev. A* **80** (2009), 031404.

[65] N. Moiseyev, J. Zobeley, R. Santra, and L. S. Cederbaum. Fingerprints of the nodal structure of autoionizing vibrational wave functions in clusters: Interatomic Coulombic decay in Ne dimer. *J. Chem. Phys.* **114** (2001), 7351.

[66] Y.-C. Chiang, F. Otto, H.-D. Meyer, and L. S. Cederbaum. Interrelation between the distributions of kinetic energy release and emitted electron energy following the decay of electronic states. *Phys. Rev. Lett.* **107** (2011), 173001.

[67] Y.-C. Chiang, F. Otto, H.-D. Meyer, and L. S. Cederbaum. Kinetic energy release in fragmentation processes following electron emission: A time-dependent approach. *J. Chem. Phys.* **136** (2012), 114111.

[68] J. Laskin and C. Lifshitz. Kinetic energy release distributions in mass spectrometry. *Journal of Mass Spectrometry* **36** (2001), 459478.

[69] N. Mirsaleh-Kohan, W. D. Robertson, and R. N. Compton. Electron ionization time-of-flight mass spectrometry: Historical review and current applications. *Mass Spectrometry Reviews* **27** (2008), 237.

[70] O. Jagutzki, A. Cerezo, A. Czasch, R. Dörner, M. Hattas, M. Huang, V. Mergel, U. Spillmann, K. Ullmann-Pfleger, T. Weber, H. Schmidt-Böcking, and G. Smith. Multiple hit readout of a microchannel plate detector with a three-layer delay-line anode. *IEEE Transactions on Nuclear Science* **49** (2002), 2477.

[71] J. H. D. Eland, M. Hochlaf, G. C. King, P. S. Kreynin, R. J. LeRoy, I. R. McNab, and J.-M. Robbe. Photo double ionization spectra of CO: comparison of theory with experiment. *J. Phys. B: At. Mol. Opt. Phys.* **37** (2004), 3197.

[72] M. Matsumoto, K. Ueda, E. Kukk, H. Yoshida, T. Tanaka, M. Kitajima, H. Tanaka, Y. Tamenori, K. Kuramoto, M. Ehara, and H. Nakatsuji. Vibrationally resolved C and O 1s photoelectron spectra of carbon monoxides. *Chem. Phys. Lett.* **417** (2006), 89–93.

[73] Y. H. Jiang, A. Rudenko, J. F. Pérez-Torres, O. Herrwerth, L. Foucar, M. Kurka, K. U. Kühnel, M. Toppin, E. Plésiat, F. Morales, F. Martín, M. Lezius, M. F. Kling, T. Jahnke, R. Dörner, J. L. Sanz-Vicario, J. van Tilborg, A. Belkacem, M. Schulz, K. Ueda, T. J. M. Zouros, S. Düsterer, R. Treusch, C. D. Schröter, R. Moshammer, and J. Ullrich. Investigating two-photon double ionization of D_2 by XUV-pump–XUV-probe experiments. *Phys. Rev. A* **81** (2010), 051402(R).

[74] I. A. Bocharova, A. S. Alnaser, U. Thumm, T. Niederhausen, D. Ray, C. L. Cocke, and I. V. Litvinyuk. Time-resolved Coulomb-explosion imaging of nuclear wave-packet dynamics induced in diatomic molecules by intense few-cycle laser pulses. *Phys. Rev. A* **83** (2011), 013417.

[75] E. Kukk, S. Aksela, and H. Aksela. Features of the Auger resonant Raman effect in experimental spectrum. *Phys. Rev. A* **53** (1996), 327.

[76] F. Gel'mukhanov and H. Ågren. Resonant X-ray Raman scattering. *Phys. Rep.* **312** (1999), 87.

[77] M. Grimm, B. Langer, S. Schlemmer, T. Lischke, U. Becker, W. Widdra, D. Gerlich, R. Flesch, and E. Rühl. Charging mechanisms of trapped element-selectively excited nanoparticles exposed to soft X-rays. *Phys. Rev. Lett.* **96** (2006), 066801.

[78] O. Kugeler, G. Prümper, R. Hentges, J. Viefhaus, D. Rolles, U. Becker, S. Marburger, and U. Hergenhahn. Intramolecular electron scattering and electron transfer following autoionization in dissociating molecules. *Phys. Rev. Lett.* **93** (2004), 033002.

[79] P. O'Keeffe, S. Aloïse, M. Meyer, and A. N. Grum-Grzhimailo. Circular polarization of ion fluorescence completing the analysis of resonant Xe* $4d_{5/2}^{-1}6p$ Auger decay. *Phys. Rev. Lett.* **90** (2003), 023002.

[80] R. Feifel, F. Burmeister, P. Sałek, M. N. Piancastelli, M. Bässler, S. L. Sorensen, C. Miron, H. Wang, I. Hjelte, O. Björneholm, A. Naves de Brito, F. K. Gel'mukhanov, H. Ågren, and S. Svensson. Observation of a continuum-continuum interference hole in ultrafast dissociating core-excited molecules. *Phys. Rev. Lett.* **85** (2000), 3133–3136.

[81] K. Ueda, M. Simon, C. Miron, N. Leclercq, R. Guillemin, P. Morin, and S. Tanaka. Correlation between nuclear motion in the core-excited CF_4 molecule and molecular dissociation after resonant Auger decay. *Phys. Rev. Lett.* **83** (1999), 3800–3803.

[82] E. Pahl, L. S. Cederbaum, H.-D. Meyer, and F. Tarantelli. Controlled interplay between decay and fragmentation in resonant Auger processes. *Phys. Rev. Lett.* **80** (1998), 1865–1868.

[83] J. Arthur *et al.* Linac coherent light source (LCLS) conceptual design report no. slac-r-593. Tech. rep., SLAC, http://www-ssrl.slac.stanford.edu/lcls/cdr/, 2002.

[84] T. Tanaka and T. Shintake. SCSS X-FEL conceptual design report. Tech. rep., SPring-8, http://www-xfel.spring8.or.jp/, 2005.

[85] M. Altarelli *et al.* The European X-ray free-electron laser technical design report. Tech. rep., DESY, 2006.

[86] L. Young, E. P. Kanter, B. Krssig, Y. Li, A. M. March, S. T. Pratt, R. Santra, S. H. Southworth, N. Rohringer, L. F. DiMauro, G. Doumy, C. A. Roedig, N. Berrah, L. Fang, M. Hoener, P. H. Bucksbaum, J. P. Cryan, S. Ghimire, J. M. Glownia, D. A. Reis, J. D. Bozek, C. Bostedt, and M. Messerschmidt. Femtosecond electronic response of atoms to ultra-intense X-rays. *Nature* **466** (2010), 56–61.

[87] K. Rzążewski, J. Zakrzewski, M. Lewenstein, and J. W. Haus. Strong-field autoionization by smooth laser pulses. *Phys. Rev. A* **31** (1985), 2995–3002.

[88] P. V. Demekhin and L. S. Cederbaum. Strong interference effects in the resonant Auger decay of atoms induced by intense x-ray fields. *Phys. Rev. A* **83** (2011), 023422.

[89] M. Sindelka, N. Moiseyev, and L. S. Cederbaum. Strong impact of light-induced conical intersections on the spectrum of diatomic molecules. *J. Phys. B: At. Mol. Opt. Phys.* **44** (2011), 045603.

[90] N. Rohringer and R. Santra. X-ray nonlinear optical processes using a self-amplified spontaneous emission free-electron laser. *Phys. Rev. A* **76** (2007), 033416.

[91] Y.-P. Sun, J.-C. Liu, C.-K. Wang, and F. Gel'mukhanov. Propagation of a strong x-ray pulse: Pulse compression, stimulated raman scattering, amplified spontaneous emission, lasing without inversion, and four-wave mixing. *Phys. Rev. A* **81** (2010), 013812.

[92] http://www.elettra.trieste.it/it/lightsources/fermi/fermi-machine/general-description.html.

[93] H. Aksela, S. Aksela, M. Ala-Korpela, O.-P. Sairanen, M. Hotokka, G. M. Bancroft, K. H. Tan, and J. Tulkki. Decay channels of core-excited HCl. *Phys. Rev. A* **41** (1990), 6000–6005.

[94] A. Menzel, B. Langer, J. Viefhaus, S. B. Whitfield, and U. Becker. Competition between direct dissociation and resonant Auger decay: a quasi-classical model applied to the $2p^{-1}\sigma^*$ states of HCl, DCl and Cl_2. *Chem. Phys. Lett.* **258** (1996), 265–270.

[95] E. Kukk, H. Aksela, S. Aksela, F. Gel'mukhanov, H. Ågren, and S. Svensson. Raman versus non-Raman behavior in resonant Auger spectra of HCl. *Phys. Rev. Lett.* **76** (1996), 3100–3103.

[96] O. Björneholm, S. Sundin, S. Svensson, R. R. T. Marinho, A. Naves de Brito, F. Gel'mukhanov, and H. Ågren. Femtosecond dissociation of core-excited HCl monitored by frequency detuning. *Phys. Rev. Lett.* **79** (1997), 3150–3153.

[97] Z. W. Gortel, R. Teshima, and D. Menzel. Auger resonant Raman effect for dissociative core-excited states: general treatment and application to the HCl case. *Phys. Rev. A* **60** (1999), 2159–2175.

[98] P. Sałek, F. Gel'mukhanov, and H. Ågren. Wave-packet dynamics of resonant x-ray Raman scattering: excitation near the Cl $L_{II,III}$ edge of HCl. *Phys. Rev. A* **59** (1999), 1147–1159.

[99] A. D. Pradhan, K. P. Kirby, and A. Dalgarno. Theoretical study of HCl^+ : Potential curves, radiative lifetimes, and photodissociation cross sections. *J. Chem. Phys.* **95** (1991), 9009.

[100] R. F. Fink, M. Kivilompolo, and H. Aksela. Theory and ab initio calculations of $2p$ photoabsorption spectra: The lowest rydberg resonances in HCl. *J. Chem. Phys.* **111** (1999), 10034.

[101] C. Brion. Database of absolute dipole photoabsorption oscillator strengths of atoms and small molecules.

[102] I. Cacellit, V. Carravetta, and R. Moccia. Photoionization cross section calculations of HCI by the Stieltjes technique effect of the channel coupling. *Mol. Phys.* **59**, 3 (1986), 385–402.

[103] H. Köppel, W. Domcke, and L. S. Cederbaum. Multimode molecular dynamics beyond the Born-Oppenheimer approximation. *Adv. Chem. Phys.* **57** (1984), 59.

[104] S. Feuerbacher, T. Sommerfeld, and L. S. Cederbaum. Intersections of potential energy surfaces of short-lived states: The complex analogue of conical intersections. *J. Chem. Phys.* **120** (2004), 3201.

[105] H.-D. Meyer, U. Manthe, and L. Cederbaum. The multi-configurational time-dependent hartree approach. *Chem. Phys. Lett.* **165** (1990), 73–78.

[106] G. A. Worth, M. H. Beck, A. Jäckle, and H.-D. Meyer. The MCTDH package, version 8.2 (2000), version 8.3 (2002), version 8.4 (2007).

[107] L. Allen and J. H. Eberly. *Optical Resonance And Two-Level System.* Dover Publications, INC., New York, 1987.

[108] E. Pahl, J. Brand, L. S. Cederbaum, and F. Tarantelli. Impact of narrow-band excitation on resonance decay spectra. *Phys. Rev. A* **60** (1999), 1079.

[109] P. V. Demekhin, Y.-C. Chiang, and L. S. Cederbaum. Resonant Auger decay of the core-excited C*O molecule in intense x-ray laser fields. *Phys. Rev. A* **84** (2011), 033417.

[110] T. J. Park and J. C. Light. Unitary quantum time evolution by iterative Lanczos reduction. *J. Chem. Phys.* **85** (1986), 5870.

[111] W. E. Arnoldi. The principle of minimized iterations in the solution of the matrix eigenvalue problem. *Q. Appl. Math.* **9** (1951), 17.

[112] C. J. Temperton. Self-sorting mixed-radix fast Fourier transforms. *J. Comp. Phys.* **52** (1983), 1.

[113] T. Seideman and W. H. Miller. Calculation of the cumulative reaction probability via a discrete variable representation with absorbing boundary conditions. *J. Chem. Phys.* **96** (1992), 4412.

[114] U. V. Riss and H.-D. Meyer. Calculation of resonance energies and widths using the complex absorbing potential method. *J. Phys. B: At. Mol. Opt. Phys.* **26** (1993), 4503.

[115] U. V. Riss and H.-D. Meyer. Investigation on the reflection and transmission properties of complex absorbing potentials. *J. Chem. Phys.* **105** (1996), 1409.

Ich erkläre hiermit an Eides statt, dass ich die vorgelegte Dissertation selbst verfasst und mich dabei keiner anderen als der von mir ausdrücklich bezeichneten Quellen und Hilfen bedient habe.

Ich erkläre hiermit an Eides statt, dass ich an keiner anderen Stelle ein Prüfungsverfahren beantragt beziehungsweise die Dissertation in dieser oder anderer Form bereits anderweitig als Prüfungsarbeit verwendet oder einer anderen Fakultät als Dissertation vorgelegt habe.

Ying-Chih Chiang